

UC Berkeley

UC Berkeley Electronic Theses and Dissertations

Title

Theoretical Understanding and Exploitation of Phase Transitions for Thermal Applications

Permalink

<https://escholarship.org/uc/item/7nx4h741>

Author

Kang, Hyungmook

Publication Date

2020

Peer reviewed|Thesis/dissertation

Theoretical Understanding and Exploitation of Phase Transitions for Thermal Applications

By

Hyungmook Kang

A dissertation submitted in partial satisfaction of the

requirements for the degree of

Doctor of Philosophy

in

Engineering – Mechanical Engineering

in the

Graduate Division

of the

University of California, Berkeley

Committee in charge:

Professor Chris Dames, Co-Chair

Dr. Jeffrey J. Urban, Co-Chair

Professor Mark D. Asta

Professor Van P. Carey

Fall 2020

Theoretical Understanding and Exploitation of Phase Transitions for Thermal Applications

Copyright 2020

by

Hyungmook Kang

Abstract

Theoretical Understanding and Exploitation of Phase Transitions for Thermal Applications

by

Hyungmook Kang

Doctor of Philosophy in Mechanical Engineering

University of California, Berkeley

Professor Chris Dames, Co-Chair

Dr. Jeffrey J. Urban, Co-Chair

Direct usage of thermal energy, instead of electricity, is intriguing to diminish total energy consumption with a benefit of reducing the number of energy conversions by directly utilizing such solar power and waste heat. Although various thermally driven systems have been suggested to overcome the problem of electricity-dependent systems, materials for the mechanisms limit the realization and effective operation of the systems. A more complete theoretical understanding of materials for thermal applications can suggest guidance to determine the bottlenecks of current materials and then ways to develop new materials. Among many computational methods, molecular dynamics (MD) simulations especially provide a molecular insight into structures of materials and phononic heat transfer at nanoscale.

In this dissertation, I discuss unconventional phase transition materials for thermal applications. Here, I focus on two types of phase transition materials. The lower critical solution temperature (LCST) liquid-liquid transition of aqueous ionic liquids is a thermally responsive phenomenon with phase separation. The phase separation can be used for forward osmosis desalination which directly utilizes a low-grade of thermal energy. By using MD simulations, I describe the local molecular environment during the transition and the driving force. The unusual trend of osmotic strength of the ionic liquids is explained with a suggested definition of an apparent free ion ratio. MD simulations are also used to study the amorphous phases and their phase transition of sugar alcohols in nanopores. The nano-encapsulation is proposed to shift the melting temperature and here I suggest a methodology to determine the phase transition temperature of encapsulated materials. This thesis also uses a theoretical approach to explore the thermal conductivity of the nanoconfined composites. Phonon frequency analysis verifies the enhancement of heat transfer by the infusion of phase change materials to the frameworks due to additional heat pathways between the nanoporous structures. Finally, I propose a practical design for a thermal rectifier that can be realized by phase change materials and derive a general theory for the design. The general theory indicates the possibility to obtain a high thermal rectification from the design and introduces the critical parameters for theoretical maximal performance.

Dedicated to my family

Table of Contents

List of Figures	iv
List of Tables.....	ix
Acknowledgments.....	xi
Chapter 1 Introduction	1
1.1 Basic principle of Molecular Dynamics simulation	2
1.2 Molecular Dynamics principles for heat transfer and phase analysis	6
1.2.1 Thermal conductivity	6
1.2.2 Phase analysis.....	7
1.3 Organization of this dissertation.....	9
Chapter 2 Liquid-Liquid phase transition with lower critical solution temperature (LCST) for forward osmosis draw solutes.....	10
2.1 Introduction	10
2.2 Molecular interactions for LCST behavior.....	13
2.2.1 Problem statement.....	13
2.2.2 Experimental observation.....	14
2.2.3 Molecular Dynamics simulation setup.....	18
2.2.4 Molecular Dynamics simulation results.....	23
2.3 Osmotic strength of LCST ILs	28
2.3.1 Problem statement.....	28
2.3.2 Experimental observation.....	31
2.3.3 Molecular Dynamics simulation setup.....	32
2.3.4 Molecular Dynamics simulation results.....	35
Chapter 3 Anomalous phase change of sugar alcohols encapsulated in nanopores for thermal applications	39
3.1 Introduction	39
3.2 Problem statement	40
3.3 Model and method.....	41
3.4 Structure analysis.....	46
3.4.1 ZIFs containing erythritol.....	46

3.4.2 Encapsulated erythritols	48
3.5 Melting temperature of encapsulated erythritols	49
3.6 Thermal conductivity.....	57
Chapter 4 Thermal rectification via heterojunctions of solid-state phase change materials.....	62
4.1 Introduction	62
4.2 Problem statement	63
4.3 Theoretical model	64
4.3.1 Heterojunction design	64
4.3.2 General theory	65
4.3.2 Criteria to determine phase situations	73
4.3.4 Adjustment method for extended conditions.....	75
4.4 Case study.....	75
4.4.1 Applied materials.....	75
4.4.2 General theory results.....	76
4.4.3 Global optimal solution.....	78
Chapter 5 Summary and future works	84
5.1 Summary of this dissertation	84
5.2 Recommendations for future work	85
5.2.1 Low Critical Solution Temperature (LCST) behavior	86
5.2.2 Enthalpy of fusion and phase transition temperature of phase change materials.....	86
5.2.3 Strategy for tunable phase transition temperature.....	87
References.....	88

List of Figures

Figure 1-1. Hierarchy of computational methods at certain length and time scales.

Figure 1-2. Single CPU cost in seconds per-atom per-time step versus year for the representative potentials. The line represents a doubling in computational cost every two years.

Figure 1-3. (a) Radial distribution functions of solid ($T = 50$ K), liquid ($T = 80$ K), and gaseous argon ($T = 300$ K). The radii are given in reduced units of the molecular diameter σ . (b) Spatial distribution functions of the hydration shell water. The deuterium atoms and the oxygen atoms are shown in yellow and red color where at over a certain threshold times of average density, respectively.

Figure 2-1. Schematic diagram and visualization of LCST behavior. The subclass of ionic liquids undergoes a thermo-responsive liquid-liquid phase transition of either UCST or LCST. A water/LCST IL mixture is miscible for all concentration below the critical temperature. The phase separation as function of temperature is visualized by a Nile red dye which is only dissolved by IL in the mixture.

Figure 2-2. Illustration of the proposed FO desalination system. A contaminated feed stream undergoes pre-treatment and enters an FO module in which the higher concentration IL draw solute causes water molecules from the feed to diffuse through the membrane owing to the natural osmotic gradient. The diluted draw then flows into a thermal separator using low grade heat source to cause a rise in temperature. Liquid-liquid phase separation occurs as the temperature increase above LCST, with the denser IL-rich phase settling at the bottom while the water-rich phase is on top. The former is recycled as the draw for FO, while the water-rich phase with residual IL content undergoes a low pressure nanofiltration polishing step to attain high quality product water.

Figure 2-3. Dynamic light scattering cumulant analysis results for particle size versus temperature. (a) Particle size versus temperature of $[P_{4444}][DMBS]H_2O$ 50 wt.% over the fully miscible region and phase separated regions of the phase diagram. Phase separation temperature, T_c ca. 36 °C (b) Particle size distribution of a $[P_{4444}][BnzSO_3]H_2O$ 50 wt.% mixture versus temperature.

Figure 2-4. Molecular structures and partial atomic charges of (a) the $[P_{4444}]$ cation, (b) the $[DMBS]$ anion (c) the $[BnzSO_3]$ anion and (d) the four-site based water molecule. The mostly charged atom represents the position of each molecules. i.e. the P atoms, S atoms, S atoms and O atoms, respectively, are taken as reference sites of the $[P_{4444}]$ cation, the $[DMBS]$ anion the $[BnzSO_3]$ anion and water molecule for further analysis.

Figure 2-5. RDFs from MD simulations for the 50 wt.% $[P_{4444}][DMBS]H_2O$ system. (a) cation-

anion (b) cation-cation (c) anion-anion (d) water-water (e) water-cation and (f) water-anion pairs.

Figure 2-6. Radial distribution functions (RDFs) calculated from MD simulations for the 49.6 wt.% [P₄₄₄₄][BnzSO₃] IL|H₂O system in different temperature conditions: (a) cation-anion, (b) cation-cation, (c) anion-anion, (d) water-water (e) water-cation and (f) water-anion pairs.

Figure 2-7. Calculated the number of hydrogen bonds for the 50 wt.% IL|H₂O system. (a-b) RDFs between oxygen and hydrogen for the 50.8 wt.% [P₄₄₄₄][DMBS] IL|H₂O system. (a) Oxygen of sulfite in anion-Hydrogen in water, (b) Oxygen in water-Hydrogen in water pairs. Vertical dashed lines denote O-H separation to define hydrogen bonding. (c) Number of hydrogen bonds as a function of temperature per each oxygen atom for both 50 wt.% of [P₄₄₄₄][DMBS] and [P₄₄₄₄][BnzSO₃] with water solution. Error bars present the range of recorded data from MD per 1 ps.

Figure 2-8. The HOH angle distribution of water molecules in the 50.8 wt.% [P₄₄₄₄][DMBS] IL|H₂O system calculated from MD simulations with a flexible water model based on a four-site water model of TIP4P/2005. In spite of the analysis to verify the contribution of dipoles relative to the ions, the dependency of average HOH angle on the temperature is not observed.

Figure 2-9. UV-Vis transmittance measurements used to determine cloud points as a function of IL-water concentration for LCST determination of (a) [P₄₄₄₄][DMBS] and (b) [P₄₄₄₄][TFA]. Concentrations of 70 wt.% (in red), 40 wt.% (in blue) and 10 wt.% (in yellow) are shown.

Figure 2-10. Binodal phase diagram of aqueous mixtures of [P₄₄₄₄][DMBS] and [P₄₄₄₄][TFA] which show the LCST behavior.

Figure 2-11. Viscosity of aqueous mixtures of [P₄₄₄₄][DMBS] and [P₄₄₄₄][TFA] as a function of concentration.

Figure 2-12. Osmotic strength of [P₄₄₄₄][DMBS] and [P₄₄₄₄][TFA] (a) Measured osmolality and calculated osmotic pressure, with dilute mixtures shown in the inset. (b) Osmolality measured as a function of molality showing deviations from ideal mixtures.

Figure 2-13. Molecular structures and partial atomic charges of the (a) P₄₄₄₄ cation, (b) DMBS anion, (c) TFA anion and (d) the rigid TIP4P water model.

Figure 2-14. Radial distribution functions (RDFs) calculated from MD simulations of solutions of P₄₄₄₄DMBS at different concentrations between a water molecule and (a) the P atom in the P₄₄₄₄ cation, (b) the S atom in the DMBS anion, (c) center of the benzene ring in the DMBS anion.

Figure 2-15. Radial distribution functions (RDFs) calculated from MD simulations for solutions of P₄₄₄₄TFA at different concentrations between water molecules and (a) the P atom in the P₄₄₄₄ cation, (b) the C2 atom in the TFA anion.

Figure 2-16. Molecular dynamics simulation showing the number of water molecules in the first coordination shell per ion pair of [P4444][DMBS] (line graph) and the ratio of water molecules contributing to their shells (area graph).

Figure 2-17. Preliminary single ion MD simulations (a) Radial distribution functions (RDFs) between a water molecule and the pivot atoms for hydration shells. Dotted lines denote the radius of the first coordination shell. (b) Normalized histogram of the number of water molecules in their first coordination shell.

Figure 2-18. Apparent free ion ratio by two hypothetical definition of free ion. (a) Molecular dynamics simulation showing the apparent free cation and anion ratio for DMBS compared to experimental data under two assumptions. (b) Molecular dynamics simulation showing the apparent free ion ratio for DMBS (in blue) and TFA (in red) compared to experimental data under the hypothesis that water molecules contribute to the osmotic strength of the nearest ion only.

Figure 3-1. Structure of (a) pristine ZIF-8 (*sod*, lattice constant, $a=b=c=16.99 \text{ \AA}$) and (b) ZIF-11 (*rho*, lattice constant, $a=b=c=28.76 \text{ \AA}$), both functioning as framework, and (c) erythritol as the phase change material. For each ZIF structure, Zn ions are represented as tetrahedra and the largest cavity in the pores by a yellow sphere that fits into the framework without touching any atoms. H atoms are omitted here for clarity but were included in the MD simulations.

Figure 3-2. Structural analysis of ZIF-8 (top row) and ZIF-11 (bottom row) containing various numbers of erythritol molecules. (a,d) Effect on lattice constant according to the number of erythritol molecules per pore. (b,e) Absolute displacement (center of mass) of erythritol molecules from an origin time. Only a representative subset of molecular trajectories (10 in b, 16 in e) is shown here for visibility. (c,f) Accessible internal cavity size as determined by the maximum distance among trajectories of each erythritol molecule.

Figure 3-3. Radial distribution function among erythritol molecules inside ZIF-8 (top row) and ZIF-11 (bottom row). (a,c) RDF between the mid-carbon (CT_m) atoms. (b,d) RDF between terminal-oxygen (O_t) atoms and mid-hydrogen (HO_m) atoms

Figure 3-4. Mean squared displacement. (a) Conceptual examples of two idealized systems (bulk liquid, bulk solid) and the confined liquid system. (b) The split of movement of an SA molecule into circumferential (*ds*) and radial (*dr*) directions based on the spherical symmetry of a ZIF pore.

Figure 3-5. Mean squared displacement of erythritol molecules inside ZIF pores. (a) 5pP in ZIF-8. (b) 16pP in ZIF-11. The saturated trend of MSD at long times shows that erythritol molecules cannot diffuse between the ZIF pores.

Figure 3-6. Mean squared displacements of encapsulated erythritol as a function of temperature,

evaluated at the 5 different sampling times listed in panel (b,top). We decompose these displacements into the radial direction (dr^2 ; upper plot in each pair) and along the surface of the ZIF's approximately-spherical pore (ds^2 ; lower plot in each pair), as indicated in Fig. 3-4b. (a) 3pP in ZIF-8. (b) 5 pP in ZIF-8. (c) 4 pP in ZIF-11. (d) 16 pP in ZIF-11. In each case the melting temperature, T_m , is determined and indicated by a vertical red dashed line. For each sample, we define its T_m such that for all $T < T_m$ the ds^2 data is practically independent of t_s for $1.0 \text{ ps} \leq t_s \leq 2.5 \text{ ps}$, while for all $T > T_m$ the ds^2 data increases significantly with increasing $t_s \geq 1.0 \text{ ps}$.

Figure 3-7. Radial distribution function at possible hydrogen bonding pairs between SAs and ZIF-8. If hydrogen bonds were present, a strong first peak would show up around 2 Å. (a) Pairs between HO_t atom in erythritol and four types of non-hydrogen atoms in ZIF-8. (b) Pairs between HO_m atom in erythritol and four types of non-hydrogen atoms in ZIF-8. (c) Pairs between oxygen atoms in erythritol and hydrogen atoms in ZIF-8. In all cases no hydrogen-bonding peaks are seen.

Figure 3-8. (Like Fig. 3-7 but here for ZIF-11). Radial distribution function at possible hydrogen bonding pairs between SAs and ZIF-11. If hydrogen bonds were present, a strong first peak would show up around 2 Å. (a) Pairs between HO_t atom in erythritol and six types of non-hydrogen atoms in ZIF-11. (b) Pairs between HO_m atom in erythritol and six types of non-hydrogen atoms in ZIF-11. (c) Pairs between oxygen atoms in erythritol and hydrogen atoms in ZIF-11. In all cases no hydrogen-bonding peaks are seen.

Figure 3-9. (a) Normalized heat current autocorrelation function and (b) thermal conductivity by using the Green-Kubo method as a function of correlation time, both for the pristine ZIF-8 at 400 K.

Figure 3-10. Thermal conductivity of pristine ZIFs and their composites with encapsulated erythritols. (a) ZIF-8 and its composites. (b) ZIF-11 and its composites. In each panel the cold and hot temperatures were chosen to ensure that the erythritol acts fully solid-like and liquid-like, respectively. Error bars show the maximum and minimum values from repeated calculations.

Figure 3-11. Phonon analysis by Fourier transform of the normalized HCACF and VACF at 400 K. (a) Comparison between pristine ZIF-11 and the case of 16pP in ZIF-11. The inset shows the 10-50 THz range in more detail. (b) Comparison between pristine ZIF-8 and the case of 5pP in ZIF-8. (c) Pure liquid erythritol. (d) VDOS comparison between pristine ZIF-8 (left) and the case of 5pP in ZIF-8 (right). Shaded bands indicate the enhanced heat transfer originating from the contributions of the edge atoms of erythritol, namely O (<2 THz, blue shading) and HO & HC (~40 THz, yellow shading).

Figure 4-1. Basic concept of thermal rectification. Analogous to the electrical diode, the thermal

rectifier transmits heat more easily in one direction than in the reverse direction. The subscript HL and LH indicate the direction of heat flux, from high (H) to low (L) temperature, or vice versa.

Figure 4-2. Heterojunction using two phase change materials in series. Schematic geometry of the suggested junction. The black line represents the temperature profile within the structure when phase changes exist in both A and B materials

Figure 4-3. Thermal resistance circuit diagram for the heterojunction design comprised of two phase-change materials.

Figure 4-4. Thermal bias dependent thermal rectification via a heterojunction between polyethylene (material A) and tungsten doped VO₂ (material B) as detailed in Table 4-5. Regimes with different slopes represent different combinations of phase change states between the two materials Two representative states yielding different thermal rectification trends are detailed in the inserts.

Figure 4-5. Optimal thermal rectification with respect to a selected design parameter, the length ratio l_A/l_B . The 3D mesh graph shows the existence of local and general optimization points for thermal rectification. (Other parameters are detailed in Table 4-5)

Figure 4-6. Optimal thermal rectification with respect to phase change temperature at the defined length ratio, (a) $l_{VO_2}/l_{Polyethylene} = 2$, (b) $l_{VO_2}/l_{Polyethylene} = 4$ and (c) $l_{VO_2}/l_{Polyethylene} = 8$. The area inside the black line in each figure has the same thermal rectification factor γ and the maximum value of γ . The black dashed lines mean the condition the VO₂ has the same phase change temperature with the polyethylene as 320 K. The magenta dashed line in (b) corresponds to the condition of the case study at Fig. 4-4. (Other parameters are detailed in Table 4-5)

Figure 4-7. Maximal thermal rectification γ_{max} with $T_A^* = T_B^*$ condition at each length ratio. The green line is the solution of γ for the case of a phase change in material A in both directions and the red line is the solution for that in material B. The global maximal rectification is observed at the intersection between the two solutions. The theoretical maximal rectification is based on the geometric mean of the thermal conductivity ratio of the two materials as expressed as

$\sqrt{\frac{k_{A,L} k_{B,H}}{k_{A,H} k_{B,L}}} - 1$ with the optimized length ratio of $\frac{l_A}{l_B} = \sqrt{\frac{k_{A,L} k_{A,H}}{k_{B,L} k_{B,H}}}$. (Other parameters are detailed in Table 4-5)

List of Tables

Table 1-1. The representative empirical potentials for MD simulations and comparisons. The potentials are summarized with typical systems they model, time step size. The CPU cost of potentials is normalized by that of Lennard-Jones potential. The last 3 ones are for comparison with DFT calculation by VASP. The details for each calculation are described on LAMMPS benchmark webpage.

Table 2-1. Van der Waals parameters for the force field in molecular dynamics simulations.

Table 2-2. Bond parameters of the flexible water model for Morse potential force field in molecular dynamics simulations.

Table 2-3. Bond parameters for the harmonic potential force field in molecular dynamics simulations.

Table 2-4. Angle parameters for the harmonic potential force field in molecular dynamics simulations.

Table 2-5. Dihedral parameters for the force field in molecular dynamics simulations.

Table 2-6. Van der Waals parameters for the force field in molecular dynamics simulations.

Table 2-7. Bond parameters for the harmonic potential force field in molecular dynamics simulations.

Table 2-8. Angle parameters for the harmonic potential force field in molecular dynamics simulations.

Table 2-9. Dihedral parameters for the force field in molecular dynamics simulations.

Table 2-10. The number of ion pairs of the [P₄₄₄₄][DMBS] and [P₄₄₄₄][TFA], and water molecules in the MD studies in order to match with the mass fraction conditions at the experiments.

Table 3-1. Force field parameters for ZIF-8 framework.

Table 3-2. Force field parameters for ZIF-11 framework.

Table 3-3. Force field parameters for erythritol.

Table 3-4. Simulation system size for the encapsulated erythritol in ZIF-8.

Table 3-5. Simulation system size for the encapsulated erythritol in ZIF-11.

Table 4-1. Total possible phase change cases with respect to the inequalities between the phase change temperatures and boundary temperatures for the q_{LH} direction.

Table 4-2. Total possible phase change cases with respect to the inequalities between the phase change temperatures and boundary temperatures for the q_{HL} direction.

Table 4-3. Heat flux relations for q_{LH} with corresponding criteria. The criteria on columns and rows independently determine the existence of phase change in material A and B, respectively.

Table 4-4. Heat flux relations for q_{HL} with corresponding criteria. The relation on the second column is about the state of the absence of phase change in both materials.

Table 4-5. Material properties used for the calculation in this manuscript for polyethylene (material A) and tungsten doped VO₂ (material B).

Acknowledgments

I consider myself very fortunate to have a challenging and rewarding life at Berkeley with supportive, brilliant, passionate scholars and friends. I would like to take a moment to express my deep gratitude to those who helped me finally finish this dissertation.

First of all, I cannot imagine myself completing a Ph.D. degree without my advisors, Jeff Urban and Chris Dames. Jeff Urban encouraged me to seek challenging questions and taught me an attitude for pursuing science. His enthusiasm and encyclopedic knowledge broaden my horizon by introducing extensive learning and incredible collaboration opportunities. Chris Dames epitomizes the definition of a mentor. He prioritizes genuine care and advocates for his students at every moment. Needless to say, his expertise and creativity guided me in the right direction of researches. I sincerely hope to emulate even a fraction of their examples in the future.

It was huge luck that I can work on the Molecular Foundry in Lawrence Berkeley National Laboratory (LBNL). I have experienced a lot of interdisciplinary collaborations and interacted with many enthusiastic researchers. Particular thanks go to Woochul Lee, Peter (Fan) Yang, Chih-Hao Hsu, David Suich, Ngoc Bui and Akanksha Menon. Their critical insight and encouragement motivated me to become a sincere Ph.D. I also remember the warm hands from Maddie Gordon, Lukas Hackl, Jaeyoo Choi, Joseph Schaadt and Anne Pham physically and mentally. They always have welcomed me when I need scientific discussion, brainstorming, language improvement and break.

Throughout my years at Berkeley, I have been always surrounded by great friends. Many thanks go to Donggun Lee, Jinsol Kim, Joonwoo Kim, Hyungtaek Kim, Won Hee Ko, Suhong Moon and Sareum Kim. I also would like to thank the tennis club friends, IM league soccer team members, golf buddies and travel mates who shared unforgettable memories with me. From applying to graduate schools to sharing life experience and knowledge in the U.S., KIST fellas have helped me a lot. I appreciate and respect Jai Hyun Koh, Junbeom Pyo, Jaeyune Ryu and Junha Roh.

I am grateful for the funding supports from DOE via LBNL and Kwanjeong Educational Foundation which allowed me to pursue my studies and researches.

Finally, to my parents and brother, I am deeply thankful for unwavering support and love. Whenever I was not confident, you have shown me unerring trust at every stage of my life. This dissertation is dedicated to you.

Chapter 1

Introduction

Worldwide, energy demand has been increasing due to many factors such as population increase, climate change, and improved quality of human life. Although electricity operates as the primary energy form due to its convenient transportability, transformability, and storability, one-third of total energy in the U.S. is used as thermal energy at the residential consumer side [1]. Even some portion of electricity generated by conventional thermodynamics cycles is converted back to thermal energy. Since electrical energy in nature is not proper to consume directly, it requires power plants and/or transferring systems which make the electricity relatively expensive. Beside converting thermal energy for use in electricity-dependent systems, thermal energy has also been considered for direct use by utilizing such resources as solar power and waste heat.

In every field, computational simulations are utilized to complement and guide experiments because simulations can reveal phenomena which lack direct experimental access. They can also save cost for research and development by suggesting the promising candidates of materials, configurations, and designs. Simulations can sometimes be even more appropriate and precise than traditional experiments as we can freely control environmental parameters, such as conditions of extremely high and low temperatures or pressures.

Especially in the heat transfer field, the finite element methods with the continuum equations are typically used to simulate energy and mass transports in a system. However, the recent interests in micro/nanoscale materials to overcome the current barriers of thermal energy systems require the fundamental understanding of unforeseen science which cannot be explored by the continuum-based approaches. To treat the aspects of various phenomena for particular length and time scales, several methods have been developed and widely used at those suitable scales, as presented in Fig. 1-1. Especially, molecular dynamics (MD) simulations are effective to cover structures of nanoscale and interfacial phenomena of materials. Thanks to the recent rapid growth of performance of computing resources, the simulations allow us to predict a phenomenon in more detail and more precisely.

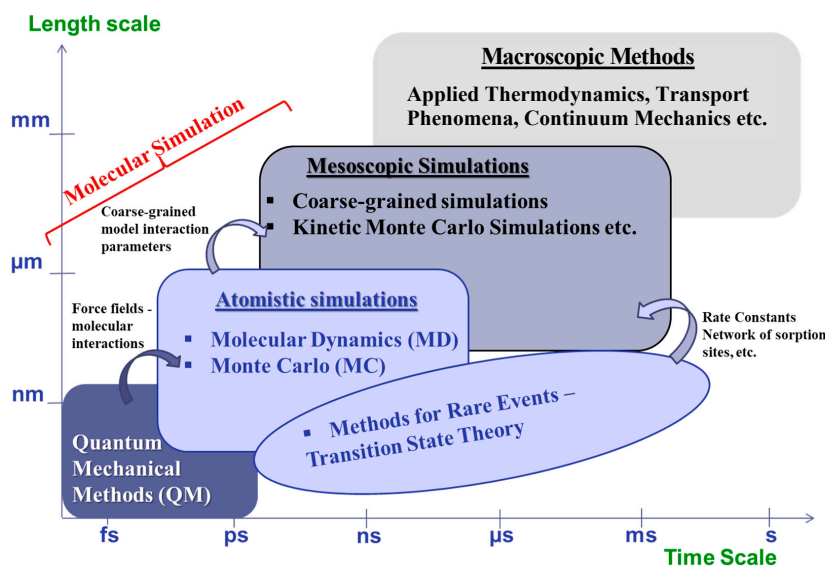


Figure 1-1. Hierarchy of computational methods at certain length and time scales. *Adapted from open source [2].*

This dissertation will mainly discuss unconventional phase transition materials for thermal applications. The theoretical understanding of the anomalous phases and their transitions can suggest the guidance to determine the bottleneck of current materials and then to develop new materials. MD simulations are mainly used to study the thermal characteristics of phase transition materials and the radical changes at their transitions at the atomistic level. In this introductory chapter, I will explain the basic principles of MD simulations and the detailed methodologies for thermal and phases analysis. The introduction and motivation for problematic issues associated with thermal applications that I am interested in will be introduced separately in each chapter.

1.1 Basic principle of Molecular Dynamics simulation

Although quantum mechanics described by the Schrodinger equation can consider detailed potential generated by the electrons and the energy levels and wavefunction of a molecule, a quantum molecular dynamics simulation, which is usually called density functional theory (DFT), can only treat the system region of a few hundred atoms in size and picoseconds order in time. The Born–Oppenheimer (BO) approximation is the first step to simplify the physics by reducing the electronic degrees of freedom for the classical MD simulation. BO approximation assumes the motion of atomic nuclei and electrons in a molecule can be treated separately, based on the fact that the nuclei are much heavier than the electrons. In MD simulation, atoms are treated as spherically symmetric particles which only have the translational motion, and the quantum mechanical motion governed by the Schrodinger equation is replaced by Newton's second law of classical mechanics,

$$f_i = m_i \frac{d^2 r_i}{dt^2} = m_i a_i, \quad (1.1)$$

where m_i is the mass of the i -th atom and f_i is the sum of the forces exerted on the atom by the other atoms in the system, r is the position vector of the atom, and t is the time. The force vector f_i is calculated from the interatomic potential energy, U , acting on the atom,

$$f_i(t) = -\frac{\partial U}{\partial r_i(t)} = -\nabla U. \quad (1.2)$$

The choice of potential is one of the most important aspects of the practical implementation for the MD simulations. A potential, also called a force field, is determined with the consideration of the system type (metal, covalent bonded organic, solution), the phenomena of interest (flexibility, transferability, polarization), the computational resource, and desired accuracy [3]. Table 1-1 summarizes the benchmark results of representative interatomic potentials in MD simulations. Thanks to the growing hardware performance, better accuracy and multifunctional potentials along with the computational complexity have been developed by following the trend of the familiar Moore's law as shown in Fig. 1-2.

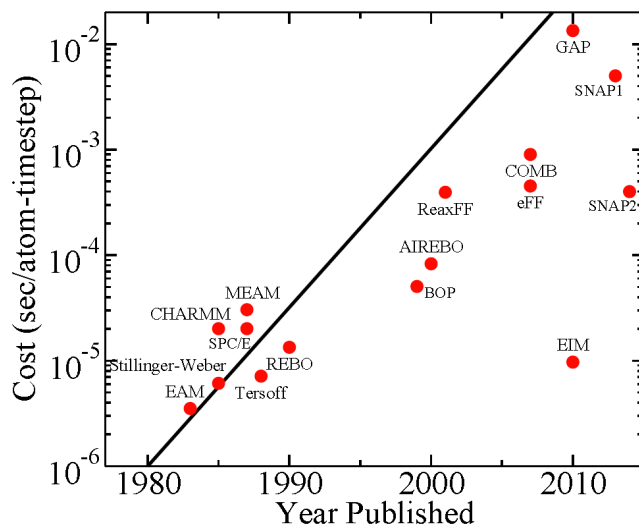


Figure 1-2. Single CPU cost in seconds per-atom per-time step versus year for the representative potentials. The line represents a doubling in computational cost every two years [4]. *Copyright* © *Materials Research Society* 2012

Table 1-1. Representative empirical potentials for MD simulations and comparisons. The potentials are summarized with typical systems they model and time step size. The CPU cost of potentials is normalized by that of Lennard-Jones potential. The last 3 rows are for comparison with DFT calculation by VASP. The details for each calculation are described on the LAMMPS benchmark webpage [5].

Potential	System	# Atoms	Timestep	CPU cost*	LJ Ratio
Granular	chute flow	32000	0.0001 tau	2.08e-7	0.26x
FENE bead/spring	polymer melt	32000	0.012 tau	2.86e-7	0.36x
Lennard-Jones	LJ liquid	32000	0.005 tau	8.01e-7	1.0x
DPD	pure solvent	32000	0.04 tau	1.22e-6	1.53x
EAM	bulk Cu	32000	5 fs	1.87e-6	2.34x
REBO	polyethylene	32640	0.5 fs	3.18e-6	3.97x
Stillinger-Weber	bulk Si	32000	1 fs	3.28e-6	4.10x
Tersoff	bulk Si	32000	1 fs	3.74e-6	4.67x
ADP	bulk Ni	32000	5 fs	5.58e-6	6.97x
EIM	crystalline NaCl	32000	0.5 fs	5.60e-6	6.99x
Peridynamics	glass fracture	32000	22.2 ns	7.46e-6	9.31x
SPC/E	liquid water	36000	2 fs	8.77e-6	11.0x
CHARMM+PPPM	solvated protein	32000	2 fs	1.13e-5	14.1x
MEAM	bulk Ni	32000	5 fs	1.32e-5	16.5x
Gay-Berne	ellipsoid mixture	32768	0.002 tau	2.20e-5	27.5x
BOP	bulk CdTe	32000	1 fs	2.51e-5	31.3x
AIREBO	polyethylene	32640	0.5 fs	3.25e-5	40.6x
ReaxFF/C	PETN crystal	32480	0.1 fs	1.09e-4	136x
COMB	crystalline SiO2	32400	0.2 fs	2.00e-4	250x
eFF	H plasma	32000	0.001 fs	2.16e-4	270x
ReaxFF	PETN crystal	16240	0.1 fs	2.84e-4	354x
VASP/small	water	192/512	0.3 fs	26.2	17.7e6x
VASP/medium	CO2	192/1024	0.8 fs	252	170e6x
VASP/large	Xe	432/3456	2.0 fs	1344	908e6x

* The unit of CPU cost: secs/atom/step

The numerical integration of Newton's equation of motion is another primary aspect of MD. The most used algorithm is the *velocity Verlet* algorithm [6]. Although the form of motion equation depends on the boundary condition and any constraints on the system, the basic form at

the condition with a constant number of atoms, volume, and energy in the system is described as follows. This algorithm is similar to the *leapfrog* algorithm, however, note that it is not necessary to keep track of the velocity at every time step, and the force at the next time step only depends on position not velocity at the next time step.

$$r_i(t + \Delta t) = r_i(t) + v_i(t)\Delta t + \frac{1}{2!} \frac{f_i(t)}{m_i} \Delta t^2 + O(\Delta t^3). \quad (1.3)$$

$$v_i(t + \Delta t) = v_i(t) + \frac{f_i(t) + f_i(t + \Delta t)}{2m_i} \Delta t + O(\Delta t^3). \quad (1.4)$$

The timestep-by-timestep movement of every molecule from an initial state provides the macroscopic physical properties of the substance such as temperature, pressure, potential energies, etc. through statistical methods. The notion of ensemble (statistical ensemble) is an idealization of an assembly of all possible microstates consistent with constraints imposed macroscopically. The *ergodic hypothesis* says that the average of trajectories over a long period of time will reproduce the statistical average of all accessible microstates at a given set of conditions.

The most interesting and representative physical properties are temperature and pressure. Temperature is calculated by the microscopic approach by the *equipartition energy theorem*. The theorem explains that each classical degree of freedom of a freely moving particle has an average kinetic energy, E_k , of $k_B T/2$ in equilibrium at absolute temperature T where k_B denotes Boltzmann's constant. Thus, the temperature of a system of N atoms in a 3-dimensional MD simulation is calculated as

$$\langle E_k \rangle = \left\langle \sum_i^N \frac{p_i^2}{2m_i} \right\rangle = \frac{3}{2} N k_B T, \quad (1.5)$$

where p_i is the momentum of particle i . The angular bracket means the ensemble average, however as mentioned, it can be replaced by time average based on the *ergodic hypothesis*. The pressure of a simulation system is computed by virial expression from classical mechanics.

$$\langle P \rangle V = N k_B T + \langle W \rangle, \quad (1.6)$$

where W is the virial term defined in a 3-dimensional system as

$$W = \frac{1}{3} \sum_{i=1}^N r_i \cdot f_i. \quad (1.7)$$

1.2 Molecular Dynamics principles for heat transfer and phase analysis

1.2.1 Thermal conductivity

Phonons, the quantum mechanical description of vibrational motion, are the primary heat carrier in insulators and semiconductors. The MD simulation is one of the best techniques to observe the dynamics of lattice vibration. Although being based on classical mechanics with a lack of consideration of quantum effects, such as zero-point energy or quantization of phonon energy levels, which leads to lower accuracy at low temperature [7], the MD simulation has the further advantages of implicitly modeling the anharmonic phonon-phonon interaction to all orders [8]. The phonon frequency provides valuable insight into the understanding of thermal transport behavior as well as the thermal conductivity prediction. There are two commonly used methods to calculate the thermal conductivity: the non-equilibrium molecular dynamics (NEMD) simulation and the equilibrium molecular dynamics (EMD) simulation.

The representative method of EMD simulation is the Green-Kubo method. The Green-Kubo method computes lattice thermal conductivity based on the fluctuation-dissipation theorem [9] of heat current, which is based on the linear response theory [10]. The Green-Kubo formula for thermal conductivity in a 3-dimensional system is

$$k = \frac{1}{3k_B T^2 V} \int_0^\infty \langle \vec{J}(0) \cdot \vec{J}(t) \rangle dt, \quad (1.8)$$

where T is the system temperature, V is the system volume, $\vec{J}(t)$ is the heat current, and so $\langle \vec{J}(0) \cdot \vec{J}(t) \rangle$ is the heat current autocorrelation function (HCACF). The heat current is given by

$$\vec{J}(t) = \frac{d}{dt} \sum_i^N r_i E_i, \quad (1.9)$$

where r_i and E_i are the position and total energy of particle i . The HCACF naturally decays to zero, however, numerical evaluation needs an adequate integral time length to obtain a converged value of thermal conductivity. One of the promising candidates for the integral time is the correlation length [11].

The “direct method” of NEMD simulation is based on Fourier's law of heat conduction below with an imposed temperature gradient, akin to a typical measurement mechanism in experimental methods.

$$k = -\frac{J}{\nabla T}, \quad (1.10)$$

where J and ∇T are the heat flux temperature gradient along the transport direction in the non-equilibrium steady state, respectively. The key step for this “direct method” is to build up the temperature gradient. The most common way imposes the local temperature at two regions by thermostats (heat source and sink) [12]. The energy added to the heat source region is extracted at the heat sink region, and it is proportional to the transferred heat flux between the two regions. Otherwise, a fixed amount of thermal energy is applied to and extracted from two heat baths [13]. The occurring temperature gradient between the two regions is used to calculate the thermal conductivity.

As the phonon mean free path is longer than the length scales of MD simulations (Fig. 1-1), the phonon-boundary scattering would occur at the interface with heat baths. The calculated thermal conductivity at NEMD simulations is influenced by the simulation sizes, which is known as the Casimir limit [14]. Since it is impossible to simulate a big enough to ignore the size effect, repeated simulations with different simulation size are required to extrapolate the thermal conductivity results to the infinite size system.

1.2.2 Phase analysis

As the first MD simulation is known as a phase transition study for a hard-sphere system by Alder and Wainwright in 1957 [15], MD simulations are naturally suitable to study phases of substances and their phase transition. The development of the MD simulation has demonstrated the possibility of the basic understanding of phase transition mechanism which is an evident example of molecular-scale phenomena on the macroscopic problem by following a bottom-up approach [16].

The radial distribution function (RDF), $g(r)$, has been widely used to understand the structural features of a system of particles. With a viewpoint of statistical mechanics, the RDF describes how number density varies as a function of distance from a reference particle. If $\rho_n = N/V$ is the average number density of the particles in a system, the $g(r)$ is defined as the ratio between the local density at a distance r from reference and ρ_n . Thus, the $g(r)$ for 3 dimensions is expressed as

$$g(r) = \frac{\rho(r)}{\rho_n} = \frac{dn(r)}{\rho_n 4\pi r^2 dr'} \quad (1.11)$$

where $n(r)$ is the number of particles within a shell of thickness dr .

The qualitative appearance of RDFs provides the information for phase identification as shown in Fig. 1-3a. The rapid molecular motion of liquid states compared to the crystalline solid shows its lack of long-range order, then further at gas phases. There is a clear long-range order in the crystalline solid. Amorphous solids (e.g., ordinary glass) that have no long-range order also can be distinguished by the time scale of the motion. Furthermore, the RDF informs quantitative information as well such as average bond length and the average number of bonds. The idea of the RDF is extended to the spatial distribution function (SDF) as a 3-dimensional density distribution with additional parameters of spherical angles, as shown in Fig. 1-3b.

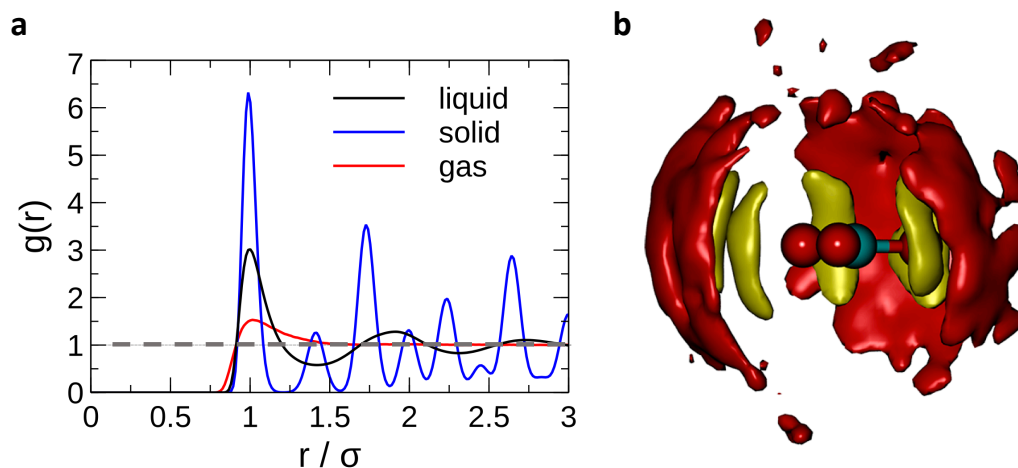


Figure 1-3. (a) Radial distribution functions of solid ($T = 50$ K), liquid ($T = 80$ K), and gaseous argon ($T = 300$ K). The radii are given in reduced units of the molecular diameter σ . *Adapted from open source* [17]. (b) Spatial distribution functions of the hydration shell water. The deuterium atoms and the oxygen atoms are shown in yellow and red color where at over a certain threshold times of average density, respectively. *Adapted from* [18]. Copyright © 2017, American Chemical Society.

1.3 Organization of this dissertation

This dissertation details molecular insight into the anomalous phases for thermal energy materials by using an atomistic computation technique, MD simulations, and suggests a thermal device design and its theoretical model, which can utilize the advantages of phase change materials. The chapter-by-chapter outline is as follows:

- Chapter 2 describes a molecular insight into the lower critical solution temperature (LCST) liquid-liquid transition of aqueous ionic liquids. The thermally responsive phenomenon provides a small enthalpy of phase separation from water, which then can be used for forward osmosis desalination. I discuss the local molecular environment during the transition and the driving force for aggregates upon heating by using MD simulations. To understand the unusual trend of osmotic strength of ionic liquid with LCST behavior, I also suggest a method to define an apparent free ion ratio which contributes to the osmotic pressure.
- Chapter 3 investigates the amorphous phases and their phase transition in nanopores. Sugar alcohols, as phase change materials, have been required to reduce their melting temperature. By utilizing MD simulations, I study the phase transition of encapsulated sugar alcohols on a molecular level and the shift of the melting temperature. The theoretical approach explores the thermal conductivity of the nanoconfined composites. Phonon frequency analysis provides the effect of the infusion of phase change materials to the frameworks and details of heat pathways.
- Chapter 4 suggests a practical design for a thermal device that can be realized by phase change materials. A thermal rectifier transmits heat more easily in one direction than in the reverse direction. Inspired by the thermal conductivity difference between phases, a heterojunction comprised of two phase-change materials shows the possibility to obtain a high thermal rectification. I derive a general theory for the heterojunction design with a consideration of where the phase changes happen. The general theory indicates the critical parameters for optimization.
- Chapter 5 summarizes the results of this dissertation and provides directions for future study.

Chapter 2

Liquid-Liquid phase transition with lower critical solution temperature (LCST) for forward osmosis draw solutes

Content in this chapter is adapted with permission from the following publication:

H. Kang[†], D. E. Suich[†], J. F. Davies, A. D. Wilson, J. J. Urban, R. Kostecki, “Molecular Insight into the Lower Critical Solution Temperature Transition of Aqueous Alkyl Phosphonium Benzene Sulfonates”, *Communications Chemistry*, **2**, 51, (2019)

Content in this chapter will be published as the following title:

A. Z. Haddad[†], A. K. Menon[†], H. Kang, J. J. Urban, R. S. Prasher, R. Kostecki, “Water Desalination Using Thermally-Responsive Ionic Liquids Regenerated by Solar Energy”, *under review as of Dec. 2020*

2.1 Introduction

Desalination, a process that separates salts and other contaminants from water, can be used to treat these non-traditional brines for beneficial reuse to meet the growing demand. While desalination technologies for seawater are well-established and highly optimized for potable use, non-traditional water sources are far more varied in their salinity and composition, thereby requiring new treatment methods beyond reverse osmosis (RO) [19]. For example, produced waters, which are a byproduct of oil and gas extraction, represent an under-utilized water resource – in the United States alone, nearly one million oil and gas wells generate ~2.4 billion gallons of water per day [20]. This water is typically disposed by deep-well injection, but increased regulation and economic incentives are pushing industry to explore treatment options that convert produced water into a value added commodity, *i.e.*, water for agricultural reuse.

Forward osmosis (FO) is considered to be one of the promising technologies for desalination of non-traditional waters and complex brines [21]. Recent literature on FO has shown that it exhibits a higher fouling and scaling resistance relative to RO [22,23], making it suitable for feeds of variable composition with minimal pre-treatment and membrane maintenance and/or replacement [24,25]. However, a FO desalination with traditional draw solutes comprising inorganic salts (*e.g.* sodium chloride) requires a second step to regenerate the draw and produce

clean water, which is very energy intensive. For example, sodium chloride can be recovered either by supplementing FO with RO that requires more electrical energy than direct treatment (*i.e.*, RO without FO) of the same feed [26], or by evaporating water in a thermal or membrane distillation process that is constrained by the enthalpy of vaporization of water ($\sim 2400 \text{ Jg}^{-1}$) [27,28]. Such large energetic inputs for regeneration of traditional inorganic draws often preclude FO as a competitive desalination technology.

A novel class of materials that can serve as potential draw solutes are thermo-responsive ionic liquids (ILs), pioneered by *Ohno* and coworkers [29-38]. The subclass of ionic liquids undergoes a thermo-responsive liquid-liquid phase transition of either an upper critical solution temperature (UCST) or lower critical solution temperature (LCST), as detailed in Fig. 2-1. In liquid-liquid mixtures with a LCST transition, a single and miscible phase appears at lower temperatures. However, upon heating above a critical temperature T_c , the single-phase liquid-liquid mixture separates into two immiscible phases. From a thermodynamic view, this behavior is understood in the framework of Eq. (2.1), where ΔG_{mix} is the free energy of mixing, ΔH_{mix} is the enthalpy of mixing, and ΔS_{mix} is the entropy of mixing.

$$\Delta G_{mix} = \Delta H_{mix} - T\Delta S_{mix}. \quad (2.1)$$

At lower temperatures, strong intermolecular interactions, such as hydrogen bonding, lead to a negative enthalpy of mixing and formation of a miscible phase between the two components. These intermolecular interactions are often highly directional and come at an entropic cost. Upon heating above T_c , the entropic term dominates as intermolecular interactions are broken, and the system entropy can increase by phase separation due increased degrees of freedom from the broken intermolecular interactions [39,40] or if dispersion forces between two like components (A-A) and (B-B) is greater than between unlike components (A-B) [41]. While this type of behavior has been observed for many polymer-solvent systems, there are fewer cases of small molecule LCST mixtures.

By avoiding the traditional first order phase transition prevalent in thermal regeneration mechanisms, the energy required for separation of water from ILs (*i.e.*, enthalpy of de-mixing) is approximately 10 Jg^{-1} , which is orders of magnitude lower [42,43]. Furthermore, from an enormous library of ionic liquids [44], a few ionic liquid combinations show this phase transition with a relatively low transition temperature $< 50 \text{ }^\circ\text{C}$. As a result, these thermo-responsive draw solutions can be coupled with a low-grade heat source such as solar-thermal energy or waste heat, which in turn significantly reduces the carbon footprint and cost of water treatment [45], as an example presented in Fig. 2-2.

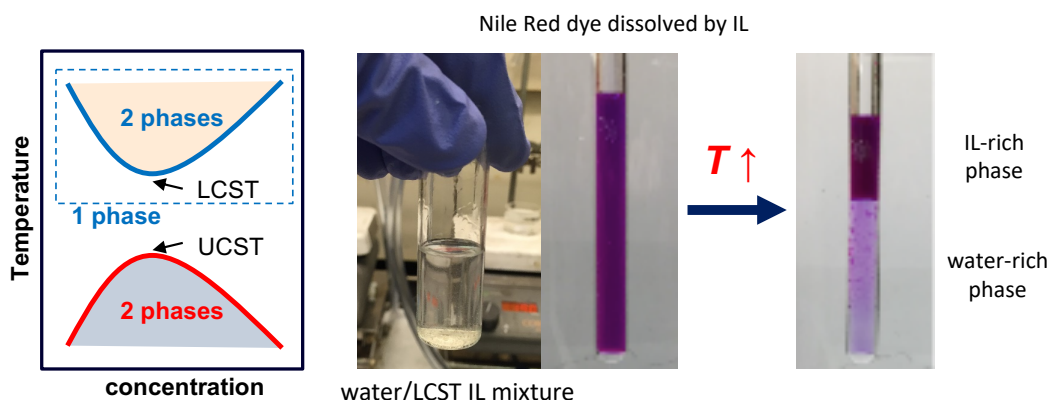


Figure 2-1. Schematic diagram and visualization of LCST behavior. The subclass of ionic liquids undergoes a thermo-responsive liquid-liquid phase transition of either UCST or LCST. A water/LCST IL mixture is miscible for all concentration below the critical temperature. The phase separation as function of temperature is visualized by a Nile red dye which is only dissolved by IL in the mixture.

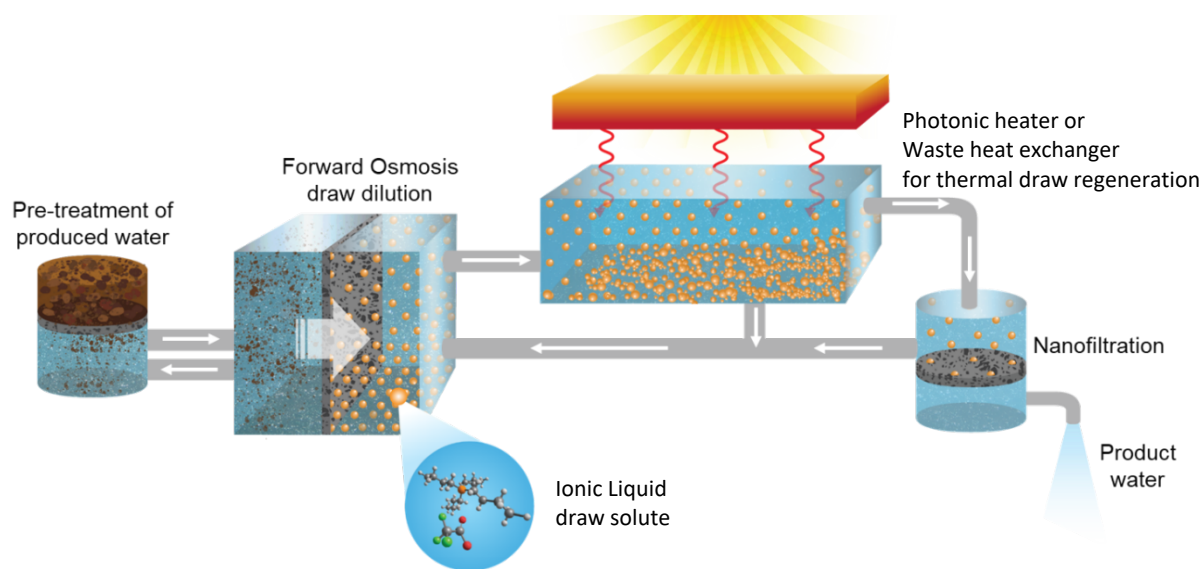


Figure 2-2. Illustration of the proposed FO desalination system. A contaminated feed stream undergoes pre-treatment and enters an FO module in which the higher concentration IL draw solute causes water molecules from the feed to diffuse through the membrane owing to the natural osmotic gradient. The diluted draw then flows into a thermal separator using low grade heat source to cause a rise in temperature. Liquid-liquid phase separation occurs as the temperature increase above LCST, with the denser IL-rich phase settling at the bottom while the water-rich phase is on

top. The former is recycled as the draw for FO, while the water-rich phase with residual IL content undergoes a low pressure nanofiltration polishing step to attain high quality product water.

2.2 Molecular interactions for LCST behavior

2.2.1 Problem statement

The argument for the physicochemical conditions necessary for LCST behavior between an ionic liquid and water mixtures is the balance between the hydrophilic and hydrophobic character of the component positive and negative ions [35]. If both the anion and cation are too hydrophobic, aqueous mixtures will be immiscible over the whole temperature range, and conversely, if both components are too hydrophilic, aqueous mixtures will remain fully miscible independent of temperature. In studying related protonated tertiary amines, our team has found that is not the total organic content of the molecular ions that drive this phenomena but the proximity of the organic content to the charged center [46].

Recent studies have attempted to understand the molecular interactions responsible for the IL-water LCST transition. FT-IR spectroscopic probing of tetrabutylphosphonium [P₄₄₄₄] 4-vinylbenzenesulfonate-water mixtures concluded that the C-H functional groups of the cation responded first to a temperature perturbation, followed by the sulfonate group of the anion. The mechanism proposed that the cation initiates conformational changes (due to greater hydrophobic interaction with water) forming single cation-anion ion pair aggregates due to strong coulombic forces [47]. A different IL|H₂O LCST mixture obtained by replacing the 4-vinylbenzenesulfonate anion with trifluoroacetate ([P₄₄₄₄][CF₃COO]), was studied to examine the hydrophilic nature of the ions using 1-propanol probing methodology. The results found that [P₄₄₄₄] showed equally strong hydrophilic and hydrophobic character, whereas the anion exhibited slightly hydrophobic character. The number of water molecules hydrating the cation was 10 times that of the anion and this large hydration shell of the cation results in an unfavorable entropy of mixing [48]. Cations are known to require greater hydration than anions [49], and the largely neutral polarity (neither polar nor non-polar) nature of the [P₄₄₄₄] further explains why to date much of the observed IL|H₂O LCST mixtures are based on quaternary ammonium and phosphonium cations [50].

Molecular Dynamics (MD) simulations demonstrated that the LCST transition of [P₆₆₆₈] and amino acid anions in aqueous solutions occur by temperature dependent changes in intermolecular interactions between the anion, cation, and water [51]. Specifically, the anion's functional groups, -NH₂ and -COOH, are able to form a hydrogen bond to the carboxylate group of another anion. Similar interactions between anions are believed to play a role in the self-assembly of tertiary amine bicarbonates [46]. With increasing temperature, the anion-water and

cation-anion interactions weaken, whereas anion-anion interactions increase, resulting in an LCST transition. Furthermore, radial distribution functions showed no clear interaction of $-\text{CH}_3$ groups of one anion to $-\text{COO}^-$ of another. Consequently, the proposed conclusions only represent a system specific mechanism as it cannot account for the LCST transition of tetralkylphosphonium benzene sulfonate derivatives [33] which have no hydrogen bond donor functional groups.

Currently, there exists disagreement in the literature about the molecular interactions responsible for the IL|H₂O LCST transition. In this part, I study the changes in LCST aqueous mixtures of tetrabutylphosphonium 2,4-dimethylbenzenesulfonate [P₄₄₄₄][DMBS] across temperatures ranges in both the fully miscible and phase separated regions to obtain further insight in the molecular mechanism of IL|H₂O phase separation. The aggregation of ILs is investigated experimentally and theoretically by using the dynamic light scattering method and the MD simulation, respectively.

2.2.2 Experimental observation

Experiments in this part were conducted by Dr. David E. Suich

Dynamic light scattering (DLS) is used to study the effects of aggregation and changes in long range order for LCST mixtures. For each experiment, scattering intensity versus delay time was collected, and then analyzed by software to give the distribution versus decay constant occurring by diffusion under Brownian motion. The decay constant, Γ , given by Eq. (2.2), is a function of the diffusion coefficient, D_t , and the scattering vector, q .

$$\Gamma = -D_t q^2. \quad (2.2)$$

The scattering vector is given by Eq. (2.3), where n_D is the refractive index of the material, λ is the wavelength and θ is the detection angle.

$$q = \frac{4\pi n_D}{\lambda} \sin\left(\frac{\theta}{2}\right). \quad (2.3)$$

From the analyzed decay time distribution and known scattering vector, the hydrodynamic diameter, D_h , of the scattering particle can be determined from Eq. (2.4).

$$D_h = \frac{k_B T}{3\pi\eta(T)D_t}. \quad (2.4)$$

where k_b is Boltzmann's constant, $\eta(T)$ is the viscosity and the D_t is the translational diffusion. Figure 2-3a shows the results for the particle size distribution versus temperature across the fully miscible region of a 50 wt.% (w/w) mixture of $[P_{4444}][DMBS][H_2O]$. Initially, at temperatures 10 °C below T_c , the solution shows minimal scattering aggregates, meaning the solution is homogenous within the length scale of sensitivity for the DLS apparatus. However, around 30 °C, the solution shows clear correlation with an average scattering size of 3-4 nm, which enlarges with increasing temperature up to 9 nm at 35 °C, just below T_c .

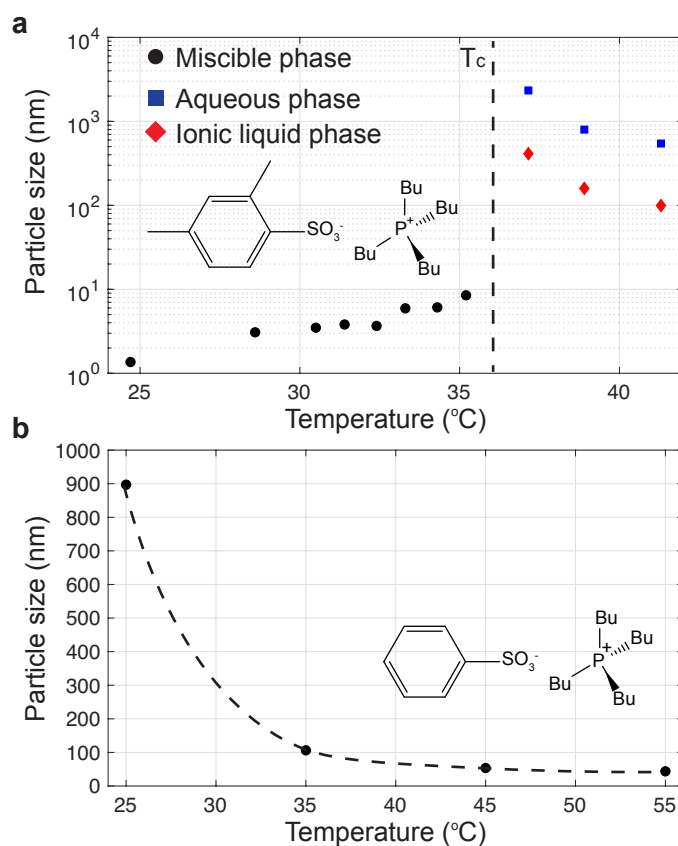


Figure 2-3. Dynamic light scattering cumulant analysis results for particle size versus temperature. (a) Particle size versus temperature of $[P_{4444}][DMBS][H_2O]$ 50 wt.% over the fully miscible region and phase separated regions of the phase diagram. Phase separation temperature, T_c ca. 36 °C (b) Particle size distribution of a $[P_{4444}][BnzSO_3][H_2O]$ 50 wt.% mixture versus temperature.

The aggregate size growth follows DLS measurements of a different LCST aqueous mixture with $[P_{4444}][CF_3COO]$, which showed a similar increase in particle size with increasing

temperature leading up the critical point [52]. This observation was also supported by additional experimental techniques and it was assigned to the surfactant free micellar formation by the ionic liquid that swelled in size with increasing temperature until macroscopic phase separation occurred. Aggregation behavior approaching the critical point for [P₄₄₄₄][CF₃COO] aqueous mixtures was also observed by density fluctuations from small-angle X-ray scattering (SAXS) [53]. However, the SAXS study did not support micelle formation i.e., structures consisting of an ordered hydrophilic shell and hydrophobic core [52]. The authors of the previous studies concluded that the aggregates formed non-distinct ‘fuzzy clusters’ composed of ionic liquid and water molecules [53]. What appears consistent of IL|H₂O LCST mixtures is the change from a more homogenous mixture (reduced density fluctuations, smaller aggregates) to a more inhomogeneous mixture upon heating up to the T_c and macroscopic phase separation. Thus, the microstructure of the system seems to change gradually with temperature perturbation rather than undergoing a sudden structural change at T_c . This trend is compared against the same test on a chemically similar system not exhibiting a LCST phase transition in water, tetrabutylphosphonium benzenesulfonate [P₄₄₄₄][BnzSO₃], and is shown in Fig. 2-3b. In this system, the 2, 4- methyl positions on the DMBS anion are replaced with hydrogens, yielding benzenesulfonate. Despite the minor chemical change, this system exhibits markedly different behavior. As noted by *Ohno* [33], this mixture remains fully miscible versus temperature rather than undergoing a liquid-liquid phase separation. At lower temperatures, the system reveals scattering aggregates on the order of hundreds of nanometers. The aggregate’s size rapidly reduces an order of magnitude and then more gradually shrinks to tens of nanometers upon further heating. The seemingly inert substitution of methyl groups with hydrogens results in the loss of the LCST transition and opposite aggregation behavior versus temperature as compared to the fully miscible phase of the LCST IL. One possible explanation for the distinct result is that [P₄₄₄₄][BnzSO₃] in water forms extended apolar and polar networks, which has been understood to occur in other ionic liquid mixtures [54-56]. In contrast [P₄₄₄₄][DMBS] cannot form extended networks (possibly due to steric disruption) and is relegated to distinct solvated ion pair/pair clustering in water.

Previously unexplored in LCST mixtures are changes in long range order after phase separation into an aqueous rich and ionic liquid rich phase. In the fully miscible state just below the critical point, the solution formed aggregates on the order of 9 nm. Above T_c , each of the two-phase mixture shows substantial changes in long range order. The ionic liquid rich phase shows aggregates on the order of 500 nm at 37 °C, just above T_c . The size of aggregates in the IL rich phase subsequently decrease with increasing temperature to 150 nm at 39 °C and then to 100 nm at 41 °C. The initial 50-fold increase in IL aggregate size going from the miscible phase to IL rich phase would likely arise from the sudden decrease in water concentration and additionally the reduced electrostatic screening from water enabling larger aggregates to form.

The aqueous rich phase shows nearly an order of magnitude increase scattering diameter of 3000 nm compared to the IL rich phase just above phase separation. While an increase in aggregate size matches the temperature dependent exponential particle growth trend in the miscible phase this is also a seemingly counterintuitive result; as the concentration of ionic liquid is greatly reduced in the aqueous phase. One would expect the aggregate structure to decrease in size with reduced ionic liquid and increased screening between ion pairs from higher water content.

Koga et al. [57] studied the higher order derivatives of the Gibbs energy with regard to the excess enthalpy, and found the LCST IL [P₄₄₄₄][CF₃COO] exhibited strong hydrophobic character, especially compared to other ionic liquids not exhibiting a LCST transition in water. The authors proposed that [P₄₄₄₄][CF₃COO] acting as an extreme hydrophobe may not dissociate in water rich regions. Our observation of large IL aggregates in the water rich phase supports the author's proposal, where the hydrophilic IL aggregates rather than dissociate. This decline in aggregate size upon additional heating is similar to the general trend in the fully soluble IL, [P₄₄₄₄][BnzSO₃]. Molecular dynamics of the ionic liquid, tetraalkylphosphonium-Bis(oxalato)borate, at very dilute concentrations in water found a 'loose micelle-like aggregate' structure with the cation alkyl chains forming a hydrophobic core and hydrophilic shell formed by polar segments of the anion and cation [56]. However, such a structure cannot be verified by DLS measurements in this work.

Method for Dynamic Light Scattering (DLS)

Dynamic Light Scattering experiments were carried out using an ALV-6010/200 Multiple Tau Digital Correlator with a 632 nm HeNe laser and a 1 cm cuvette containing a U-shaped channel for external liquid flow enabling temperature-controlled measurements with a water-heater chiller within 0.05 °C. The flow channel prevented 90° scattering detection, so scattered light was collected in a backscatter geometry with a collection angle of 165°. Scans were collected for 90 seconds and averaged over multiple data acquisitions. Temperature dependent viscosity of the solutions were measured with a TA Rheometer equipped with a Peltier temperature controller at a 200 rev s⁻¹ shear rate. Temperature dependent refractive index was measured with an Abbe DR-M2 refractometer at 589 and 680 nm, and extrapolated to 632 nm.

2.2.3 Molecular Dynamics simulation setup

All-atom AMBER force fields for potential energy U were used in the MD simulation of this system.

$$\begin{aligned}
 U_{potential} = & \sum_{i>j} \left[4\epsilon_{ij} \left\{ \left(\frac{\sigma_{ij}}{r_{ij}} \right)^{12} - \left(\frac{\sigma_{ij}}{r_{ij}} \right)^6 \right\} + \frac{q_i q_j}{4\pi\epsilon_0 \epsilon_r r_{ij}} \right] + \sum_{bonds=water\ OH} D_r [1 - e^{-\beta(r-r_0)}]^2 \\
 & + \sum_{bonds \neq water\ OH} K_r (r - r_0)^2 + \sum_{angles} K_\theta (\theta - \theta_0)^2 + \sum_{torsions} \frac{K_\phi}{2} \{1 + \cos(n\phi - \gamma)\}
 \end{aligned} \quad (2.5)$$

The first term describes the non-bonded interactions including Van der Waals as the Lennard-Jones 12-6 form and Coulombic forces from atom-centered partial charges. The following terms in the potential energy equation represent, respectively, bonds, angles and torsional interactions. A hybrid bond potential was applied: the Morse potential for the OH bond in water and a harmonic potential for others. The force field parameters of atomistic [P₄₄₄₄] cation and [DMBS] anion were developed in previous works [58,59] and are summarized in Tables 2-1 to 2-5. A flexible water model [60] based on a four-site water model of TIP4P/2005 is employed for water molecules, which depicts well the dynamics and bulk properties of the condensed water. In particular, the flexibility of the OH bond distance and HOH angle enables observation of the structural behavior which provides this information about directional bonding, e.g. hydrogen bonding. The VdW interaction parameters between unlike atoms are obtained by the Lorentz–Berthelot combining rule. The non-bonded interactions separated by exactly three consecutive bonds (1–4 interactions) are reduced by related scaling factors [61,62], which were optimized as 0.50 for VdW interactions and 0.83 for electrostatic interactions, respectively. Atomic charges are calculated using a web base calculator, AtomicChargeCalculator, via the Electronegativity Equalization Method (EEM) [63]. The schematic molecular structures and partial charges of the [P₄₄₄₄] cation and [DMBS] anion and water molecule of the flexible TIP4P/2005 water model are presented in Fig. 2-4.

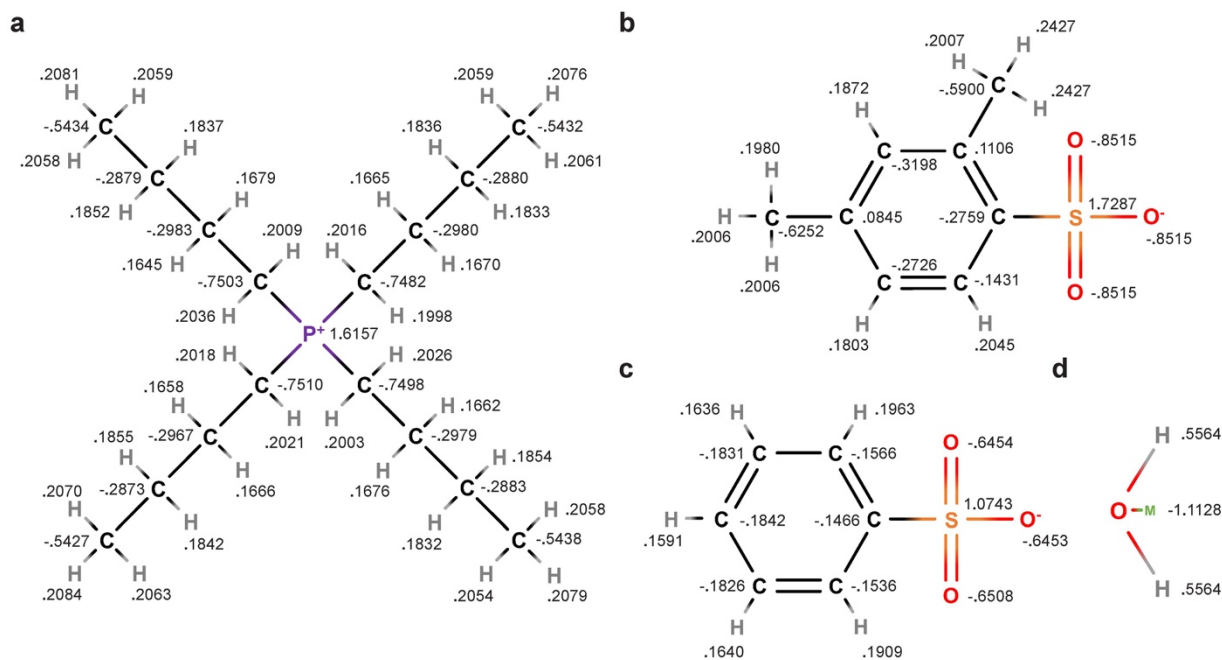


Figure 2-4. Molecular structures and partial atomic charges of (a) the [P₄₄₄₄] cation, (b) the [DMBS] anion (c) the [BnzSO₃] anion and (d) the four-site based water molecule. The mostly charged atom represents the position of each molecules. i.e. the P atoms, S atoms, S atoms and O atoms, respectively, are taken as reference sites of the [P₄₄₄₄] cation, the [DMBS] anion the [BnzSO₃] anion and water molecule for further analysis.

The MD simulation is performed using the LAMMPS package with standard three-dimensional periodic boundary conditions. The non-bonded interactions were cut off at 15 Å while the Ewald summation method is applied to treat the long-range electrostatic interactions. All simulations are carried out at isothermal-isobaric conditions in the Nose-Hoover NPT ensemble with time coupling constants of 25 and 250 fs, respectively. After an initial relaxation with short time steps and an equilibration with long time steps, additional simulations of 3 sets of 4 ns of the ensemble at each temperature are further performed with a fixed time step of 0.25 fs. The simulation time of 4 ns was preliminary tested to check that the time duration is long enough to collect ensembles and independent of the system size. The atomic trajectories of simulation are recorded with an interval of 1 ps for post-analysis.

For the investigation of IL|H₂O mixture with LCST behavior, the 80 pairs of [P₄₄₄₄][DMBS] and 1920 water molecules are initially displayed without an overlap, corresponding 50.8 wt.% of ILs in IL|H₂O mixtures. The number of molecules is chosen to satisfy that the system size enough exceeds twice the cut off distance for the non-bonded interactions. A total of four different

temperature cases are performed at atmospheric condition: Two cases of below T_c (10, 20 °C) and two cases of above T_c (50, 60 °C). Temperature conditions far from the measured T_c are selected because the temperature of the liquid states in MD simulation fluctuates by 10 °C up and down.

Additional MD simulation set of [P₄₄₄₄][BnzSO₃] is employed to investigate the IL|H₂O mixtures without LCST behavior. The 80 pairs of [P₄₄₄₄][BnzSO₃] and 1440 water molecules are initially displayed without an overlap, corresponding 49.6 wt.% of ILs in IL|H₂O mixtures. Two different temperature cases are performed at atmospheric condition, 20 and 50 °C.

Table 2-1. Van der Waals parameters for the force field in molecular dynamics simulations.

molecule	atoms	σ (Å)	ϵ (kJ/mol)	description
Water	Ow	3.1644	0.6498	Oxygen in water
	Hw	0	0	Hydrogen in water
P ₄₄₄₄	P	3.7418	0.8368	Phosphorus
	C	3.3997	0.3598	sp ³ carbon
	HP	1.9600	0.0657	H attached to carbon bonded to formally positive atom
	HC	2.6495	0.0657	H attached to carbon with no electron-withdrawing substituents
DMBS & BnzSO ₃	CA	3.3997	0.3598	aromatic sp ² carbon
	C	3.3997	0.3598	sp ³ carbon
	HA	2.5996	0.0628	H attached to aromatic carbon
	HC	2.6495	0.0657	H attached to sp ³ carbon
	S	3.5636	1.0460	Sulfur
	O	2.9599	0.8786	Oxygen in Sulfite

Table 2-2. Bond parameters of the flexible water model [60] for Morse potential force field in molecular dynamics simulations.

molecule	bonds	r_0 (Å)	D_r (kJ/mol)	β (1/Å)
Water	O-H	0.9419	432.581	2.287

Table 2-3. Bond parameters for the harmonic potential force field in molecular dynamics simulations.

Ion	bonds	r_0 (Å)	K_r (kJ/mol Å ²)	source
P ₄₄₄₄	P-C	1.8273	878.64	[58]
	C-C	1.5334	1297.04	AMBER
	C-HP	1.0862	1407.92	[58]
	C-HC	1.0860	1384.90	[58]
DMBS & BnzSO ₃	CA-CA	1.3903	1673.60	[58]
	CA-C	1.49	962.32	[59]
	CA-HA	1.0765	1502.06	[58]
	CA-S	1.78	962.32	[59]
	C-HC	1.0860	1384.90	[58]
	S-O	1.4577	2217.52	[58]

Table 2-4. Angle parameters for the harmonic potential force field in molecular dynamics simulations.

molecule	angles	θ_0 (deg)	K_θ (kJ/mol rad ²)	source
Water	H-O-H	107.40	367.81	[60]
P ₄₄₄₄	C-C-C	111.88	171.54	[58]
	C-C-HP	110.07	129.70	[58]
	C-C-HC	109.96	177.82	[58]
	C-P-C	109.46	209.20	[58]
	HP-C-HP	107.36	153.55	[58]
	HC-C-HC	106.47	160.25	[58]
	P-C-C	116.24	313.80	[58]
	P-C-HP	106.74	135.98	[58]
DMBS & BnzSO ₃	CA-CA-CA	120.00	263.59	AMBER
	CA-CA-C	122.30	191.63	[59]
	CA-CA-HA	119.80	158.99	[58]
	CA-CA-S	122.30	41.84	[59]

CA-C-HC	107.50	206.27	[59]
CA-S-O	98.00	355.64	[59]
HC-C-HC	108.50	160.25	[58]
O-S-O	113.83	418.40	[58]

Table 2-5. Dihedral parameters for the force field in molecular dynamics simulations.

molecule	angles	γ (deg)	$K\phi$ (kJ/mol)	n	source
P ₄₄₄₄	C-C-C-C	0	0.753	3	AMBER
	C-C-C-HP	0	0.669	3	[58]
	C-C-C-HC	0	0.669	3	AMBER
	C-C-C-P	0	0.603	3	[58]
	C-C-P-C	0	0.690	3	[58]
	C-P-C-HP	0	0.690	3	[58]
	HP-C-C-HC	0	0.628	3	[58]
	HC-C-C-HC	0	0.628	3	AMBER
	HC-C-C-P	0	0.603	3	[58]
DMBS & BnzSO ₃	CA-CA-CA-CA	180	15.167	2	AMBER
	CA-CA-CA-C	180	12.970	2	[59]
	CA-CA-CA-HA	180	15.167	2	AMBER
	CA-CA-CA-S	180	12.970	2	[59]
	CA-CA-C-HC	0	0	6	[59]
	CA-CA-S-O	0	16.736	2	[59]
	C-CA-CA-HA	180	17.573	2	[59]
	C-CA-CA-S	180	15.167	2	AMBER
	HA-CA-CA-HA	180	15.167	2	AMBER
HA-CA-CA-S	180	17.573	2	[59]	

2.2.4 Molecular Dynamics simulation results

The MD simulations are employed to investigate the aggregation trends in the IL|H₂O mixtures in response to the temperature for the both [P₄₄₄₄][DMBS] and [P₄₄₄₄][BnzSO₃] systems. The radial distribution function (RDF), $g(r)$, is a calculated parameter which quantifies the spatial correlation between specific atoms, and thus enables detailed understanding of structural features of microscopic ionic liquid systems. The $g(r)$ is defined as the ratio of the local time-averaged number density of specific particles at a given distance, r , from an origin particle to the total average number density of the particles, so then expressed as

$$g(r) = \frac{dn(r)}{\rho_n 4\pi r^2 dr} \quad (2.6)$$

where ρ_n is the total number density of the particles. The mostly charged atom in Fig. 2-4 represents the position of each molecules for the RDF analysis. i.e. the P atoms, S atoms, S atoms and O atoms, respectively, are taken as reference sites of the [P₄₄₄₄] cation, the [DMBS] anion the [BnzSO₃] anion and water molecule.

Figure 2-5 shows the calculated RDF results for [P₄₄₄₄][DMBS]. According to the cation-anion RDF (Fig. 2-5a), the ion pairs are attracted strongly to each other by means of strong electrostatic interactions. The pronounced peak observed at around 5 Å results from the geometry of the ions. The two simulations for temperatures above T_c display a greater peak height as compared to the that of the lower temperature cases. It is basically counter-intuitive for the more thermal motion of molecules at the higher temperature. This indicates that at higher temperatures ion pairs reside in closer proximity to each other. However, inspection of the two cases in the below T_c range show a remarkable lack of difference. Thus, the apparent temperature dependence of the cation-anion $g(r)$ suggests that the electrostatic interaction is a main driving force responsible for the aggregation in the ionic liquids. As no strong attractive potential exists among ions of the same charge, the cation-cation and anion-anion RDFs must be a consequence of the electrostatic interactions between oppositely charged ions. The cation-cation RDF (Fig. 2-5b) shows evidence of clustering at above T_c range. Considering the size of the single cation with even butyl chains of around 6 Å, the multiple small peaks between 5 and 10 Å are observed and can be interpreted as all located in the first coordination shell. The many numbers of peaks come from different coordination orientations and mean the ions are loosely tied. The merging of neighboring small peaks at elevated temperature causes a major peak at 7 Å at the two cases above T_c . The peak distance corresponds the summation of the length of a butyl chain in [P₄₄₄₄] and the O-S bond length of sulfonate in [DMBS]. Therefore, the major peak means the ions are compactly tied to each other by the strong electrostatic forces and the ion-pair aggregation is in the dense form of multiple layers of cation-anion shells. The first small peak moving to the larger radius as a

temperature change from 10 °C to 20 °C is also consistent with the experimental results (Fig. 2-3a) at below T_c range. Nevertheless, since the MD simulations were carried out with 80 pairs of ions equilibrated in a simulation box with box lengths less than 10 nm in all dimensions, some experimental results, such as the aggregation on length scales of several thousands of nm, are difficult to be realized in the typical size scale of an MD simulation. For the anion-anion RDF of Fig. 2-5c, since the [DMBS] anion is a relatively small and flat molecule which can be located between cations and the aggregation is mainly caused by cation-anion interactions, no clear conclusion can be reached from this. However, the aforementioned trend depending on temperature is not observed at the [P₄₄₄₄][BnzSO₃]|H₂O mixture without the LCST behavior, as shown in Figs. 2-6a to 2-6c. The cation-anion RDF of the 50 wt.% of [P₄₄₄₄][BnzSO₃]|H₂O mixture system shows the opposite trend of a smaller peak height with increasing temperature, which is also consistent with the experimental results of Fig. 2-3b. Other RDFs in Fig. 2-6 display a notable lack of temperature dependence.

Figures 2-5d to 2-5f present RDFs with water molecules and supports the experimental findings of the LCST characteristic. The overall $g(r)$ of all RDFs with water molecules of the two cases above T_c is lower than that of the two below T_c cases, which means there are fewer spaces between ions. The trend is more clearly observed in the ion-water RDFs, and demonstrates the ion-water interactions declines as temperature increases. Hydrogen bonding exists in this IL|H₂O mixture system. The gain or loss of the directional bonding has been used as the most reliable approach to explain the LCST behavior of small molecules [64].

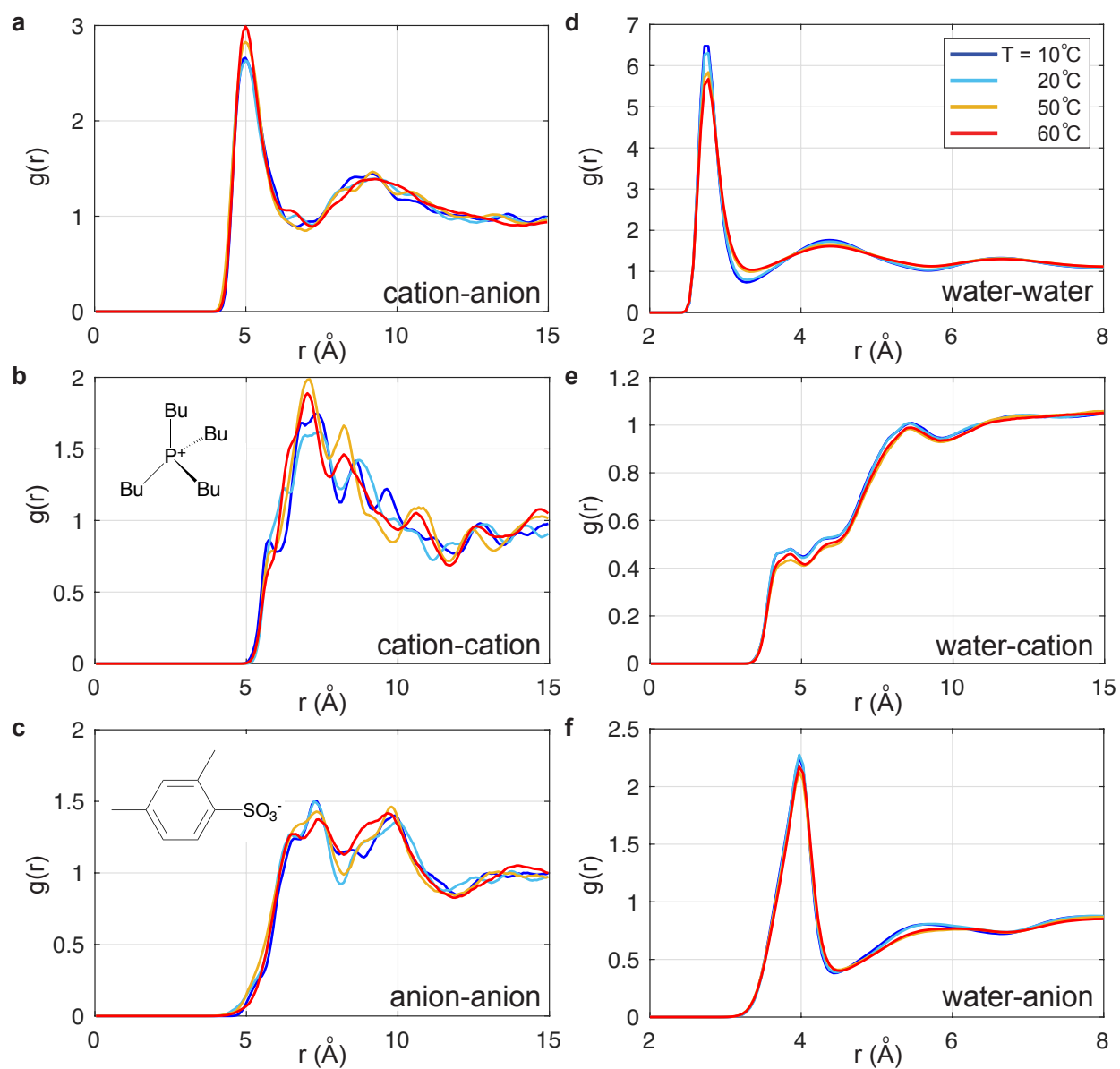


Figure 2-5. RDFs from MD simulations for the 50 wt.% [P₄₄₄₄][DMBS]H₂O system. (a) cation-anion (b) cation-cation (c) anion-anion (d) water-water (e) water-cation and (f) water-anion pairs.

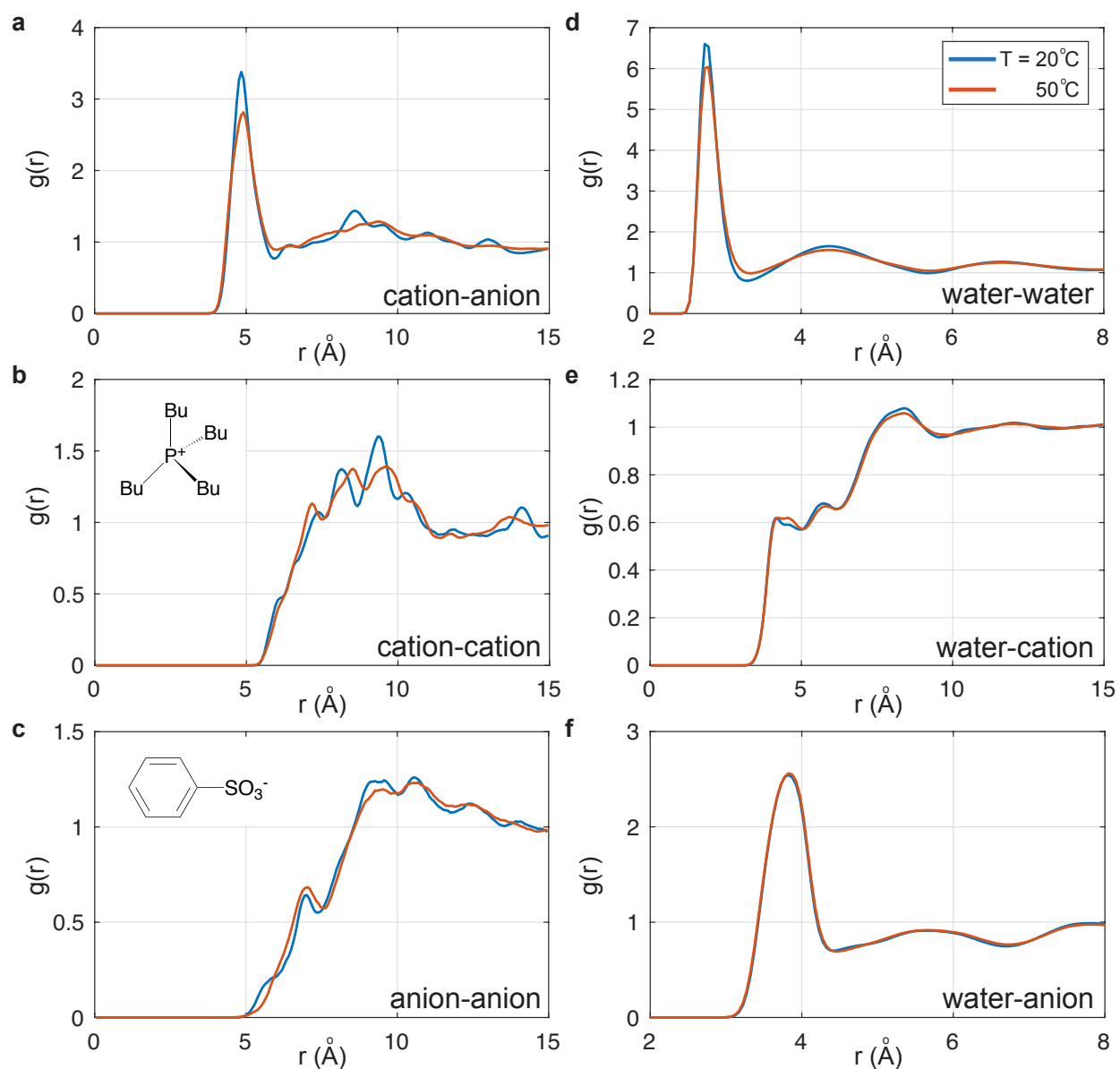


Figure 2-6. Radial distribution functions (RDFs) calculated from MD simulations for the 49.6 wt.% [P₄₄₄₄][BnzSO₃] IL/H₂O system in different temperature conditions: (a) cation-anion, (b) cation-cation, (c) anion-anion, (d) water-water (e) water-cation and (f) water-anion pairs.

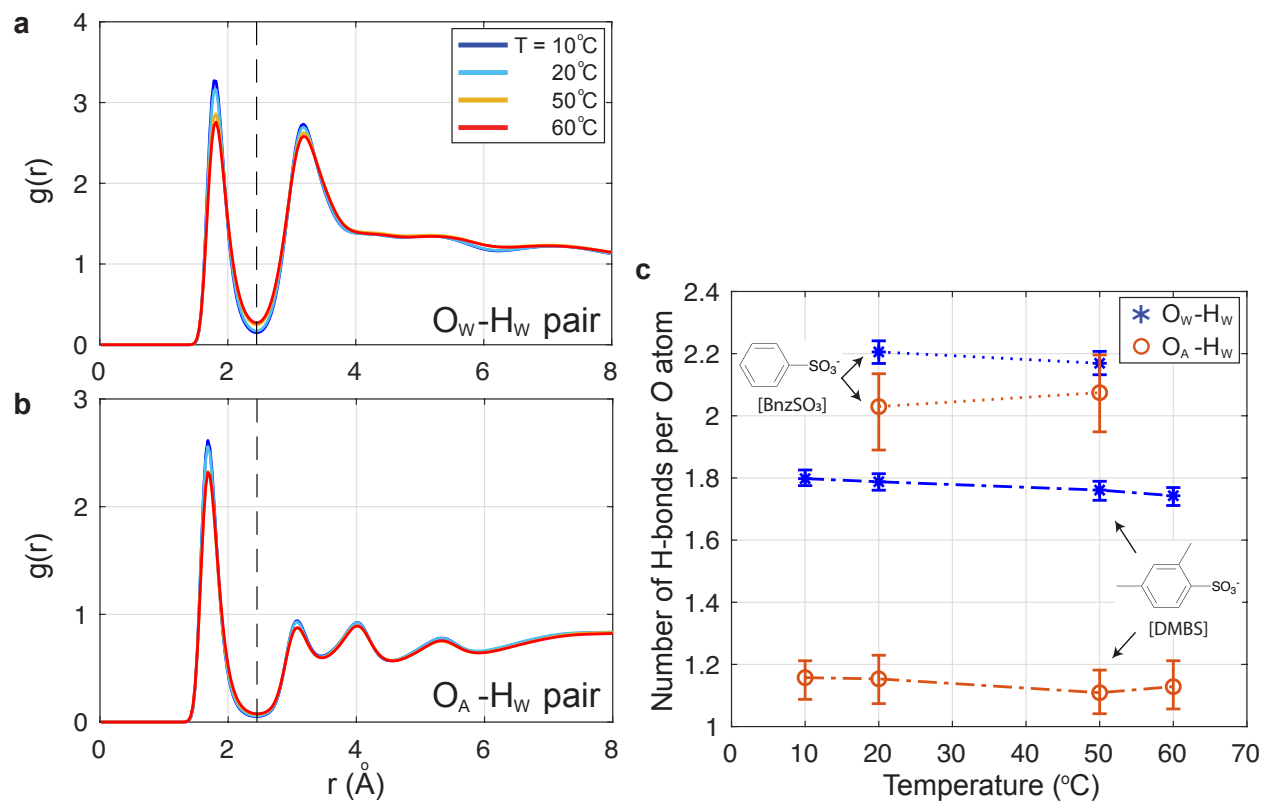


Figure 2-7. Calculated the number of hydrogen bonds for the 50 wt.% IL|H₂O system. (a-b) RDFs between oxygen and hydrogen for the 50.8 wt.% [P₄₄₄₄][DMBS] IL|H₂O system. (a) Oxygen of sulfite in anion-Hydrogen in water, (b) Oxygen in water-Hydrogen in water pairs. Vertical dashed lines denote O-H separation to define hydrogen bonding. (c) Number of hydrogen bonds as a function of temperature per each oxygen atom for both 50 wt.% of [P₄₄₄₄][DMBS] and [P₄₄₄₄][BnzSO₃] with water solution. Error bars present the range of recorded data from MD per 1 ps.

In order to gain insight into hydrogen bonding in the IL|H₂O mixtures, representative oxygen and hydrogen pair distributions in the [P₄₄₄₄][DMBS] mixture system are presented in Fig. 2-7. The O-H separation based on the RDFs clearly suggests a simple definition of the hydrogen bonding, as the radius of the first hydrogen atom coordination shell for each oxygen atom, without any further complicated definition. Each occurrence of an O-H approach within 2.45 Å for both pairs in Fig. 2-7 can be determined as the hydrogen bonding. Applying the definition of O-H separation distance, the number of hydrogen bonds per each oxygen atom in each temperature case was counted and summarized in Fig. 2-7c. For the [P₄₄₄₄][DMBS] mixture system with the LCST behavior, the degree of hydrogen bonding seems to decrease with increasing temperature. It is known that solutions of 50 wt.% or more contain essentially no free water [64]. In other words, all

water molecules either participate in hydrogen bonding or the formation of hydration shells around the ILs. A lesser degree of hydrogen bonding at the above T_c means more water molecules contribute to the hydration shell of ILs. However, for the $[P_{4444}][\text{BnzSO}_3]$ mixture system, each oxygen atom is basically involved in more hydrogen bonds compared to the ILs with LCST behavior. As a result, the shortage of water contributing to stable hydration interactions disturbs the mechanism leading to the large IL clusters. The number of hydrogen bonds per oxygen atom in $[\text{BnzSO}_3]$ anion increases as a function of temperature. The net number of hydrogen bonds ($O_w\text{-H}_w$ & $O_A\text{-H}_w$) for the mixture display a notable lack of temperature dependence a wide temperature range. Although an additional analysis of angle distribution of water molecules to verify the contribution of dipoles relative to the ions, the dependency of average angle on the temperature is not observed as shown in Fig. 2-8.

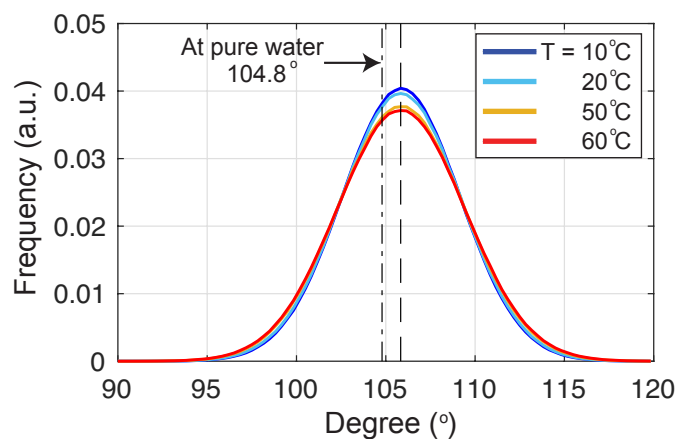


Figure 2-8. The HOH angle distribution of water molecules in the 50.8 wt.% $[P_{4444}][\text{DMBS}]$ IL/ H_2O system calculated from MD simulations with a flexible water model based on a four-site water model of TIP4P/2005. In spite of the analysis to verify the contribution of dipoles relative to the ions, the dependency of average HOH angle on the temperature is not observed.

2.3 Osmotic strength of LCST ILs

Experiments in this part were conducted by Dr. Akanksha K. Menon and Dr. Andrew Z. Haddad

2.3.1 Problem statement

For the proposed FO desalination system depicted in Fig. 2-2, the cation and anion combination for the LCST behavior as a draw solution is one of the most critical parameters. Various thermo-responsive ILs have been identified in literature for different applications, but the

following solution properties are of interest for the FO desalination with a low-grade heat source: (i) LCST phase transition, (ii) viscosity and (iii) osmotic strength. The temperature-dependent phase behavior of the IL-water mixtures affects the draw regeneration step, and the osmotic strength and viscosity of aqueous IL solutions are significant parameters that impact water flux during the FO dilution step. With multiple properties to be optimized and many potential IL chemistries, the analytical hierarchy process [65] methodology is used to select the most suitable ILs. Specifically, we focused on ILs with $[P_{4444}]$ as the cation because its amphiphilicity results in LCST behavior with a variety of anions. In addition to $[DMBS]$ anion, which was studied at the previous part, trifluoroacetate $[TFA]$ is also selected as an ideal candidate for the counterpart of $[P_{4444}]$.

A binary phase diagram is constructed to determine the LCST of each IL by measuring the optical transmittance as a function of temperature; for a given concentration, phase separation is evidenced by a sharp decrease in transmittance that is recorded as the critical temperature (Fig. 2-9). As shown in Fig. 2-10, $[P_{4444}][DMBS]$ displays a broad binodal phase curve, with an LCST of 36 °C at a concentration of 40 wt.%, while the $[P_{4444}][TFA]$ curve is symmetric with an LCST of 31 °C at the same concentration. The width of the curve dictates the effectiveness of phase separation upon heating - the broad curve for DMBS indicates that at a temperature of say 55 °C, the 40 wt.% mixture separates into a concentrated IL-rich phase >80 wt.%, while TFA at the same concentration and temperature separates into an IL-rich phase of ~70 wt.% (confirmed by NMR analysis). Thus, the draw solutions should be heated not just to their LCST, but to temperatures ~20 °C higher in order to be regenerated and reused in a subsequent FO process, while the product water contains <10 wt.% of IL.

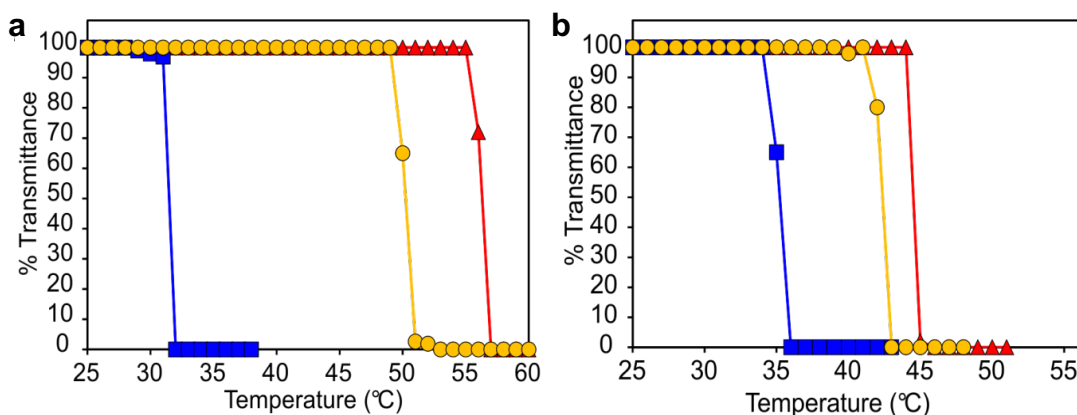


Figure 2-9. UV-Vis transmittance measurements used to determine cloud points as a function of IL-water concentration for LCST determination of (a) $[P_{4444}][DMBS]$ and (b) $[P_{4444}][TFA]$. Concentrations of 70 wt.% (in red), 40 wt.% (in blue) and 10 wt.% (in yellow) are shown.

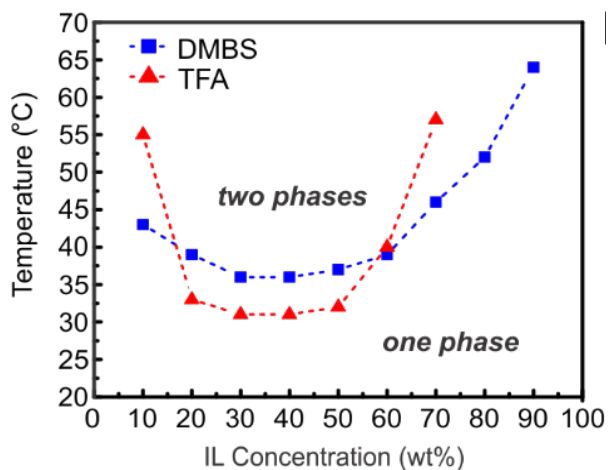


Figure 2-10. Binodal phase diagram of aqueous mixtures of $[P_{4444}][DMBS]$ and $[P_{4444}][TFA]$ which show the LCST behavior.

The viscosity of $[DMBS]$ and $[TFA]$ solutions is measured at 25 °C as shown in Fig. 2-10. Viscous draws can cause concentration polarization that adversely impacts water flux [66]. At concentrations <30 wt.% the mixture viscosity is close to that of water (~ 1 mPa-s) but then increases with concentration, likely due to molecular interactions (*e.g.* ion pairing and/or molecular aggregation) at these non-dilute concentrations which are studied at the previous part.

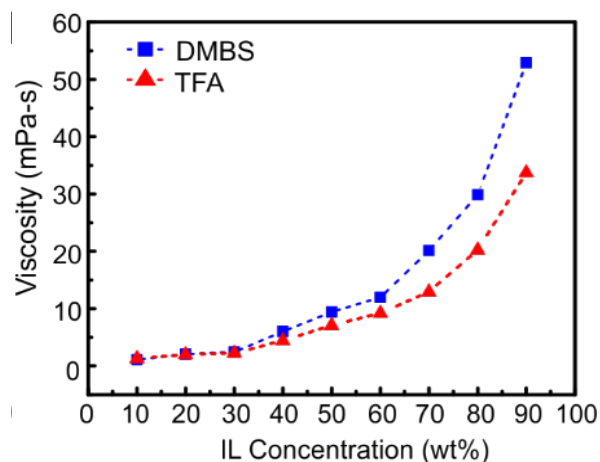


Figure 2-11. Viscosity of aqueous mixtures of $[P_{4444}][DMBS]$ and $[P_{4444}][TFA]$ as a function of concentration.

In this part, we study the osmotic strength of the aqueous mixtures which is the most important characteristics for the FO desalination. The osmotic pressure is experimentally measured

as a function of concentrations in water to evaluate the ability of ILs as draw solutes to desalinate feeds of varying salinity. Then, the theoretical osmolality at the aggregated molecular structures is investigated by using the MD simulation.

2.3.2 Experimental observation

The osmotic strength of aqueous mixtures of $[P_{4444}][DMBS]$ and $[P_{4444}][TFA]$ is measured at 25 °C at which FO draw dilution occurs. It is in contrast with literature measurements based on freezing point techniques that over-predict osmotic strength as the physical state of the mixture and thermal interactions are altered at low temperatures [67]. Figure 2-12a shows the osmolality of both selected ILs, which provides a measure of ions dissolved in solution at a given concentration, and this is converted into an approximate osmotic pressure. The osmotic pressure of both ILs can be tuned by changing the mixture concentration, rendering them suitable for salinities ranging from brackish water to produced water. At low concentrations <10 wt.%, the osmolality of both $[DMBS]$ and $[TFA]$ increase linearly, indicating complete dissociation into constituent ions as expected in a dilute mixture. However, at intermediate concentrations ~20-50 wt.%, both ILs appear to have a near-constant osmolality, which increases dramatically upon further increase in concentration >60 wt.%. To understand this unusual behavior, osmolality is plotted as a function of mixture molality and compared with an ideal solute like NaCl. As shown in Fig. 2-12b, above ~0.3 mol kg⁻¹, the osmotic pressure generated by IL ions in solution deviates significantly from NaCl dissolved in water.

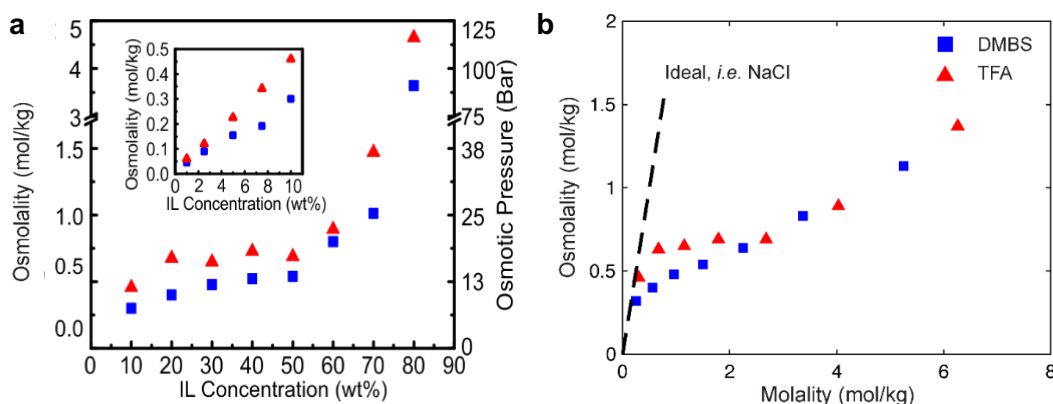


Figure 2-12. Osmotic strength of $[P_{4444}][DMBS]$ and $[P_{4444}][TFA]$ (a) Measured osmolality and calculated osmotic pressure, with dilute mixtures shown in the inset. (b) Osmolality measured as a function of molality showing deviations from ideal mixtures.

2.3.3 Molecular Dynamics simulation setup

To provide insight on the deviation from the ideal solute, MD simulations are performed. All-atom AMBER force fields for potential energy, U were used in the MD simulation of this system.

$$\begin{aligned}
 U_{potential} = & \sum_{i>j} \left[4\epsilon_{ij} \left\{ \left(\frac{\sigma_{ij}}{r_{ij}} \right)^{12} - \left(\frac{\sigma_{ij}}{r_{ij}} \right)^6 \right\} + \frac{q_i q_j}{4\pi\epsilon_0\epsilon_r r_{ij}} \right] + \sum_{bonds} K_r (r - r_0)^2 + \sum_{angles} K_\theta (\theta - \theta_0)^2 \\
 & + \sum_{torsions} \frac{K_\phi}{2} \{1 + \cos(n\phi - \gamma)\}
 \end{aligned} \tag{2.7}$$

Since the dependency of average angle was not observed at the previous part (Fig. 2-8), The rigid TIP4P water model [68] was employed for water molecules, which depicts enough well the dynamic and structural properties of liquid water. The same force field parameters of atomistic [P4444] cation, [DMBS] anion with the previous part are used. The force field parameters of [TFA] anion were developed in the previous work [69] and the newly added molecules' parameters are summarized in Tables 2-6 to 2-9. The schematic molecular structures and partial charges of the [P4444] cation, [DMBS] anion, [TFA] anion and water molecule of the rigid TIP4P water model are presented in Fig. 2-13.

The number of initially displayed ion pairs and water molecules to match the concentration cases is summarized in Table 2-10. The non-bonded interactions were cut off at 15 Å while the particle-particle particle-mesh solver [70] is applied to treat the long-range electrostatic interactions. All simulations are carried out at isothermal-isobaric conditions, at 25 °C and ambient pressure, in the Nose-Hoover NPT ensemble with time coupling constants of 100 and 1000 fs, respectively. After initial relaxations with short time steps and an equilibration with long time steps, at least 6 ns simulation of the ensemble were performed with a fixed time step of 1.0 fs. The atomic trajectories of simulation or the RDFs were recorded with an interval of 1.5 ps for post-analysis. Unmentioned conditions are identically set up with the previous part.

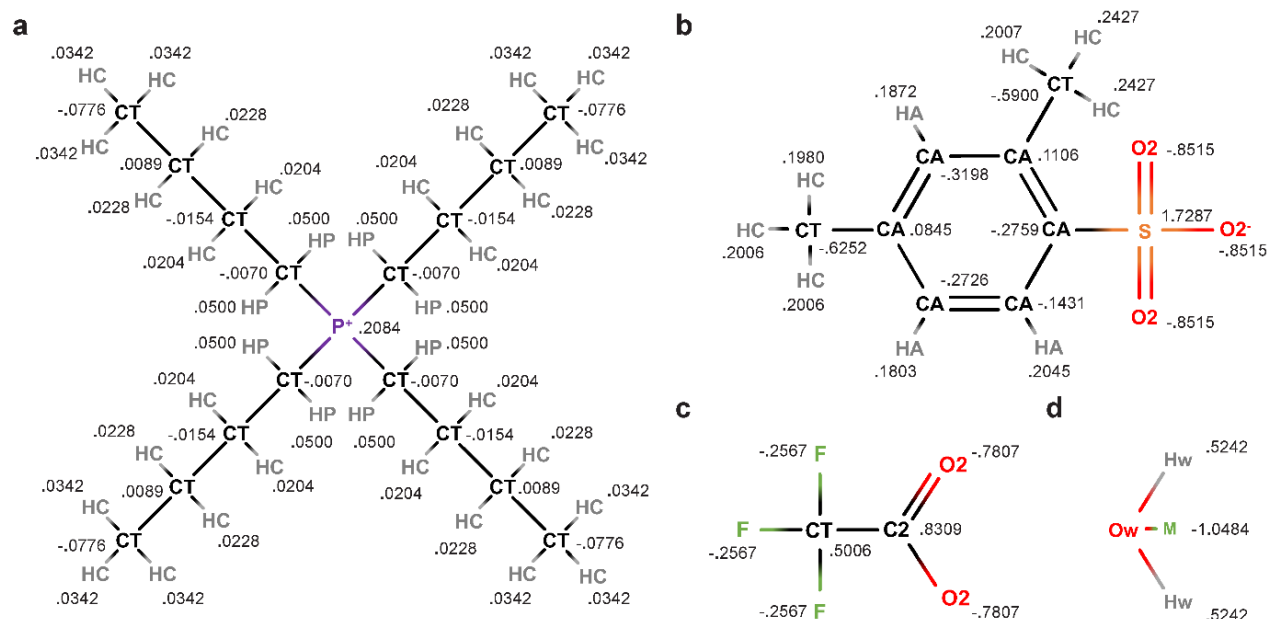


Figure 2-13. Molecular structures and partial atomic charges of the (a) P₄₄₄₄ cation, (b) DMBS anion, (c) TFA anion and (d) the rigid TIP4P water model.

Table 2-6. Van der Waals parameters for the force field in molecular dynamics simulations.

molecule	atoms	σ (Å)	ϵ (kJ/mol)	description
TFA	CT	3.3997	0.4577	sp ³ carbon
	C2	3.3997	0.3598	sp ² carbon
	F	3.1180	0.2552	Fluorine
	O2	2.9599	0.8786	sp ² oxygen

Table 2-7. Bond parameters for the harmonic potential force field in molecular dynamics simulations.

Ion	bonds	r_0 (Å)	K_r (kJ/mol Å ²)	source
TFA	C2-CT	1.5680	1087.84	[69]
	C2-O2	1.2230	2322.12	[69]
	CT-F	1.3340	1004.16	[69]

Table 2-8. Angle parameters for the harmonic potential force field in molecular dynamics simulations.

molecule	angles	θ_0 (deg)	K_θ (kJ/mol rad ²)	source
TFA	CT-C2-O2	113.60	167.36	[69]
	O2-C2-O2	132.80	439.32	[69]
	C2-CT-F	112.80	376.56	[69]
	F-CT-F	106.00	585.76	[69]

Table 2-9. Dihedral parameters for the force field in molecular dynamics simulations.

molecule	angles	γ (deg)	K_ϕ (kJ/mol)	n	source
TFA	F-CT-C2-O2	0	0.209	3	[69]

Table 2-10. The number of ion pairs of the [P₄₄₄₄][DMBS] and [P₄₄₄₄][TFA], and water molecules in the MD studies in order to match with the mass fraction conditions at the experiments.

Ion pairs	wt.%	N_{IL}	N_{water}
[P ₄₄₄₄] & [DMBS]	10.0	24	5352
	29.9	48	2784
	49.8	48	1200
	69.3	48	528
	80.5	48	288
[P ₄₄₄₄] & [TFA]	10.0	24	4464
	30.1	48	2304
	49.6	48	1008
	69.7	48	432
	80.5	48	240

2.3.4 Molecular Dynamics simulation results

At the previous part, I verified the hydration effect is a pre-requisite for LCST behavior. Thus, the MD simulation to understand osmotic strength of the IL|H₂O LCST mixtures is performed with interest on the number of water molecules in the first hydration shell. The first peak of the RDF between atoms in the IL and water provides information on atoms that constitute hydration shells and their radius – the central P atom in the [P₄₄₄₄] cation, S atom and benzene ring in the [DMBS] anion, and the C2 atom in the [TFA] anion are pivots for hydration shells (Figs. 2-14 and 2-15).

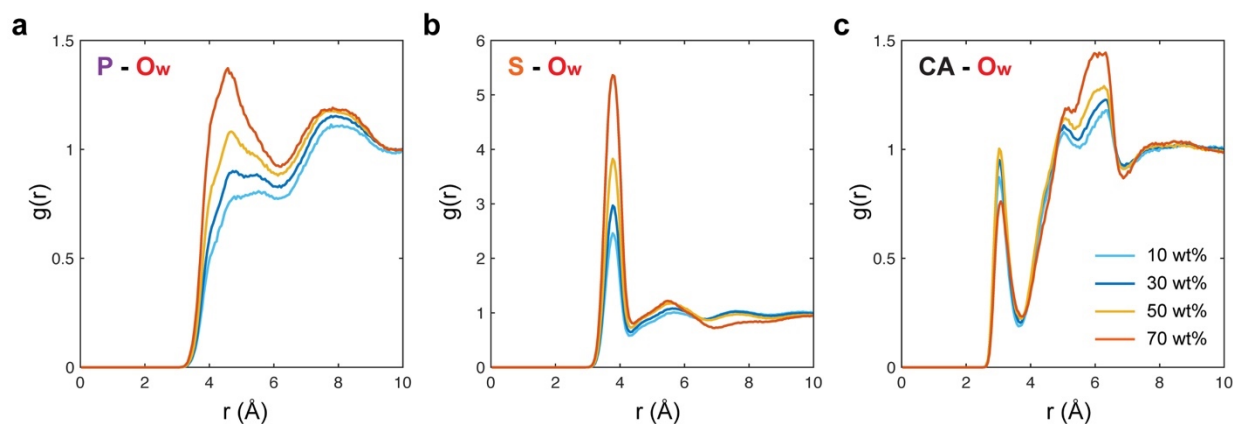


Figure 2-14. Radial distribution functions (RDFs) calculated from MD simulations of solutions of P₄₄₄₄DMBS at different concentrations between a water molecule and (a) the P atom in the P₄₄₄₄ cation, (b) the S atom in the DMBS anion, (c) center of the benzene ring in the DMBS anion.

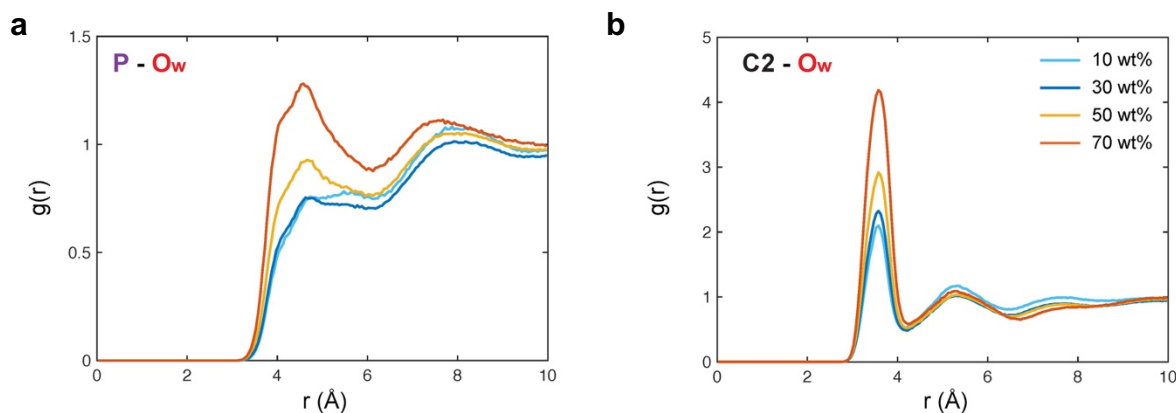


Figure 2-15. Radial distribution functions (RDFs) calculated from MD simulations for solutions of P₄₄₄₄TFA at different concentrations between water molecules and (a) the P atom in the P₄₄₄₄ cation, (b) the C2 atom in the TFA anion.

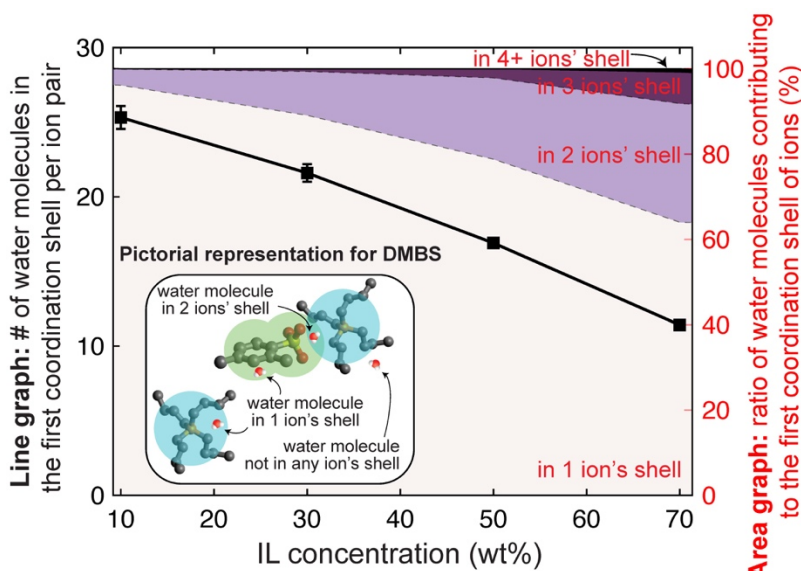


Figure 2-16. Molecular dynamics simulation showing the number of water molecules in the first coordination shell per ion pair of $[P_{4444}][DMBS]$ (line graph) and the ratio of water molecules contributing to their shells (area graph).

The inset in Fig. 2-16 provides a pictorial representation of the distribution of water molecules (i) exclusively within the coordination shell of a single ion, (ii) shared between multiple ions, or (iii) outside the first coordination shell of all ions. As the IL concentration increases, the number of water molecules inside the first coordination shell per ion pair decreases, (the line graph in Fig. 2-16 for DMBS). Furthermore, the ratio of the water molecules involved in multiple ions' the first coordination shell increases at the higher IL concentration (the area graph in Fig. 2-16 for DMBS). In other words, it appears that not all ions are hydrated due to an insufficient number of water molecules at these high IL concentrations, resulting in ion aggregation with water molecules being shared by multiple ions.

Using MD simulations, the following hypothesis is tested: to contribute to osmotic strength, a certain number of water molecules are required for a given concentration to dissociate the IL into constituent ions (*i.e.*, one cation and one anion per IL molecule). Preliminary simulations with a single-ion in water solution are firstly conducted to investigate the number of water molecules to define free ions. Similar to the general cases, the radial distribution functions between the pivot atoms and water molecules are calculated to obtain information on the first coordination shell. As shown in Fig. 2-17a, the single-ion simulations show a similar RDF trend as well as radius of the first coordination shell. Then, I count the number of water molecules in their first coordination shell which can be regarded as a hydration shell at every sampling time step (Fig. 2-17b). By choosing a criteria number of 85%, which defines the minimum number of

water molecules required to designate an ion as free, I suggest that the $[P_{4444}]$ cation needs at least 17 water molecules in its hydration shell and the $[DMBS]$ anion requires 7 and 2 water molecules in the first coordination shell from the S-atom and the center of benzene ring, respectively. For the $[TFA]$ anion, 6 or more water molecules are necessary to be solvated.

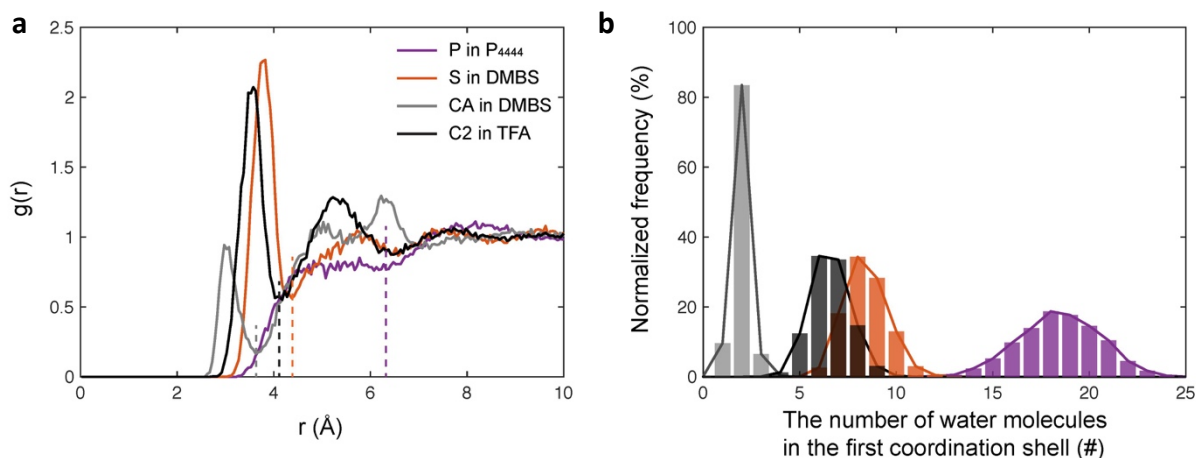


Figure 2-17. Preliminary single ion MD simulations (a) Radial distribution functions (RDFs) between a water molecule and the pivot atoms for hydration shells. Dotted lines denote the radius of the first coordination shell. (b) Normalized histogram of the number of water molecules in their first coordination shell.

Given that water molecules are being shared by multiple ions at some concentrations, two definitions of free ion are further evaluated: shared water molecules solvate all ions, or only solvate the nearest ion. When I apply the two definitions into the IL|H₂O mixtures and compare them, the simulation results for both ionic liquids indicate that the latter definition dominates, *i.e.*, shared water molecules contribute only to the nearest ion, as this correlates well with experimental data, as shown in Fig. 2-18a for DMBS. The apparent free ion ratio is defined as the ratio of measured osmolality to that predicted by van't Hoff theory for an ideal solute that dissociates into two ions (*i.e.*, like NaCl) in solution. These results indicate that a number of IL ions in solution are clustered, with shared hydration shells solvating only the nearest ion that hinders other ions from contributing to osmotic strength. At all concentrations, TFA has a larger free ion ratio than DMBS as shown in Fig. 2-18b, resulting in a higher osmolality.

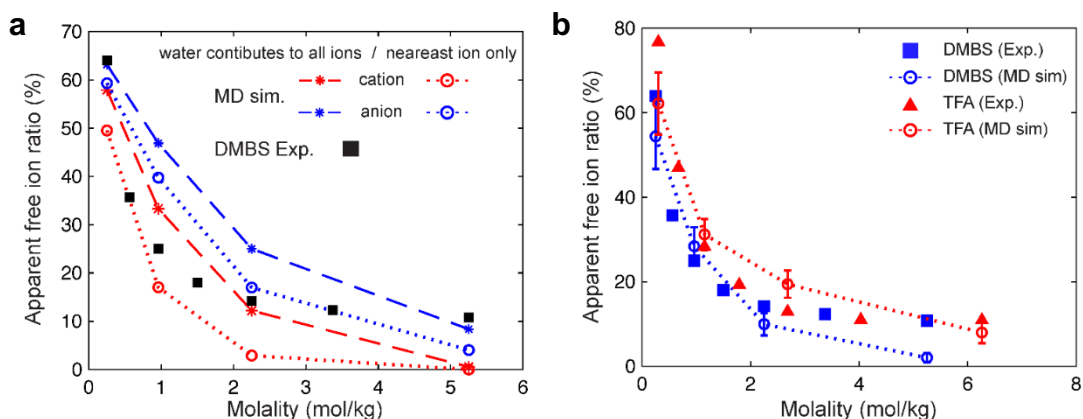


Figure 2-18. Apparent free ion ratio by two hypothetical definition of free ion. (a) Molecular dynamics simulation showing the apparent free cation and anion ratio for DMBS compared to experimental data under two assumptions. (b) Molecular dynamics simulation showing the apparent free ion ratio for DMBS (in blue) and TFA (in red) compared to experimental data under the hypothesis that water molecules contribute to the osmotic strength of the nearest ion only.

The osmolality data and MD simulations reveal for the first time, the existence of a critical concentration that is unique to each IL. This is further supported by electrical conductivity values of IL|H₂O mixtures (data not shown) that monotonically increase up to a concentration of ~7.5 wt.% and 11 wt.% for DMBS and TFA, respectively, and then remain relatively constant until 50 wt.%. This concentration represents the point at which IL-water mixtures deviate from ideality and behave like complex fluids, which impacts the water flux during FO. I have previously shown that ion aggregation is dependent on temperature and is an intermediate step towards LCST-type phase separation, however the occurrence of aggregation at room temperature is revealed through these MD simulations and indicates an opportunity to develop new IL chemistries that take advantage of this behavior. As such, a concentration >60 wt.% is required for effective desalination using either DMBS or TFA for desalination of high-salinity feeds.

Chapter 3

Anomalous phase change of sugar alcohols encapsulated in nanopores for thermal applications

Content in this chapter will be submitted for publication as the following tentative title:

H. Kang, C Dames, J. J. Urban, “Anomalous phase change of sugar alcohols encapsulated in ZIF nanopores”, *in preparation*

3.1 Introduction

Phase change materials (PCMs) have been widely investigated to store and release thermal energy in the form of latent heat from a phase transition. Thermal energy storage based on latent heat is one of the most efficient methods for pursuing high storage density in a small temperature range [71-73]. PCMs have been integrated into the fields of solar-thermal energy storage, pumped coolants, waste heat recovery, and off-peak electricity storage systems [74-79]. Nevertheless, the widespread utilization of PCM is limited since there is no ideal material for each specific application [80].

Especially, building space heating by thermal energy storage has lacked appropriate PCMs with a desired melting temperature and heat of fusion, in contrast to ice storage air conditioning which can take advantage of the large latent heat of water. Traditionally, paraffin waxes and salt hydrates are commonly used for the heating and cooling energy demand in buildings [81]. Paraffin is chemically stable, and compositionally tunable to achieve a suitable melting temperature. However, paraffin shows poor thermal properties such as relatively low latent heat ($\Delta h_L < 200 \text{ Jg}^{-1}$), low thermal conductivity, and flammability [82]. On the other hand, inorganic salt hydrates have issues of large volume change in phase transition, corrosiveness and phase separation in spite of their good thermal properties ($\Delta h_L \sim 200\text{-}300 \text{ Jg}^{-1}$) [83]. Sugar alcohols (SAs), on the other hand, have attractive characteristics for thermal energy storage applications [80]. SAs display a high latent heat ($\Delta h_L > 300 \text{ Jg}^{-1}$) and are chemically stable, non-corrosive, non-toxic and even inexpensive [84]. However, a major challenge limiting their application in the real world is their relatively high melting temperature ($T_m > 100 \text{ }^\circ\text{C}$).

For applications integrated into building walls or with working fluids such as water, the encapsulation of PCMs is necessary to prevent the flow of liquid PCMs, phase separation, and low

heat transfer rate. Recent studies have shown the confinement of PCMs at the nanoscale to improve thermo-physical properties with a versatile strategy [73]. Metal-organic frameworks (MOFs), which is an emerging class of three-dimensional crystalline porous materials, is a promising structure because it offers nanoconfinement with high internal porosity, large surface area, and stability even at high temperatures [85]. Furthermore, the nanoconfinement can be a parameter to reduce the phase transition temperature of PCMs, which can be helpful for some applications. For example, the decrease of the phase transition temperature of polyethylene glycol (PEG) has been observed when incorporated into graphene oxide [86], nanochannels of porous coordination polymers (PCPs) [87], and carbonized MOFs [88]. Recently, our group experimentally demonstrated the first encapsulation of SAs (erythritol and xylitol) within a class of MOF without an infusion process at room temperature [89]. The nanoconfinement of the sugar alcohols was found to lower the melting point of the SAs into the operating range for water cooling applications. However, the mechanism behind the observed melting point depression and the phase identification in the nanopores is currently unknown.

3.2 Problem statement

I investigate the phases of nanoconfined SAs using molecular dynamics (MD) simulations. Despite the observation of thermal transitions of the SA-in-MOF system by differential scanning calorimetry (DSC) [89], the structural difference between the phases consisting of a few number of SA molecules in the nanopores was not explained. Due to the few-nm length scales being too small, and lack of experimental access to a MOF pore interior, it is impossible to experimentally observe behaviors of the nanoconfined SAs. Instead, a theoretical atomistic-level approach presents guidance for synthesis and composite design.

The encapsulated SAs of the previous study were simultaneously synthesized with the building blocks of a uniformly porous structure of a zeolitic imidazolate framework (ZIF) type MOF. The ZIF structure was identified as ZIF-L. ZIF-L is a two-dimensional layered ZIF structure that is made up of the same building blocks as ZIF-8. ZIF-L is a metastable phase and would transform to ZIF-8 under organic solvent interactions and temperature conditions [90,91]. The layered structure of ZIF-L has a smaller pore size and weaker crystallinity than ZIF-8, so ZIF-8 is expected to be more suitable to contain the SAs as phase change materials. Therefore, here I select ZIF-8 and additional ZIF-11 with a larger pore size as the frameworks to encapsulate sugar alcohols. ZIF-8 and ZIF-11 are both popular for their thermal and chemical stabilities, and the small aperture diameter of the channels between pores in normal conditions [92].

I further explore the thermal conductivity of the SA-infused ZIFs. The thermal conductivity, k , of ZIF-11 and the SA-ZIF composites has never been measured or calculated, to the best of my knowledge. ZIF is basically a dielectric material. The thermal conductivity of ZIF-8 was measured

($0.326 \text{ Wm}^{-1}\text{K}^{-1}$) [93] in air at the standard 1 atm and 300 K which is one order of magnitude lower than other nanoporous crystals such as zeolites sodalite ($3.5 \text{ Wm}^{-1}\text{K}^{-1}$), zeolite-A ($1.7 \text{ Wm}^{-1}\text{K}^{-1}$) [94], and amorphous silica ($1.4 \text{ Wm}^{-1}\text{K}^{-1}$) [95]. Such low k could be a critical issue when applying the composites into energy storage systems or as components of thermal circuits. Here I resolve the open question on whether the presence of SA molecules increases the composite k by adding additional heat pathways, or reduces it by introducing a new phonon scattering source [96].

3.3 Model and method

I select ZIF-8 and ZIF-11 as the frameworks for encapsulating sugar alcohols (Fig. 3-1). They are suitable for this encapsulation because their rather large pore size (ZIF-8: 11.6 \AA , ZIF-11: 14.6 \AA) holds more SA molecules while the small inter-pore aperture diameter (ZIF-8: 3.4 \AA , ZIF-11: 3.0 \AA) prevents diffusion between pores [92]. In addition, the ZIFs have the same tetrahedrally-coordinated transition metal ion, Zn(II), and similar imidazolate linkers, meaning they have similar internal surface interactions.

For the MD simulation of this system, the all-atom AMBER force fields for potential energy U are used:

$$\begin{aligned}
 U_{potential} = & \sum_{i>j} \left[4\epsilon_{ij} \left\{ \left(\frac{\sigma_{ij}}{r_{ij}} \right)^{12} - \left(\frac{\sigma_{ij}}{r_{ij}} \right)^6 \right\} + \frac{q_i q_j}{4\pi\epsilon_0\epsilon_r r_{ij}} \right] + \sum_{bonds} K_r (r - r_0)^2 + \sum_{angles} K_\theta (\theta - \theta_0)^2 \\
 & + \sum_{torsions} \frac{K_\phi}{2} \{1 + \cos(n\phi - \gamma)\} + \sum_{impropers} K_\chi (\chi - \chi_0)^2
 \end{aligned} \tag{3.1}$$

The first term describes the non-bonded interactions including Van der Waals as the Lennard-Jones 12-6 form and Coulombic forces from atom-centered partial charges q ; this includes interactions between SAs and ZIF and among different SA molecules. The next terms in Eq. (3.1) represent, respectively, bond stretching, bond bending, and proper and improper torsional interactions. I apply a force field developed for ZIF-8 with structural flexibility [97] to both ZIFs since they share mostly the same bonded interactions of stretching, bending, and torsion. However, to the best of my best knowledge, the partial charges for ZIF-11 have not been studied with a reliable treatment, so here I first calculate them using a density functional theory simulation with DDEC6 methodology [98]. To unify the partial charge methodology for both ZIFs, the partial charges of ZIF-8 are also calculated with the same method. The details of the force field parameters and partial charges for the ZIF-8 and ZIF-11 are summarized in Tables 3-1 and 3-2, respectively.

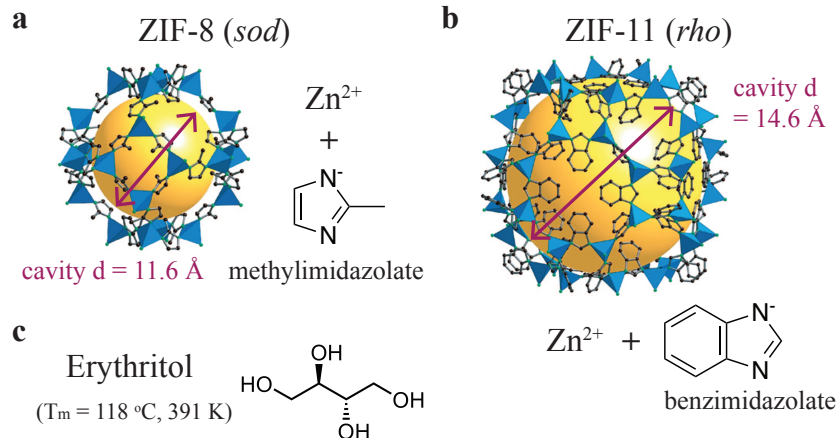


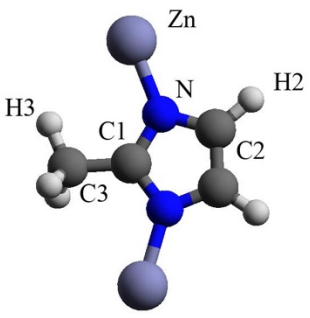
Figure 3-1. Structure of (a) pristine ZIF-8 (*sod*, lattice constant, $a=b=c=16.99 \text{ \AA}$) and (b) ZIF-11 (*rho*, lattice constant, $a=b=c=28.76 \text{ \AA}$), both functioning as frameworks [92], and (c) erythritol as the phase change material. For each ZIF structure, Zn ions are represented as tetrahedra and the largest cavity in the pores by a yellow sphere that fits into the framework without touching any atoms. H atoms are omitted here for clarity but were included in the MD simulations. *Copyright (2006) National Academy of Sciences, U.S.A.*

Regarding sugar alcohols, this study focuses on erythritol as a representative of sugar alcohols having hydroxyl (OH) groups. The thermodynamic properties of sugar alcohols are substantially affected by the OH group which forms strong intermolecular hydrogen bonds [99]. Bulk erythritol has an outstanding heat of fusion ($\Delta h_m=337 \text{ Jg}^{-1}$) among sugar alcohols and a melting point ($T_m=118 \text{ }^\circ\text{C}$, 391 K) [100] not too far from the liquid water working range. The short carbon chain is also suitable for being confined in the nanopores of a ZIF. I use force field parameters for erythritol which were used in a previous MD analysis of C6 sugar alcohols [99] and the details are summarized in Table 3-3.

MD simulation is performed using the LAMMPS package with standard 3D periodic boundary conditions. The non-bonded interactions are cut off at 12 \AA while the Ewald summation method is applied to treat the long-range electrostatic interactions. The VdW interaction parameters between unlike atoms were obtained by the Lorentz–Berthelot combining rule. The non-bonded interactions separated by exactly three consecutive bonds (1–4 interactions) are reduced by related scaling factors which are optimized as 0.50 for VdW interactions and 0.83 for electrostatic interactions, respectively [61,62]. For the upcoming investigation of the structure and melting temperature of the SA-ZIF composites (shown later in Fig. 3-8), the Nose-Hoover thermostat and barostat [101] is applied to the ZIF structures. All simulations are carried out at atmospheric pressure. The erythritol molecules are initially placed with an original crystal structure

in the pores. After initial relaxation and equilibration, at least 3 ns of simulation is performed for each temperature condition with a fixed time step of 1.0 fs. The simulation system sizes are summarized in Tables 3-4 and 3-5, where the notation “*npP*” means “*n* erythritol molecules per pore.”

Table 3-1. Force field parameters for ZIF-8 framework.



atoms	σ (Å)	ϵ (kcal/mol)	partial charge (e)
Zn	1.960	0.0125	0.6326
N	3.250	0.1700	-0.3591
C1	3.400	0.0860	0.3961
C2	3.400	0.0860	-0.0854
C3	3.400	0.1094	-0.5759
H2	2.511	0.0150	0.1109
H3	2.471	0.0157	0.1769

bonds	r_0 (Å)	K_r (kcal/mol Å ²)
C1-C3	1.490	346.543
C1-N	1.335	488.000
C2-C2	1.350	540.249
C2-N	1.370	440.210
C2-H2	1.080	367.000
C3-H3	1.090	340.000
Zn-N	2.011	78.500

torsions ^a	γ_0 (deg)	K_ϕ (kcal/mol)	n
X-C1-N-X	180	5.000	2
X-C2-N-X	180	2.325	2
X-C2-C2-X	180	5.150	2

angles	θ_0 (deg)	K_θ (kcal/mol rad ²)
C1-C3-H3	109.32	48.088
C1-N-C2	105.27	71.254
C1-N-Zn	128.33	48.680
C2-C2-N	108.65	73.750
C2-C2-H2	125.67	49.451
C2-N-Zn	126.40	32.477
C3-C1-N	123.92	66.015
H3-C3-H3	109.50	35.000
N-C1-N	112.16	75.484
N-C2-H2	125.68	49.954
N-Zn-N	109.48	35.240

improper	ψ_0 (deg)	K_ψ (kcal/mol rad ²)
N-C3-C1-N	180	2
C2-H2-C2-N	180	2
C2-Zn-N-C1	180	2

The force field for ZIF-8 cites the results from [97].

^a X denotes wildcard atoms. i.e., X-A-B-X means any dihedral combination having A-B as central atoms. Unmentioned combinations are assumed as negligible torsional potential.

Table 3-2. Force field parameters for ZIF-11 framework.

bonds	r_0 (Å)	K_r (kcal/mol Å ²)
C4-H4	1.080	367.00
C4-N	1.335	488.00
C5-C5	1.350	540.25
C5-CA ^b	1.404	469.00
C5-N	1.370	440.21
CA-CA ^b	1.400	469.00
CA-HA ^b	1.080	367.00
Zn-N	2.011	78.50

torsions ^a	ψ_0 (deg)	K_ψ (kcal/mol)	n
X-C4-N-X	180	5.000	2
X-C5-N-X	180	2.325	2
X-C5-C5-X	180	5.150	2
X-C5-CA-X ^b	180	14.000	4
X-CA-CA-X ^b	180	14.500	4

atoms ^c	σ (Å)	ϵ (kcal/mol)	partial charge (e)
Zn	1.960	0.0125	0.6342
N	3.250	0.1700	-0.3584
C4	3.400	0.0860	0.1712
C5	3.400	0.0860	0.1434
CA α	3.400	0.0860	-0.1730
CA β	3.400	0.0860	-0.0953
H4	2.420	0.0150	0.0847
HA α	2.511	0.0150	0.1004
HA β	2.511	0.0150	0.0964

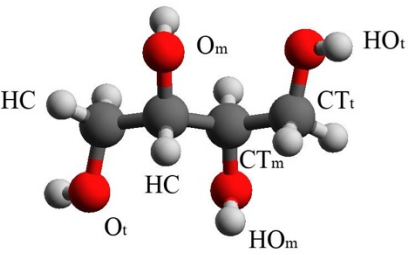
angles	θ_0 (deg)	K_θ (kcal/mol rad ²)
C4-N-C5	105.33	71.254
C4-N-Zn	128.33	48.680
C5-C5-CA ^b	120.00	63.000
C5-C5-N	108.65	73.750
C5-CA-CA ^b	120.00	63.000
C5-CA-HA ^b	120.00	50.000
CA-C5-N ^b	132.40	70.000
CA-CA-CA ^b	120.00	63.000
CA-CA-HA ^b	120.00	50.000
N-C4-H4 ^b	120.00	50.000
N-C4-N	112.16	75.484
N-Zn-N	109.48	35.240
Zn-N-C5	126.40	32.477

improper	ψ_0 (deg)	K_ψ (kcal/mol rad ²)
C4-Zn-N-C5	180	2
C5-CA-C5-N	180	2
C5-HA-CA-CA	180	2
CA-CA-HA-CA	180	2
N-H4-C4-N	180	2

^a X denotes wildcard atoms. i.e., X-A-B-X means any dihedral combination having A-B as central atoms. Unmentioned combinations are assumed as negligible torsional potential.

^b The force field for ZIF-11 except for b marked terms cites the results from [97]. The b marked terms cite the general AMBER force field.

^c Subscripts α and β correspond to the description for CA, HA in a benzene ring, which is expressed in the inset structure schema.

Table 3-3. Force field parameters for erythritol.


bonds	r_0 (Å)	K_r (kcal/mol Å ²)
CT-CT	1.410	320.0
CT-CT	1.526	310.0
CT-HC	1.090	- ^d
O-HO	0.960	- ^d

torsions ^a	γ_0 (deg)	K_φ (kcal/mol)	n
X-CT-CT-X	0	0.156	3
X-CT-O-X	0	0.167	3

atoms ^c	σ (Å)	ϵ (kcal/mol)	partial charge (e)
CT _t	3.400	0.0125	0.145
CT _m	3.400	0.1700	0.205
O _t	3.066	0.2104	-0.683
O _m	3.066	0.2104	-0.700
HO _t	0.000	0.0000	0.418
HO _m	0.000	0.0000	0.435
HC	2.471	0.0157	0.060

angles	θ_0 (deg)	K_θ (kcal/mol rad ²)
HC-CT-HC	109.5	35.0
O-CT-HC	109.5	50.0
CT-O-HO	108.5	55.0
CT-CT-HC	109.5	50.0
CT-CT-O	109.5	50.0
CT-CT-CT	109.5	40.0

The force field for erythritol cites the results from [99].

^a X denotes wildcard atoms. i.e., X-A-B-X means any dihedral combination having A-B as central atoms.

^c Subscripts *t* and *m* correspond to the terminal and mid CT, T, HO units in a carbon backbone.

^d The CT-HC and O-HO bonds are held rigid by the SHAKE method.

Table 3-4. Simulation system size for the encapsulated erythritol in ZIF-8.

case	supercell size	ZIF atoms	# of erythritol per pore	total # of erythritol ^a	erythritol atoms	total atoms	
pristine			-	-	-	2208	
3pP			3	48	864	3072	
ZIF-8	4pP	2 x 2 x 2	2208	4	64	1152	3360
	5pP			5	80	1440	3648
	6pP			6	96	1728	3936

^a A ZIF-8 (sod) unit cell has two pores, like a BCC structure.

Table 3-5. Simulation system size for the encapsulated erythritol in ZIF-11.

case	supercell size	ZIF atoms	# of erythritol per pore	total # of erythritol ^a	erythritol atoms	total atoms
pristine			-	-	-	2784
4pP			4	16	288	3072
8pP	1 x 1 x 2	2784	8	32	576	3360
12pP			12	48	864	3648
16pP			16	64	1152	3936
20pP			20	80	1440	4224

^a A ZIF-11 (rho) unit cell has two pores, like a BCC structure.

3.4 Structure analysis

3.4.1 ZIFs containing erythritol

I first analyze the structural characteristics of ZIFs containing erythritol molecules (Fig. 3-2). The applied force field renders the lattice constant of ZIF-8 comparable with available experimental data [102,103] within 2%, as shown in Fig. 3-2a. Upon beginning to add SAs into the ZIF pores, Fig. 3-2a shows that the lattice constant of the ZIF composites reduces, which is due to the attractive interaction between the ZIF structure and SA molecules, and between the SA molecules themselves. However, above a certain number of erythritol molecules in a pore, the lattice constant begins to expand, due to the limitation of physical pore size. For example, this constraint effect is seen in Fig. 3-2a for 5 and 6 molecules per pore. Similarly, for ZIF-8 with 5 and especially 6 erythritol molecules per pore (6pP), the thermal expansion trend is different from the pristine ZIF-8 case and few-pP cases, indicating that the thermal expansion of the composite is dominated by the thermal expansion of the erythritol molecules (The volumetric coefficient of thermal expansion, α_V of ZIF-8 [104] is 11.9 MK^{-1} smaller than that of solid and liquid erythritol [100], 29.4 MK^{-1} and 395 MK^{-1} , respectively). For ZIF-11 (Fig. 3-2d), although shrinking of the framework size is not observed in the small quantity cases (4pP and 8pP) due to the larger pore size having enough empty space, further increasing the number of erythritol molecules gives the same trends as seen for the ZIF-8 composites in Fig. 3-2a.

Note that the lattice constants of 6pP in ZIF-8 and 20pP in ZIF-11 exceed that of pristine ZIFs in the temperature range of my interest ($< 400 \text{ K}$), which has the potential to break the ZIF structures in a real application. Therefore, I conclude that ZIF-8 and ZIF-11 safely contain up to 5 and 16 erythritol molecules per pore, respectively. Then, in order to check the diffusibility between

pores, I track the absolute displacement of every erythritol molecule from their respective origins at the highest loading conditions, and present representative results of a subset of molecules in Figs. 3-2b and 3-2e. As expected, based on the small inter-pore aperture diameter of the ZIFs, the absolute displacement does not exceed a certain distance, which means that erythritol molecules move around only within their original pore. Figures 3-2c and 3-2f show the maximum distance of every erythritol molecule itself during their 3 ns trajectory. ZIF-8 and ZIF-11 have the allowable cavity distance for erythritol as around 10 Å and 20 Å, respectively. The latter is larger than the nominal inner spherical cavity diameter of $d=14.6$ Å indicated in Fig. 3-1, but this is reasonable since the accessible spherical cavity diameter is somewhat larger due to the free space in between the benzimidazolate molecules. Furthermore, I notice from Figs. 3-2c and 3-2f that the encapsulated erythritols at low temperatures (200 K) are no longer mobile but rather vibrate locally within a ~ 3 -5 Å range. The distinction between these two phases (the mobile, liquid-like, high-temperature phase; and the immobile, low-temperature phase) will be discussed further below.

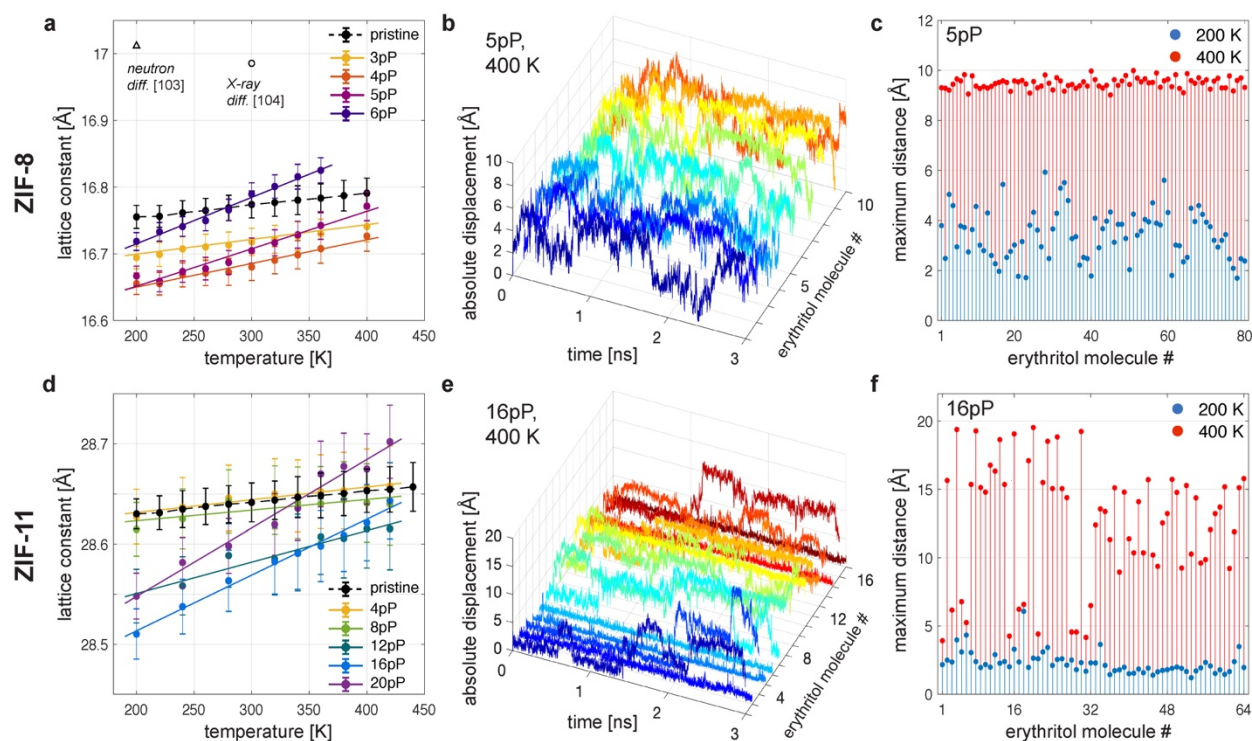


Figure 3-2. Structural analysis of ZIF-8 (top row) and ZIF-11 (bottom row) containing various numbers of erythritol molecules. (a,d) Effect on lattice constant according to the number of erythritol molecules per pore. (b,e) Absolute displacement (center of mass) of erythritol molecules from an origin time. Only a representative subset of molecular trajectories (10 in b, 16 in e) is shown here for visibility. (c,f) Accessible internal cavity size as determined by the maximum distance among trajectories of each erythritol molecule.

3.4.2 Encapsulated erythritols

The radial distribution function (RDF), $g(r)$, is used to understand structural features of the encapsulated erythritol molecules. The $g(r)$ is defined as

$$g(r) = \frac{dn(r)}{\rho_n 4\pi r^2 dr} \quad (3.2)$$

where $n(r)$ is the number of particles within a shell of thickness dr and ρ_n is the average number density of the particles in each simulation system. Figure 3-3 explains the erythritol structure by the RDFs of two significant atomic relations through comparisons with that of the solid and liquid state of pure erythritol from additional simulations. First, the mid-carbon (CT_m) atoms are taken as the central reference site showing the general density distribution. Figures 3-3a and 3-3c show that the RDFs between CT_m of the encapsulated erythritol are similar to the RDFs of the liquid state of pure erythritol, i.e. relatively slowly varying $g(r)$ with few peaks, for the entire temperature range, in spite of the initially placed crystal structure of erythritol. Hydrogen bonds among their OH groups are also the key interaction that attracts SA molecules to each other. The major difference between pure crystal and liquid erythritol is the hydrogen bond between terminal-oxygen (O_t) atoms and mid-hydrogen (HO_m) atoms. For the crystalline structure, the combination of O_t and HO_m hardly constitutes hydrogen bonds, which would show up as a strong first peak at around 2 Å on the RDF graph between O and H. On the other hand, the amorphous liquid state does form hydrogen bonds and its RDF between O_t and HO_m (black dashed lines in Figs. 3-3b and 3-3d) shows a strong peak at 2 Å. The encapsulated erythritol O_t - HO_m RDF results show a similar strong peak around 2 Å and other similar RDF features as pure erythritol liquid. Therefore, I conclude that the boundary attractive interaction of SAs with the ZIF framework frustrates the SA crystallization and causes them to remain in an amorphous structure.

Nevertheless, I can notice some evidence that there are two distinguishing amorphous phases from the RDF graphs. At the lower temperatures of Fig. 3-3 there are some signatures of the beginning of ordering. The first peak (around 5.5 Å) of the CT_m RDF splits and the movement of secondary peaks (the range of 3 to 5 Å) of the RDF between O_t and HO_m are observed at the low-temperature range. The melting temperature (T_m) of encapsulated erythritol is definitely reduced from the original melting temperature (of 391 K), and the depression amount for the encapsulation with ZIF-8 is larger than with ZIF-11 due to the stronger interaction by the smaller pore size.

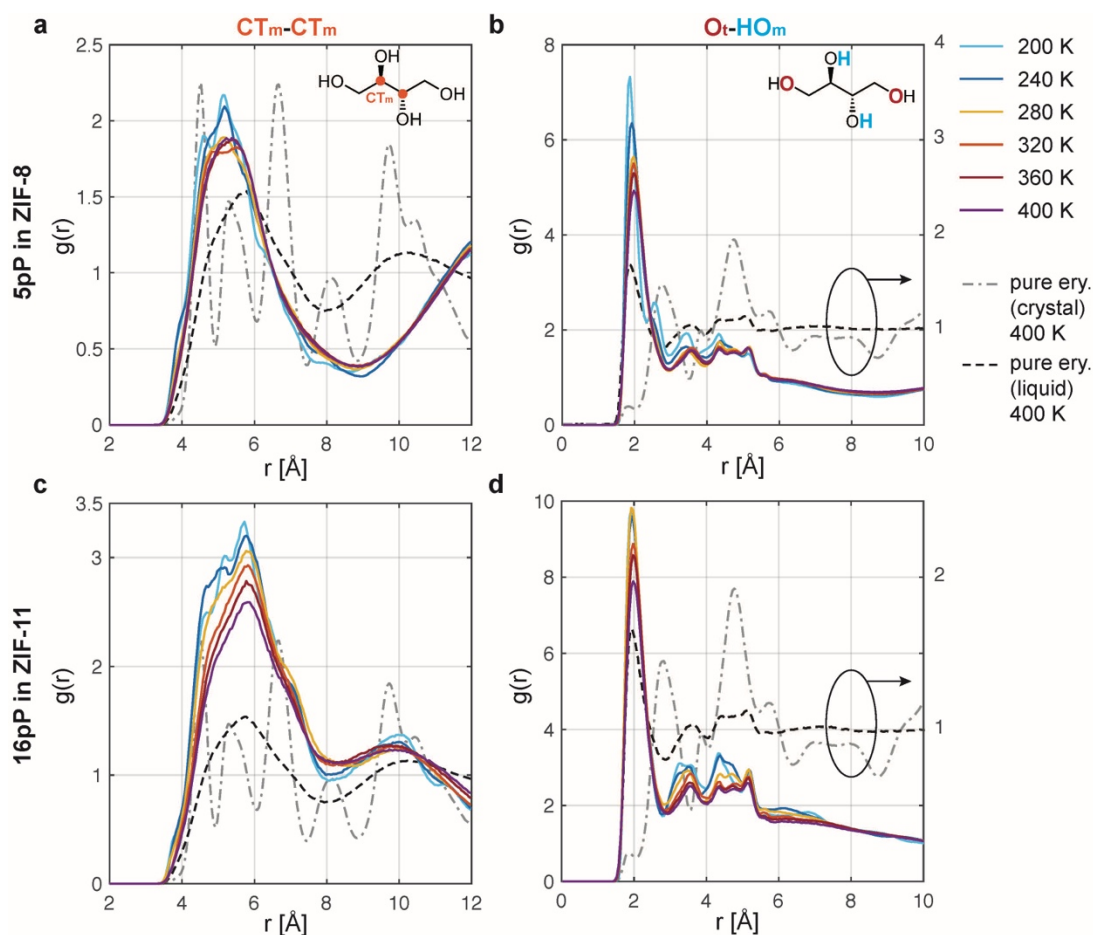


Figure 3-3. Radial distribution function among erythritol molecules inside ZIF-8 (top row) and ZIF-11 (bottom row). (a,c) RDF between the mid-carbon (CT_m) atoms. (b,d) RDF between terminal-oxygen (O_t) atoms and mid-hydrogen (HO_m) atoms

3.5 Melting temperature of encapsulated erythritols

Melting temperature T_m is one of the most important and interesting properties for the composites. Although the depression of T_m was observed from the RDF analysis, determining T_m with a higher accuracy is required to understand further the amorphous phases. Many methods in MD simulation have been developed for the computation of T_m : the hysteresis method, the voids method, and the solid-liquid interface method as direct methods; and the free energy methods as indirect methods [105]. However, those direct methods are not suitable for materials with a small number of atoms/molecules and the indirect methods require a clear understanding of the two reference phases. In order to figure out the T_m of the nanoconfined erythritols, I here take a different approach, beginning with the fundamentals of particle diffusion. The mean squared displacement (MSD) has been generally used to measure a diffusion coefficient:

$$\text{MSD} \equiv \langle |\mathbf{x}(t) - \mathbf{x}_0|^2 \rangle = \frac{1}{N} \sum_{i=1}^N |\mathbf{x}^{(i)}(t) - \mathbf{x}^{(i)}(0)|^2, \quad (3.3)$$

where N is the number of particles in simulation system, vector $\mathbf{x}^{(i)}(t)$ is the position of the i -th particle at time t , and $\mathbf{x}^{(i)}(0) = \mathbf{x}_0^{(i)}$ is the reference position of the i -th particle. Figure 3-4a presents the trends of MSD of two idealized systems (bulk liquid, bulk solid) as well as the system considered here in which a liquid is confined to a small fixed volume. For identification of bulk phases, it would be straightforward to distinguish liquid from solid phases from an $\text{MSD}(t)$ calculation accordingly, by looking for either MSD increasing linearly with t or saturating with t .

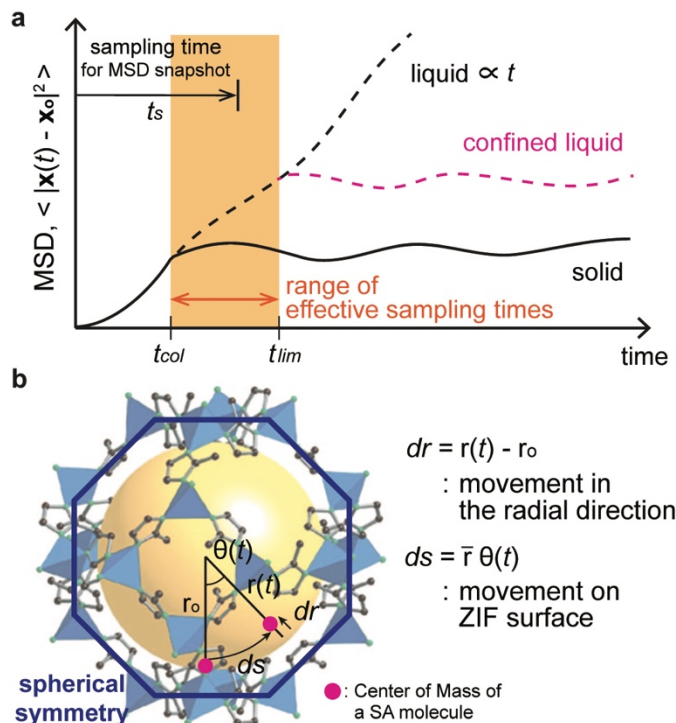


Figure 3-4. Mean squared displacement. (a) Conceptual examples of two idealized systems (bulk liquid, bulk solid) and the confined liquid system. (b) The split of movement of an SA molecule into circumferential (ds) and radial (dr) directions based on the spherical symmetry of a ZIF pore.

However, in the confined systems, the MSD saturates for the liquid phase as well as the solid phase. Such a saturated long-time $\text{MSD}(t)$ behavior was confirmed in these systems at all temperatures considered (Fig. 3-5). Nevertheless, theoretically the difference between the solid-

like and liquid-like phases in the confined volume can still be observed in a shorter effective sampling time range (highlighted as the orange color in Fig. 3-4a) after the collision time, t_{col} , and before the time limit, t_{lim} , which scales with the accessible cavity size ($\sim d$ of Fig. 3-1). To calculate the MSD I analyze a snapshot of the simulation at some sample time, t_s , which must be chosen carefully. If t_s is too short, i.e. $t_s < t_{col}$, even liquid phases will not have had enough time for their molecules to diffuse around significantly, and the MSD of liquid and solid phases will be indistinguishable. Then for a range of $t_s > t_{col}$, the MSD(t) curves for solid and confined liquid phases will diverge: the solid phase MSD(t) saturates for $t_s > t_{col}$ while the confined-liquid phase MSD(t) will continue increasing. Finally, if t_s is too large, i.e. $t_s > t_{lim}$, the confined-liquid's MSD(t) will also saturate due to the finite pore confinement volume. Thus, the best regime for distinguishing solid from confined-liquid phases based on their different MSD(t) slopes is the orange zone in the figure. Below the movements of the erythritol molecules are analyzed by dividing them into tangential and perpendicular movement to the ZIF surface. The *sod* structure of ZIF-8 and *rho* structure of ZIF-11 are approximately spherically symmetric, so the MSD can be expressed by the movement in the radial direction and on the ZIF surface, dr and ds , with the convenience of spherical coordinates as detailed in Fig. 3-4b.

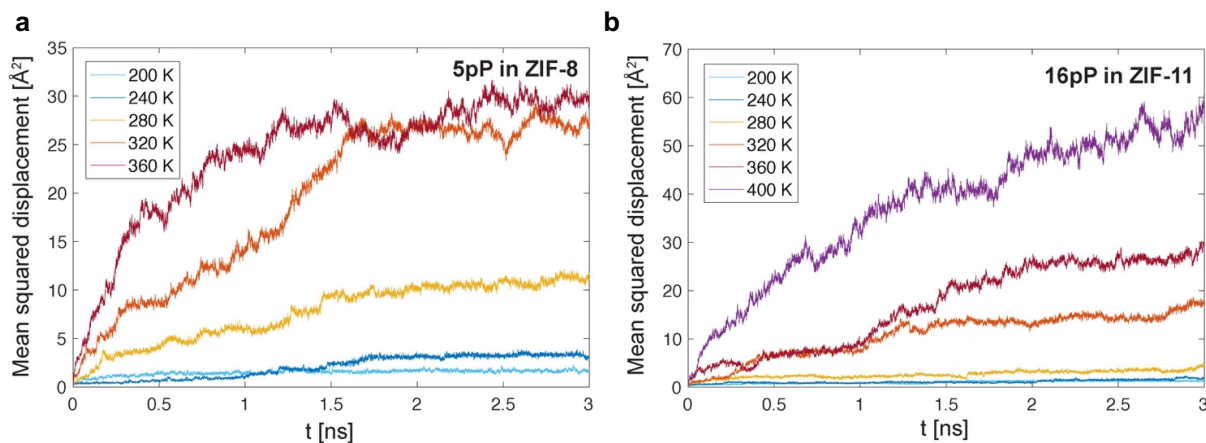


Figure 3-5. Mean squared displacement of erythritol molecules inside ZIF pores. (a) 5pP in ZIF-8. (b) 16pP in ZIF-11. The saturated trend of MSD at long times shows that erythritol molecules cannot diffuse between the ZIF pores.

I consider 5 sampling times, $t_s=0.5$ ps, 1.0 ps, 1.5 ps, 2.0 ps and 2.5 ps, to identify the phases and t_{col} . The results of the snapshotted MSD at the 5 prescribed sampling times are summarized in Fig. 3-6. To better compare the 2d movement of ds vs. the 1d movement of dr on the same footing, I choose to plot $(ds^2)/2$ in the figure. Figure 3-6 reveals several phenomena. First, in all of the cases tested the movement of the SA molecules along the ZIF surface is equal to or larger than movements in the radial direction, i.e. $(ds^2)/2 \geq dr^2$, with the largest differences occurring

at high temperature and in the ZIF-8 whose pore size is smaller. Since the interaction between erythritol and ZIFs is attractive as observed above, the perpendicular movement of erythritol away from the pore surface (dr) is limited, like adsorbates on a 2d substrate; while circumferential diffusion (ds) while still adsorbed to the pore surface is relatively easier. This phenomenon is exaggerated in ZIF-8 rather than ZIF-11, since in the latter some erythritol molecules can be located without adjacent interaction with the pore surface due to the larger pore size. Thus, I determine the collision time, t_{col} , by focusing on the MSD(t) results of the dominant movement, ds^2 . At temperatures low enough that the SA molecules can be considered as a solid-like phase, the MSD evaluated at sampling times $t_s > t_{col}$ should converge and saturate as explained in Fig. 3-4a.

Although t_{col} is dependent on the temperature and the number density, I can start the temperature region that the results with the most of sampling times converge except for the shortest sampling time, $t_s = 0.5$ ps. The erythritol is decided as solid-like phase where the sole separation of happens because of the shortest $t_s < t_{col}$ and the others' $t_s > t_{col}$. At lower temperature, the lesser mobility and larger t_{col} makes that ds^2 becomes independent of t_s due to all $t_s < t_{col}$, as shown in Figs. 3-6b to 3-6d. Recalling again the discussion around Fig. 3-4a, if the SA molecules act as liquid-like, the MSD increases with t_s as t_s in the effective range ($t_{col} < t_s < t_{lim}$) increases. Finally, for each sample and temperature, I assess whether ds^2 keeps increasing with $t_s > t_{col}$, or saturates, and use this to judge whether that condition is liquid-like or solid-like. The boundary temperature between these two phase regimes is identified as T_m and is marked by the dashed red lines in Fig. 3-6.

Like the simple observation in Fig. 3-3, the analysis in Fig. 3-6 also shows T_m of erythritol is reduced by the encapsulation in nanopores from the original bulk T_m of 391 K. The T_m depression is stronger for smaller pore sizes and smaller number of SA pP. Although Fig. 3-6 shows the movements of SA along the ZIF surface dominate those normal to it ($ds > dr$) due to the attractive interaction between SA and ZIF, there are no hydrogen donor or acceptor sites in the ligands of ZIF structures. The RDFs between erythritol and ZIFs also support the absence of hydrogen bonds (Figs. 3-7 and 3-8). Compared to the first-order phase transition of pure erythritol with its strong hydrogen bonds, the required kinetic energy for the second-order phase transition between amorphous phases of encapsulated SA is relatively lower; this also reduces the T_m . The balance between the hydrogen bonding interaction among SAs and the effect from attractive potential field of ZIF surface can also be understood through the surface-to-volume ratio. As more erythritol molecules are contained in a pore, there are relatively more “interior” SA molecules than “boundary” SA molecules which adjacently interact with ZIF pore surface; since the T_m depression is mainly due to those “boundary” molecules, reducing the effective surface-to-volume ratio in this way also tends to reduce the T_m depression. The same principle holds for the ZIF-11 with the larger pore size which means the smaller surface-to-volume ratio.

The effect from the attractive potential field of ZIF surface can be probed through the ratio

between two directional movements, $2\langle dr^2(t_s) \rangle / \langle ds^2(t_s) \rangle$. This ratio reflects the degree of the weaker effect of the ZIF surface, and so approaches to 0 if the surface attractive interaction is very strong and must equal 1 for pure bulk erythritol. I focus on times $t_s \geq t_{col}$ (where $t_s \geq 1.0$ ps). For all T, the results in Fig. 3-6 show that this ratio increases for the cases with more erythritol in a pore, for example compare $2\langle dr^2(t_s) \rangle / \langle ds^2(t_s) \rangle$ for Fig. 3-6a and Fig 3-6b. The ratio is also increasing towards 1 in the ZIF-11 as compared to ZIF-8 (compare top and bottom rows) which also makes sense because the ZIF-11 has a larger pore volume, in other words, the surface effect weakens and the SA experiences a more bulk-like environment overall.

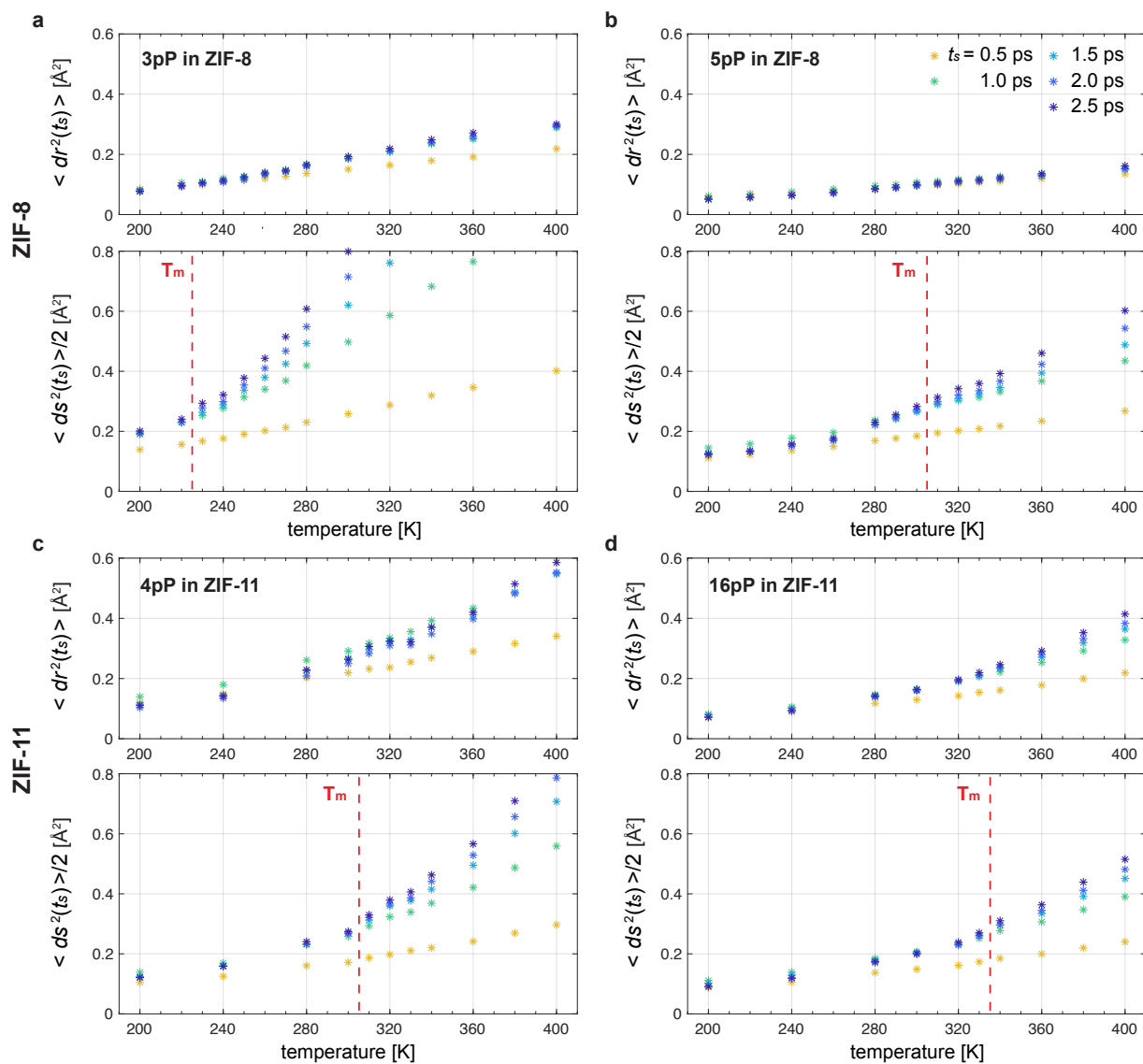


Figure 3-6. Mean squared displacements of encapsulated erythritol as a function of temperature, evaluated at the 5 different sampling times listed in panel (b,top). I decompose these displacements into the radial direction (dr^2 ; upper plot in each pair) and along the surface of the ZIF's approximately-spherical pore (ds^2 ; lower plot in each pair), as indicated in Fig. 3-4b. (a) 3pP in ZIF-8. (b) 5 pP in ZIF-8. (c) 4 pP in ZIF-11. (d) 16 pP in ZIF-11. In each case the melting temperature, T_m , is determined and indicated by a vertical red dashed line. For each sample, I define its T_m such that for all $T < T_m$ the ds^2 data is practically independent of t_s for $1.0 \text{ ps} \leq t_s \leq 2.5 \text{ ps}$, while for all $T > T_m$ the ds^2 data increases significantly with increasing $t_s \geq 1.0 \text{ ps}$.

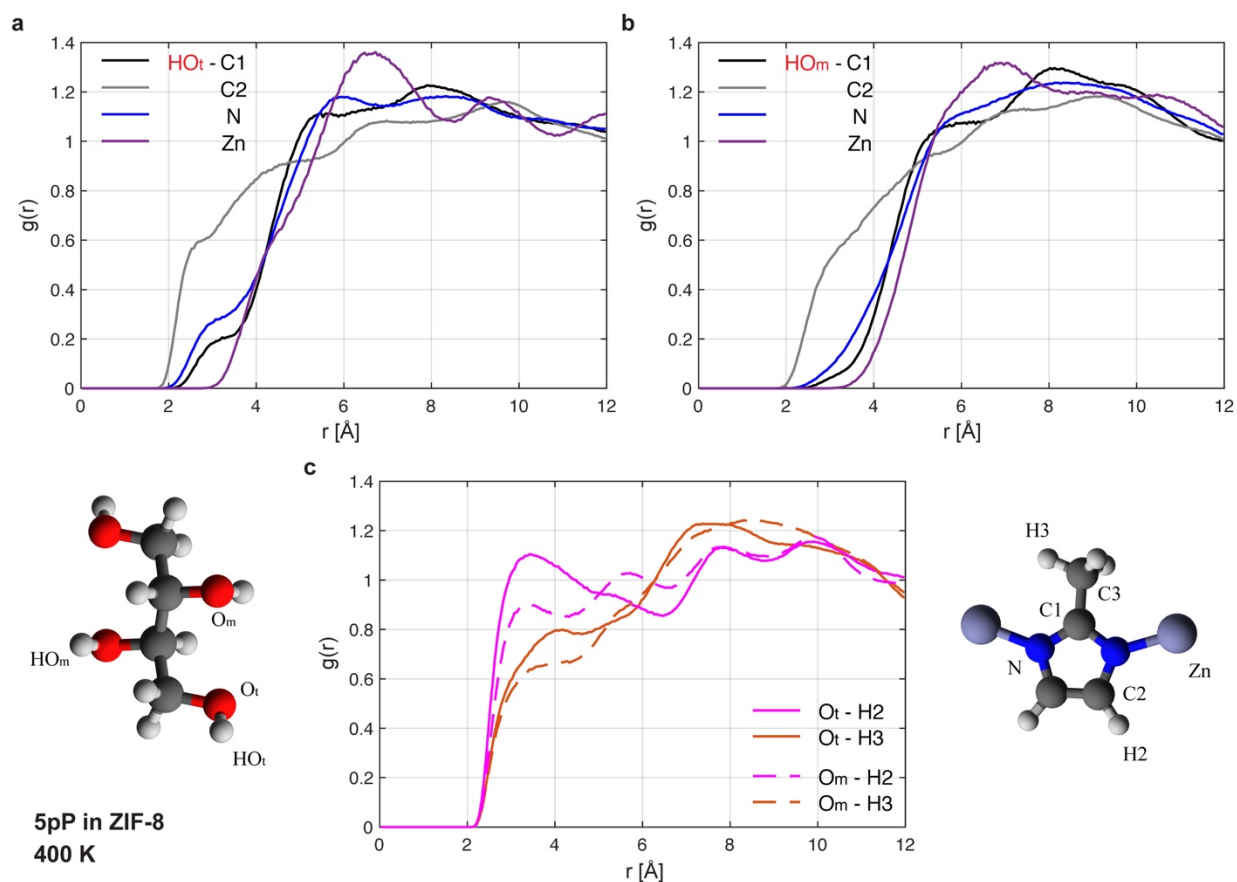


Figure 3-7. Radial distribution function at possible hydrogen bonding pairs between SAs and ZIF-8. If hydrogen bonds were present, a strong first peak would show up around 2 Å. (a) Pairs between HO_t atom in erythritol and four types of non-hydrogen atoms in ZIF-8. (b) Pairs between HO_m atom in erythritol and four types of non-hydrogen atoms in ZIF-8. (c) Pairs between oxygen atoms in erythritol and hydrogen atoms in ZIF-8. In all cases no hydrogen-bonding peaks are seen.

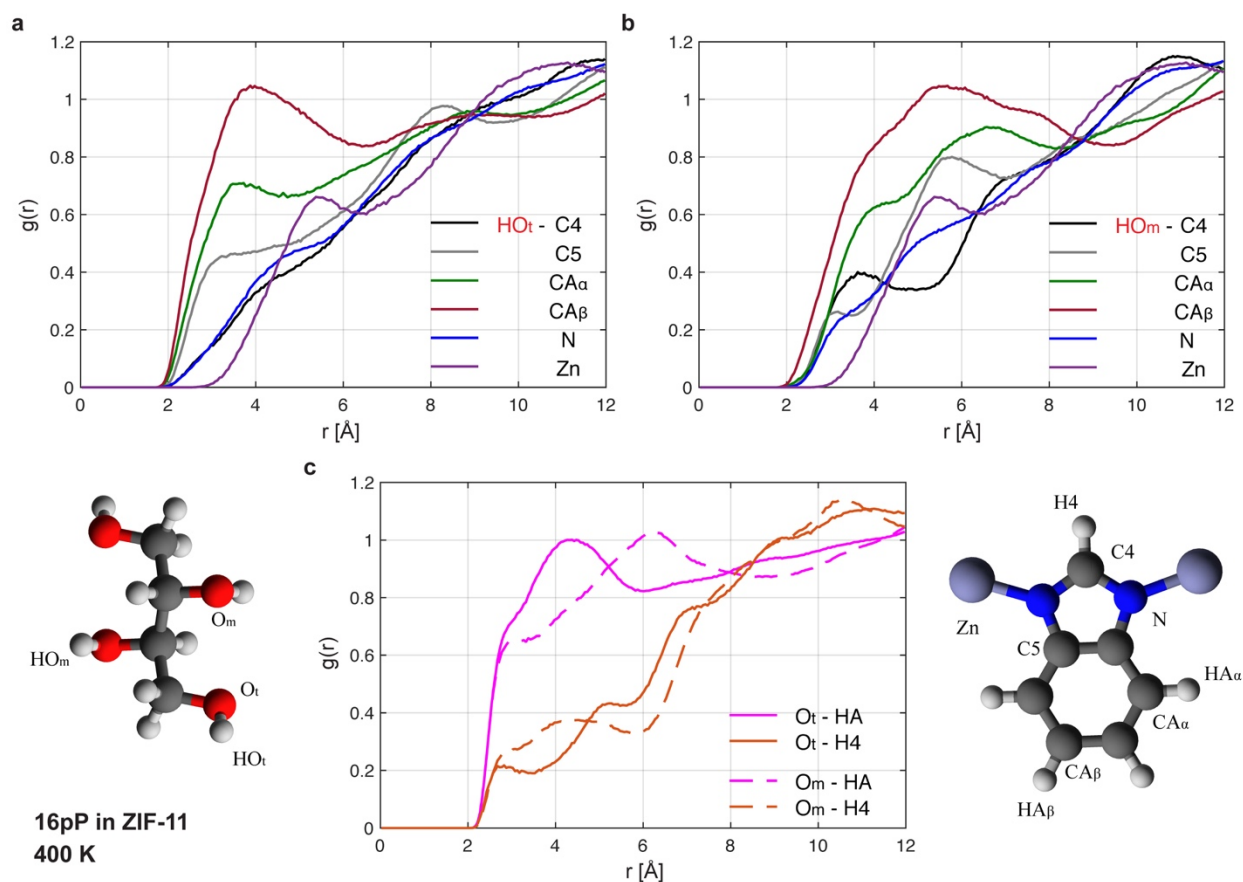


Figure 3-8. (Like Fig. 3-7 but here for ZIF-11). Radial distribution function at possible hydrogen bonding pairs between SAs and ZIF-11. If hydrogen bonds were present, a strong first peak would show up around 2 Å. (a) Pairs between HO_t atom in erythritol and six types of non-hydrogen atoms in ZIF-11. (b) Pairs between HO_m atom in erythritol and six types of non-hydrogen atoms in ZIF-11. (c) Pairs between oxygen atoms in erythritol and hydrogen atoms in ZIF-11. In all cases no hydrogen-bonding peaks are seen.

3.6 Thermal conductivity

The thermal conductivity, k , of the pristine ZIFs and the composites with encapsulated erythritol is predicted by Green-Kubo method [106]. The GK method has been used to investigate the thermal properties of dielectric materials, and recently for MOFs [107,108]. Since both ZIF-8 and ZIF-11 have cubic symmetry, their k is isotropic, which the GK method calculates as

$$k = \frac{1}{3k_B T^2 V} \int_0^\infty \langle \vec{J}(0) \cdot \vec{J}(t) \rangle dt, \quad (3.4)$$

where k_B is the Boltzmann constant, V is the system volume, $\vec{J}(t)$ is the heat current, and $\langle \vec{J}(0) \cdot \vec{J}(t) \rangle$ is the heat current autocorrelation function (HCACF). The heat current is given by

$$\vec{J}(t) = \frac{d}{dt} \sum_i^N r_i E_i \quad (3.5)$$

where r_i and E_i are the position and total energy of particle i .

In this thermal conductivity investigation, I applied a shorter timestep, 0.5 fs. To prevent a divergence issue caused by a longer phonon lifetime at low temperatures, I prepared a larger simulation size with a 2x3x4 supercell for the pristine ZIF-8 and its composite cases, and a 1x2x3 supercell for the pristine ZIF-11 and its composite cases. The system is run first in an NPT and then NVT ensemble to set the temperature and volume. After the system has reached equilibrium, the heat current is obtained from runs in an NVE ensemble over 4 ns, then the thermal conductivity is obtained from the integral of the HCACF. For good convergence, every successive 10 ps of heat current data is treated as a different independent sample of the HCACF for use in Eq. (3.4). A running average is applied to define a convergence region [107], then the thermal conductivity reaches a constant value at around 8 ps (Fig. 3-9). At each temperature and case, at least three independent runs are performed, and the averaged value is considered for the following discussion.

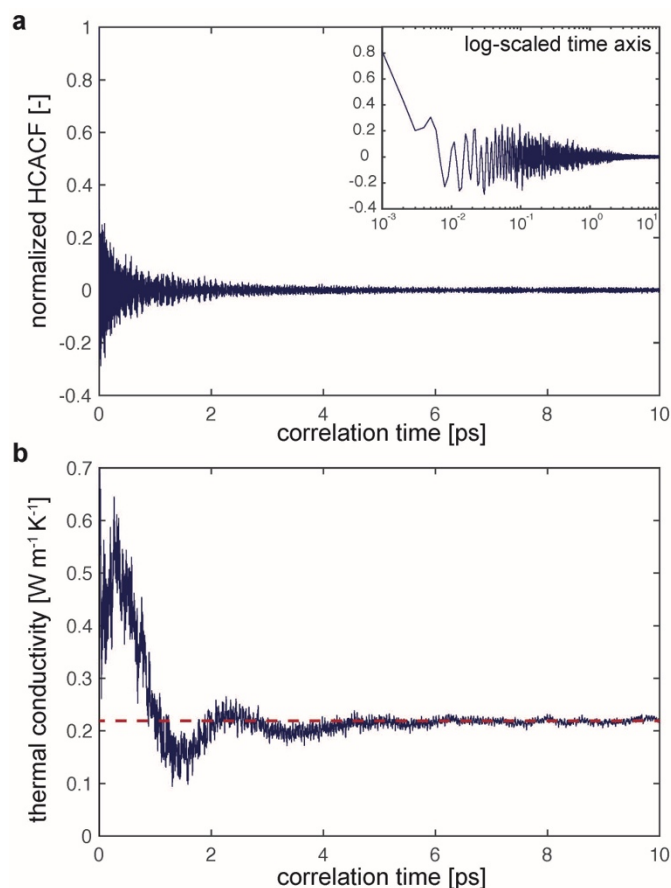


Figure 3-9. (a) Normalized heat current autocorrelation function and (b) thermal conductivity by using the Green-Kubo method as a function of correlation time, both for the pristine ZIF-8 at 400 K.

Figure 3-10 presents the result of this thermal conductivity calculation for pristine ZIF-8, pristine ZIF-11, and their composites with various numbers of erythritol molecules inside their pores. For context, a previous MD study with the Green-Kubo method had predicted the thermal conductivity of pristine (empty pores) ZIF-8 at 300 K and 1 bar as $0.165 \text{ Wm}^{-1}\text{K}^{-1}$ [108], which was the same order of magnitude as an experimental measurement [93] of in-air thermal conductivity of a ZIF-8 thin-film, $0.326 \text{ Wm}^{-1}\text{K}^{-1}$. The applied force field with DDEC6 partial charge in the present study predicts the thermal conductivity of pristine (empty pores) ZIF-8 at 300 K and 1 atm as $0.206 \text{ Wm}^{-1}\text{K}^{-1}$ which is somewhat closer to the experimental value. For the thermal conductivity of ZIF-11, this is the first calculation to the best of my best knowledge. The thermal conductivity of pristine ZIF-11 at the standard 1 atm and 300 K is predicted as $0.123 \pm 0.004 \text{ Wm}^{-1}\text{K}^{-1}$ which is approximately half that of ZIF-8. The lower thermal conductivity of ZIF-11 could be problematic for transferring heat to and from the SAs inside their pores and become a barrier for practical thermal applications.

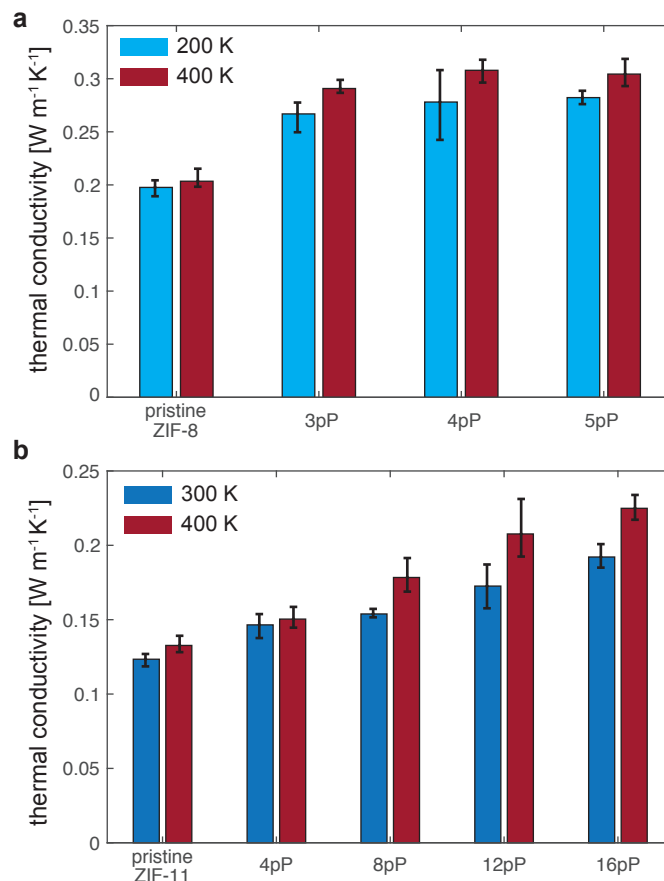


Figure 3-10. Thermal conductivity of pristine ZIFs and their composites with encapsulated erythritols. (a) ZIF-8 and its composites. (b) ZIF-11 and its composites. In each panel the cold and hot temperatures were chosen to ensure that the erythritol acts fully solid-like and liquid-like, respectively. Error bars show the maximum and minimum values from repeated calculations.

In order to investigate the influence of SA molecules on the thermal conductivity of the ZIFs, I calculate the thermal conductivities of composites by increasing the number of erythritol molecules in each pore. The results in Fig. 3-10 show that increasing the number of encapsulated erythritol molecules enhances the thermal conductivity for the both ZIF structures. This indicates that the erythritol molecules inside ZIF pores contribute to the heat transfer as additional parallel pathways. Note that fundamentally this increase was not a given, as the presence of additives in porous materials can positively or negatively affect the thermal conductivity of composites as new heat pathways or phonon scattering sources, respectively [96].

To elucidate further the thermal conductivity enhancement induced by the SA molecules,

I perform a phonon frequency analysis on ZIF structures with and without SA molecules [96,108]. The Fourier transform of the normalized HCACF, $\langle \vec{J}(0) \cdot \vec{J}(t) \rangle / \langle \vec{J}(0) \cdot \vec{J}(0) \rangle$, is used for the analysis as shown in Figs. 3-11a to 3-11c. The presence of SAs inside the ZIF pore does not disturb the major phonon frequency peaks of pristine ZIFs (compare the blue and red lines in Figs. 3-11a and b). Still, for both ZIFs the composite's peaks are stronger for frequencies around 40 THz, as seen in the insets. As seen in Fig. 3-11c this frequency range originates from the erythritol's major phonon frequency for the amorphous liquid state, as highlighted with orange color in Figs 3-11a to 3-11c.

The ZIF-8 composite shows an additionally enhanced peak at a very low-frequency range ($< \sim 2$ THz; blue shading in Fig. 3-11b inset), which has long lifetimes. To understand the origin of the phononic heat transfer of the very low-frequency range, the vibrational density of states (VDOS) is calculated by taking the Fourier transform the atomic velocity autocorrelation function (VACF) [109],

$$\text{VDOS}(\nu) = \int \gamma(t) \exp(-2\pi j\nu t) dt, \quad (3.6)$$

where ν is frequency, j is the imaginary number, and γ is the VACF which is defined as $\gamma(t) = \langle \sum_i v_i(0) \cdot v_i(t) \rangle / \langle \sum_i v_i(0) \cdot v_i(0) \rangle$. Figure 3-11d presents the VDOS for the atoms which are most important for energy transfer in ZIF-8 [108], namely Zn, N, and C1, as well as the VDOS for the edge atoms of erythritol, namely O, HO, and HC (details of labelling in Table 3-3). The O atoms in erythritol vibrate with the low-frequency phonon modes ($< \sim 2$ THz; blue shading in Fig. 3-11d) which overlap with the phonon modes of the main channel for energy transfer of ZIF-8 structure, Zn and C1. The 40 THz region phonon mode from erythritol is the major phonon mode of the edge hydrogen atoms (HO and HC, yellow shading) which closely interact with the ZIF ligands.

I also want to bring attention to the fact that the k of the liquid-like phase is larger than that of the solid-like phase, $k_{\text{liquid-like}} > k_{\text{solid-like}}$ seen in Fig. 3-10. This trend between solid-like vs. liquid-like erythritol is unusual compared to pure erythritol ($0.89 \pm 0.06 \text{ Wm}^{-1}\text{K}^{-1}$ at $20 \text{ }^\circ\text{C}$ solid and $0.33 \pm 0.02 \text{ Wm}^{-1}\text{K}^{-1}$ at $140 \text{ }^\circ\text{C}$ liquid) [100], and most natural materials, which have $k_{\text{liquid}} < k_{\text{solid}}$ [110]. To try to understand this unusual trend, I recall that Fig. 3-6 showed that the liquid-like SAs inside nanopores are more mobile than the solid-like SAs. At the atomistic scale within the framework structure, even at the highest SA loading conditions considered, there should be some vacant volume inside the pore which is not occupied by the SA molecules. Thus, a further heat transfer can be induced by the direct SA molecules transport or a thermocapillary mechanism within the mobile liquid-like phase.

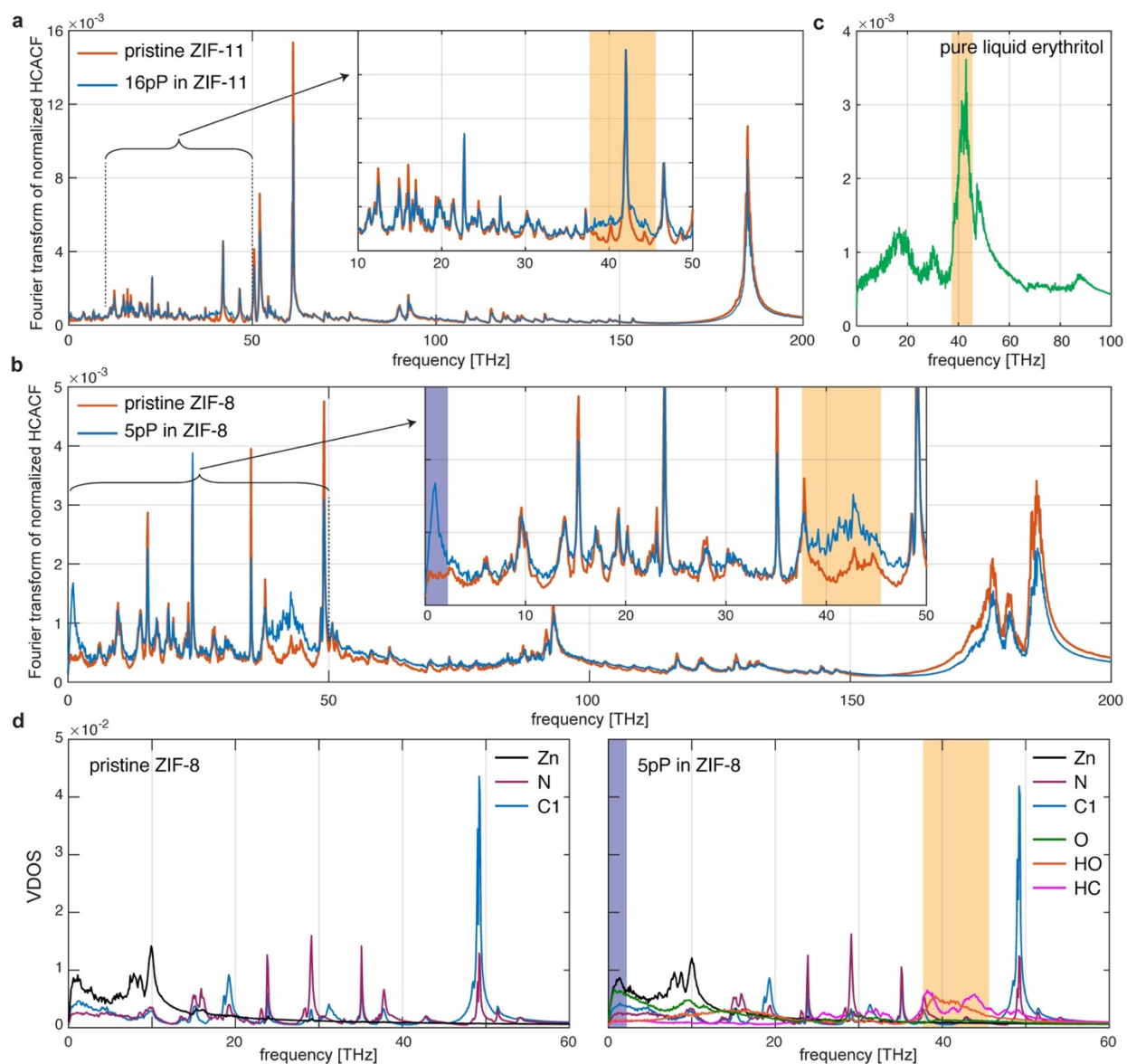


Figure 3-11. Phonon analysis by Fourier transform of the normalized HCACF and VACF at 400 K. (a) Comparison between pristine ZIF-11 and the case of 16pP in ZIF-11. The inset shows the 10-50 THz range in more detail. (b) Comparison between pristine ZIF-8 and the case of 5pP in ZIF-8. (c) Pure liquid erythritol. (d) VDOS comparison between pristine ZIF-8 (left) and the case of 5pP in ZIF-8 (right). Shaded bands indicate the enhanced heat transfer originating from the contributions of the edge atoms of erythritol, namely O (<2 THz, blue shading) and HO & HC (~40 THz, yellow shading).

Chapter 4

Thermal rectification via heterojunctions of solid-state phase change materials

Content in this chapter is adapted with permission from the following publication:

H. Kang, F. Yang, J. J. Urban, “Thermal Rectification via Heterojunctions of Solid-State Phase-Change Materials”, *Physical Review Applied* **10**, 024034, (2018)

4.1 Introduction

Inspired by the conceptual keystone of the microelectronics industry, the transistor, research on thermal transport with nonlinear thermal properties, such as nonlinear temperature- (or atomic mass, pressure, geometry) dependent thermal conductivities, has attracted a great deal of attention in recent years. Thermal devices including thermal rectifiers [111-125] and thermal transistors [111,112] have been realized by nonlinear transport phenomena such as thermal rectification (i.e. heat transport characterized by a preferential direction for heat flow, as described in Fig. 4-1). To achieve thermal rectification, several mechanisms at solid states have been suggested, such as enhancing lattice anharmonicity [112,126], use of asymmetric nanostructures [114-119], defects in structures [120,121] and asymmetric scattering of photons [122-124]. However, none of these proposed mechanisms has yielded materials with large thermal rectification, experimentally and analytically. Another promising mechanism, solid-state junctions using phase change materials, have been recently used for thermal rectification [127-130] and show great potential for making devices that scale effectively. *Cottrill et. al.* [131] analyzed the thermal rectification in a single phase change material. However, they limited their analysis to the simplest case with only one phase change material and thus can only provide rectification defined by the contrast of the high and low thermal conductivity phase of that individual material. The parametric study to obtain the thermal rectification remained in numerical approach, without an empirical solution for the maximal performance. Recently, they extended the approach to a junction with two phase change materials, however, considered limited cases which can make only one phase change situation at one time [132]. *Ordonez-Miranda et. al.* [133] studied an added hysteresis effect of a phase change material in the junction and figured out the main key parameter for the thermal rectification is thermal conductivity contrast of the phase change material. In addition, due to the lack of choice of appropriate materials, the thermal bias spans a very broad range (>50 K), limiting its use in applications such as thermal energy storage and thermal circuits,

which usually operate in a narrow thermal bias. The thermal rectification effect occurring in a narrow temperature window results in a greater potential to enhance when the thermal bias increases.

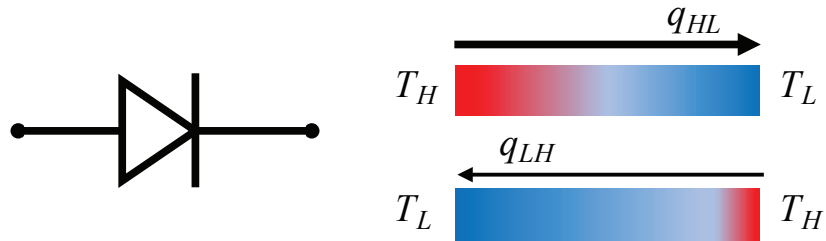


Figure 4-1. Basic concept of thermal rectification. Analogous to the electrical diode, the thermal rectifier transmits heat more easily in one direction than in the reverse direction. The subscript HL and LH indicate the direction of heat flux, from high (H) to low (L) temperature, or vice versa.

4.2 Problem statement

In this chapter, I propose a general theory that can handle multiple phase change materials and interfaces, thus providing large thermal rectification ratios well-beyond that provided by the mere thermal conductivity contrast of any one individual material. Specifically, heterojunctions using two phase change materials can strongly enhance the thermal rectification with the advantage of additional interfaces, as depicted in Fig. 4-2. This work encompasses a full physical picture of heat transport in phase change materials, fundamentally addressing all possible experimentally observable scenarios of thermal rectification. Then, this study applies the general theory to real rapid jump thermal conductivity materials. With recent advancements in solid-state materials, phase transitions can occur over just a few degrees in temperature. One prominent example is the metal-insulator-transition (MIT) which occurs in tungsten doped vanadium dioxide (VO_2) [134]. It has a MIT phase change in a very small temperature window (~ 5 K) which can show a thermal conductivity contrast clearly, and a higher thermal conductivity when the temperature rises across the MIT temperature. Thus, combining it with another material with the opposite temperature dependence, thermal rectification can be enhanced. Finally, the general theory suggests the theoretical maximum of thermal rectification factor of the solid-state junctions.

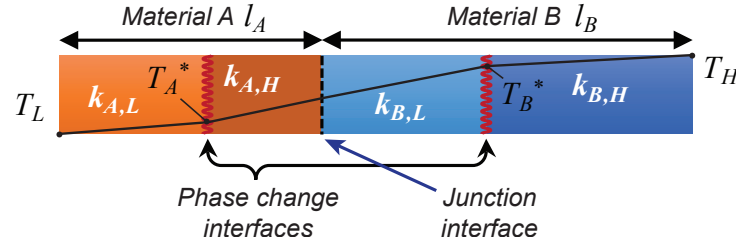


Figure 4-2. Heterojunction using two phase change materials in series. Schematic geometry of the suggested junction. The black line represents the temperature profile within the structure when phase changes exist in both A and B materials.

4.3 Theoretical model

4.3.1 Heterojunction design

I start with a junction formed by two materials, A and B, each possessing a phase change at temperatures T_A^* and T_B^* , respectively. For bulk or thin film samples, I assume heat transfer is a one-dimensional problem. Without losing generality, I take the case where material “B” has a higher phase change temperature than material “A” (i.e. $T_A^* < T_B^*$). I also assume that A has a thermal conductivity, $k_{A,L}$, at low temperature and a thermal conductivity, $k_{A,H}$, at high temperature. Here, the subscripts denote the material index and temperature region in relation to its phase change temperature (higher or lower), respectively. I also apply analogous nomenclature to material B. For simplicity, I assume thermal conductivity is a step function with respect to temperature through the phase change. This step function assumption is supported by the acceptable similarity of thermal conductivity trend in several materials within a large temperature range [134,135]. The schematic in Fig. 4-2 represents the geometry of the junction in materials A and B of lengths l_A and l_B , respectively. I name the heat flux traveling in the direction depicted in Fig. 4-2 as q_{LH} and the heat flux traveling in the opposite direction as q_{HL} . I treat the heat flux directions separately, meaning q_{LH} and q_{HL} represent their absolute magnitude. With heat flux in both directions, I define the thermal rectification factor as the normalized heat flux difference,

$$\gamma = \frac{\max\{q_{LH}, q_{HL}\}}{\min\{q_{LH}, q_{HL}\}} - 1. \quad (4.1)$$

In general, linear thermal transport, especially, no thermal rectification, the thermal rectification factor should be the minimum value, zero. The designed heterojunction would have a thermal rectification factor trend depending on thermal bias with an optimum.

4.3.2 General theory

The governing equation for this study is Fourier's law under steady state conditions. I assume that the thermal boundary resistance at the junction is negligible. The ratio of thermal boundary resistance to the thermal resistance of materials can affect the thermal rectification factor [132]. The eligible device length depends on the thermal conductivity of the applied materials and the contact resistance at the interface between different materials. This assumption holds if the device length is on the order of 300 nm or longer, since the most of similar thermal contact conductance at interface between different materials is on the order of $100 \text{ MWm}^{-2}\text{K}^{-1}$ [136-138] and the minimum order of that is around $30 \text{ MWm}^{-2}\text{K}^{-1}$ [139-142]. The boundary conditions are the temperatures T_H and T_L and the known phase change temperatures T_A^* and T_B^* . Heat fluxes through each material or phase are described by:

$$-q = k_{A,L} \left. \frac{\partial T}{\partial x} \right|_{T < T_A^*} = k_{A,H} \left. \frac{\partial T}{\partial x} \right|_{T > T_A^*} = k_{B,L} \left. \frac{\partial T}{\partial x} \right|_{T < T_B^*} = k_{B,H} \left. \frac{\partial T}{\partial x} \right|_{T > T_B^*}. \quad (4.2)$$

The problem I consider here is a general case with two phase change materials. When the thermal bias, $T_H - T_L$, changes, the phase change interface in the materials moves. There are a multitude of different factors that must be taken into consideration, such as the phase change could happen in A and/or B, or the flux direction yields different amounts of heat flux. In this study, I analytically derive the heat flux for all cases and the criteria to determine an appropriate case, compute the thermal rectification factor, γ , and give suggestions for designing an optimal thermal rectifier.

Firstly, I start from conditions that the phase change temperatures for both materials are between T_L and T_H (i.e. $T_L \leq T_A^* \leq T_H$ and $T_L \leq T_B^* \leq T_H$). Given these conditions, there are four possible cases of heat flux for the q_{LH} direction with respect to the interface position of the phase change: a phase change occurs only in material A or B, or in both or none of the materials, as summarized in Table 4-1. On the other hand, all these cases are possible for the q_{HL} direction except for the case of phase changes in both material A and B due to the temperature inequality order, as summarized in Table 4-2. Through multiple steps to simultaneously solve Eq. (4.2) for Fourier's law, I can firstly derive a relation of the phase change position in a certain material, and then obtain the magnitude of steady heat flux sequentially. The process to the general solutions is depicted below.

Table 4-1. Total possible phase change cases with respect to the inequalities between the phase change temperatures and boundary temperatures for the q_{LH} direction.

T_L	Material A	T_i	Material B	T_H	# of phase change
T_A^*, T_B^*	$k_{A,H}$		$k_{B,H}$		0
T_A^*	$T_B^*, k_{A,H}$		$k_{B,H}$		0
T_A^*	$k_{A,H}$	$k_{B,L}$	T_B^*	$k_{B,H}$	1
T_A^*	$k_{A,H}$		$k_{B,L}$	T_B^*	0
$k_{A,L}$	T_A^*, T_B^*	$k_{A,H}$	$k_{B,H}$		1
$k_{A,L}$	T_A^*	$k_{A,H}$	T_B^*	$k_{B,H}$	2
$k_{A,L}$	T_A^*	$k_{A,H}$	$k_{B,L}$	T_B^*	1
	$k_{A,L}$	$k_{B,L}$	T_A^*, T_B^*	$k_{B,H}$	1
	$k_{A,L}$		$T_A^*, k_{B,L}$	T_B^*	0
	$k_{A,L}$		$k_{B,L}$	T_A^*, T_B^*	0

Table 4-2. Total possible phase change cases with respect to the inequalities between the phase change temperatures and boundary temperatures for the q_{HL} direction.

T_L	Material A	T_i	Material B	T_H	# of phase change
T_B^*, T_A^*	$k_{A,L}$		$k_{B,L}$		0
T_B^*	$k_{A,H}$	$k_{A,L}$	$k_{B,L}$		1
T_B^*	$k_{A,H}$		$T_A^*, k_{B,L}$		0
T_B^*	$k_{A,H}$		$k_{B,L}$	T_A^*	0
$k_{A,H}$	T_B^*, T_A^*	$k_{A,L}$	$k_{B,L}$		1
	$T_B^*, k_{A,H}$		$T_A^*, k_{B,L}$		0
	$T_B^*, k_{A,H}$		$k_{B,L}$	T_A^*	0
	$k_{A,H}$	$k_{B,H}$	T_B^*, T_A^*	$k_{B,L}$	1
	$k_{A,H}$	$k_{B,H}$	T_B^*	$k_{B,L}$	1
	$k_{A,H}$		$k_{B,H}$	T_B^*, T_A^*	0

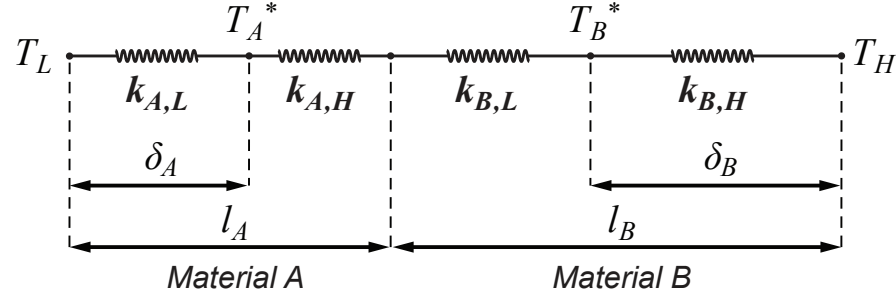


Figure 4-3. Thermal resistance circuit diagram for the heterojunction design comprised of two phase-change materials.

For the q_{LH} direction with the case of that phase change occurs in both materials, I start from two heat flux equations attained from the thermal circuit diagram in Fig. 4-3.

$$q = \frac{T_A^* - T_L}{\delta_A / k_{A,L}} = \frac{T_H - T_A^*}{(l_A - \delta_A) / k_{A,H} + (l_B - \delta_B) / k_{B,L} + \delta_B / k_{B,H}}. \quad (4.3)$$

$$q = \frac{T_B^* - T_L}{\delta_A / k_{A,L} + (l_A - \delta_A) / k_{A,H} + (l_B - \delta_B) / k_{B,L}} = \frac{T_H - T_B^*}{\delta_B / k_{B,H}}. \quad (4.4)$$

The two heat flux equations are rearranged in terms of δ_A and δ_B .

$$\left(\frac{T_H - T_A^*}{k_{A,L}} + \frac{T_A^* - T_L}{k_{A,H}} \right) \delta_A = (T_A^* - T_L) \left(\frac{1}{k_{B,H}} - \frac{1}{k_{B,L}} \right) \delta_B + (T_A^* - T_L) \left(\frac{l_A}{k_{A,H}} + \frac{l_B}{k_{B,L}} \right). \quad (4.5)$$

$$(T_H - T_B^*) \left(\frac{1}{k_{A,L}} - \frac{1}{k_{A,H}} \right) \delta_A = \left(\frac{T_B^* - T_L}{k_{B,H}} + \frac{T_H - T_B^*}{k_{B,L}} \right) \delta_B - (T_H - T_B^*) \left(\frac{l_A}{k_{A,H}} + \frac{l_B}{k_{B,L}} \right). \quad (4.6)$$

I eliminate the terms of δ_A by combining the equations.

$$\begin{aligned} & \left(\frac{T_H - T_A^*}{k_{A,L}} + \frac{T_A^* - T_L}{k_{A,H}} \right) \left\{ \left(\frac{T_B^* - T_L}{k_{B,H}} + \frac{T_H - T_B^*}{k_{B,L}} \right) \delta_B - (T_H - T_B^*) \left(\frac{l_A}{k_{A,H}} + \frac{l_B}{k_{B,L}} \right) \right\} \\ & = (T_A^* - T_L)(T_H - T_B^*) \left(\frac{1}{k_{A,L}} - \frac{1}{k_{A,H}} \right) \left\{ \left(\frac{1}{k_{B,H}} - \frac{1}{k_{B,L}} \right) \delta_B + \left(\frac{l_A}{k_{A,H}} + \frac{l_B}{k_{B,L}} \right) \right\}. \end{aligned} \quad (4.7)$$

The equation is rearranged as in terms of δ_B .

$$\begin{aligned} & \delta_B \left\{ \left(\frac{T_H - T_A^*}{k_{A,L}} + \frac{T_A^* - T_L}{k_{A,H}} \right) \left(\frac{T_B^* - T_L}{k_{B,H}} + \frac{T_H - T_B^*}{k_{B,L}} \right) - (T_A^* - T_L)(T_H - T_B^*) \left(\frac{1}{k_{A,L}} - \frac{1}{k_{A,H}} \right) \left(\frac{1}{k_{B,H}} - \frac{1}{k_{B,L}} \right) \right\} \\ & = \left\{ (T_A^* - T_L) \left(\frac{1}{k_{A,L}} - \frac{1}{k_{A,H}} \right) + \left(\frac{T_H - T_A^*}{k_{A,L}} + \frac{T_A^* - T_L}{k_{A,H}} \right) \right\} \left(\frac{l_A}{k_{A,H}} + \frac{l_B}{k_{B,L}} \right) (T_H - T_B^*). \end{aligned} \quad (4.8)$$

I remove the fractions by multiplying both sides by $k_{A,L} k_{A,H} k_{B,L} k_{B,H}$.

$$\begin{aligned} & \delta_B \left[\{k_{A,H}(T_H - T_A^*) + k_{A,L}(T_A^* - T_L)\} \{k_{B,H}(T_H - T_B^*) + k_{B,L}(T_B^* - T_L)\} - (T_A^* - T_L)(T_H - T_B^*)(k_{A,H} - k_{A,L})(k_{B,L} - k_{B,H}) \right] \\ & = k_{B,L} k_{B,H} \left[(T_A^* - T_L)(k_{A,H} - k_{A,L}) + \{k_{A,H}(T_H - T_A^*) + k_{A,L}(T_A^* - T_L)\} \right] \left(\frac{l_A}{k_{A,H}} + \frac{l_B}{k_{B,L}} \right) (T_H - T_B^*) \end{aligned}$$

$$= \mathbf{k_{B,H}}(T_H - T_L)(k_{A,H}l_B + k_{B,L}l_A)(T_H - T_B^*). \quad (4.9)$$

The bold terms in Eq. (4.9) are replaced by a heat flux term, q , through the equation of

$$q = \frac{T_H - T_B^*}{\delta_B / k_{B,H}}. \quad (4.10)$$

Then, I can obtain the general heat flux relation for the case of that a phase change occurs in both materials as below.

$$q = \frac{\{k_{A,H}(T_H - T_A^*) + k_{A,L}(T_A^* - T_L)\}\{k_{B,H}(T_H - T_B^*) + k_{B,L}(T_B^* - T_L)\} - (k_{A,H} - k_{A,L})(k_{B,L} - k_{B,H})(T_A^* - T_L)(T_H - T_B^*)}{(T_H - T_L)(k_{A,H}l_B + k_{B,L}l_A)}. \quad (4.11)$$

If a phase change occurs only in material A or B, the other material without a phase change possesses a constant overall thermal conductivity. For the case of a phase change only in A with $T_L \leq T_B^* \leq T_H$ condition, $k_{A,H}$ is substituted by $k_{A,L}$ then the above relation with two phase changes can be simplified as

$$q = \frac{k_{A,L}\{k_{B,H}(T_H - T_B^*) + k_{B,L}(T_B^* - T_L)\}}{k_{A,L}l_B + k_{B,L}l_A}. \quad (4.12)$$

Similarly, the relation for the case of a phase change in only in B with $T_L \leq T_A^* \leq T_H$ condition is obtained by substituting $k_{B,H}$ for $k_{B,L}$.

$$q = \frac{k_{B,H}\{k_{A,H}(T_H - T_A^*) + k_{A,L}(T_A^* - T_L)\}}{k_{A,H}l_B + k_{B,H}l_A} \quad (4.13)$$

Eqs. (4.12) and (4.13) can be reduced again to derive the relation for the case of none phase change in neither material.

$$q = \frac{k_{A,L}k_{B,H}(T_H - T_L)}{k_{A,H}l_B + k_{B,H}l_A} \quad (4.14)$$

Likewise, the heat flux relations for the q_{HL} direction can be derived by following the same process above with the total case study in Table 4-2. The general solutions to all cases on both directions are summarized in Tables 4-3 and 4-4. The adjustment methods for the extended conditions will be discussed.

Table 4-3. Heat flux relations for q_{LH} with corresponding criteria. The criteria on columns and rows independently determine the existence of phase change in material A and B, respectively.

$q_{LH} =$	Phase change in A: $1/\theta_A > R_{LH,A}$	No phase change in A: $1/\theta_A \leq R_{LH,A}$
Phase change in B: $\theta_B > R_{LH,B}$	$\frac{\{k_{A,H}(T_H - T_A^*) + k_{A,L}(T_A^* - T_L)\} \{k_{B,H}(T_H - T_B^*) + k_{B,L}(T_B^* - T_L)\} + (k_{A,H} - k_{A,L})(k_{B,H} - k_{B,L})(T_H - T_B^*)(T_A^* - T_L)}{(T_H - T_L)(k_{A,H}l_B + k_{B,L}l_A)}$	$\frac{k_{A,L} \{k_{B,H}(T_H - T_B^*) + k_{B,L}(T_B^* - T_L)\}}{k_{A,L}l_B + k_{B,L}l_A}$
No phase change in B: $\theta_B \leq R_{LH,B}$	$\frac{k_{B,H} \{k_{A,H}(T_H - T_A^*) + k_{A,L}(T_A^* - T_L)\}}{k_{A,H}l_B + k_{B,H}l_A}$	$\frac{k_{A,L}k_{B,H}(T_H - T_L)}{k_{A,L}l_B + k_{B,H}l_A}$

Table 4-4. Heat flux relations for q_{HL} with corresponding criteria. The relation on the second column is about the state of the absence of phase change in both materials.

	Phase change in A: $R_{HL} < \theta_A$	No change: $\theta_A \leq R_{HL} \leq \theta_B \dagger$	Phase change in B: $\theta_B \dagger < R_{HL}$
$q_{HL} =$	$\frac{k_{B,L} \{k_{A,H}(T_H - T_A^*) + k_{A,L}(T_A^* - T_L)\}}{k_{A,L}l_B + k_{B,L}l_A}$	$\frac{k_{A,H}k_{B,L}(T_H - T_L)}{k_{A,H}l_B + k_{B,L}l_A}$	$\frac{k_{A,H} \{k_{B,H}(T_H - T_B^*) + k_{B,L}(T_B^* - T_L)\}}{k_{A,H}l_B + k_{B,H}l_A}$

\dagger when $\theta_B < 0$, there is no phase change in both materials. It is equivalent to assume θ_B as very large number

4.3.2 Criteria to determine phase situations

The criterion parameters are important since they are related to how many phase changes occur and in which material. Thus, they determine which heat flux relation for q_{LH} in Table 4-3 or for q_{HL} in Table 4-4 is appropriate. These criterion parameters are defined by both boundary temperatures (T_H and T_L) and thermophysical properties of A and B. The following dimensionless temperatures

$$\theta_A = \frac{T_A^* - T_L}{T_H - T_A^*} \quad \text{and} \quad \theta_B = \frac{T_B^* - T_L}{T_H - T_B^*} \quad (4.15)$$

are introduced as representative parameters for thermal condition effects on judging the cases. The criterion for each direction is separately proposed since the possible number of phase changes is different. There are two criterion relations for each material for the q_{LH} direction. In order for a phase change to occur in material A, the temperature at the junction point between materials A and B, T_i , should be larger than the phase change temperature T_A^* .

$$\frac{T_A^* - T_L}{l_A/k_{A,L}} < \frac{T_H - T_A^*}{(l_B - \delta_B)/k_{B,L} + \delta_B/k_{B,H}}. \quad (4.16a)$$

$$\frac{k_{A,L}}{l_A} (T_A^* - T_L) < \frac{T_H - T_A^*}{\left(1/k_{B,H} - 1/k_{B,L}\right)\delta_B + l_B/k_{B,L}} = \frac{k_{B,L}k_{B,H}(T_H - T_A^*)}{(k_{B,L} - k_{B,H})\delta_B + l_Bk_{B,H}}. \quad (4.16b)$$

To express the criteria with the design and operating parameters, δ_B is also presented and replaced by the parameters from the heat flux relations.

$$\delta_B = \frac{k_{B,H}(T_H - T_B^*)}{q} = \frac{k_{B,H}(T_H - T_B^*)(k_{A,L}l_B + k_{B,L}l_A)}{k_{A,L}\{k_{B,H}(T_H - T_B^*) + k_{B,L}(T_B^* - T_L)\}}. \quad (4.17)$$

Starting from the inequality condition (4.16), I can obtain a relation of $1/\theta_A > R_{LH,A}$.

$$\frac{T_H - T_A^*}{T_A^* - T_L} > \frac{(1 - k_{B,H}/k_{B,L})(k_{A,L}l_B + k_{B,L}l_A)}{l_A \left\{ k_{B,H} + k_{B,L} \left(\frac{T_B^* - T_L}{T_H - T_B^*} \right) \right\}} + \frac{k_{A,L}l_B}{k_{B,L}l_A}. \quad (4.18a)$$

$$1/\theta_A > \frac{(1 - k_{B,H}/k_{B,L})(k_{A,L}l_B + k_{B,L}l_A)}{l_A(k_{B,H} + k_{B,L}\theta_B)} + \frac{k_{A,L}l_B}{k_{B,L}l_A} = R_{LH,A}. \quad (4.18b)$$

Similarly, the derivation for the material B starts from a physical condition between T_b^* and junction temperature, and δ_A expression.

$$\frac{T_B^* - T_L}{\delta_A/k_{A,L} + (l_A - \delta_A)/k_{A,H}} > \frac{T_H - T_B^*}{l_B/k_{B,H}}. \quad (4.19)$$

$$\delta_A = \frac{k_{A,L}(T_H - T_A^*)}{q} = \frac{k_{A,L}(T_H - T_A^*)(k_{A,H}l_B + k_{B,H}l_A)}{k_{B,H}\{k_{A,H}(T_H - T_A^*) + k_{A,L}(T_A^* - T_L)\}}. \quad (4.20)$$

Then, the relation detailing the existence of material B is obtained as $\theta_B > R_{LH,B}$.

$$\frac{T_B^* - T_L}{T_H - T_B^*} > \frac{(1 - k_{A,L}/k_{A,H})(k_{A,H}l_B + k_{B,H}l_A)}{l_B \left\{ k_{A,L} + k_{A,H} \left(\frac{T_H - T_A^*}{T_A^* - T_L} \right) \right\}} + \frac{k_{B,H} l_A}{k_{A,H} l_B}. \quad (4.21a)$$

$$\theta_B > \frac{(1 - k_{A,L}/k_{A,H})(k_{A,H}l_B + k_{B,H}l_A)}{l_B(k_{A,L} + k_{A,H}/\theta_A)} + \frac{k_{B,H} l_A}{k_{A,H} l_B} = R_{LH,B}. \quad (4.21b)$$

The two criteria for q_{LH} independently determine the existence of phase change in material A and B, as summarized in Table 4-3.

In the q_{HL} direction, one phase change can occur at most. From the same comparison using the inequality conditions below, a criterion R_{HL} is found to be sufficient for determining whether the phase change for both materials exists or not. The detailed inequality criteria with a dimensionless ratio, R_{HL} , are summarized in Table 4-4.

$$\text{For A,} \quad \frac{k_{A,H}}{l_A} (T_H - T_A^*) < \frac{k_{B,L}}{l_B} (T_A^* - T_L). \quad (4.22)$$

$$\text{For B,} \quad \frac{k_{A,H}}{l_A} (T_H - T_B^*) > \frac{k_{B,L}}{l_B} (T_B^* - T_L). \quad (4.23)$$

$$R_{HL} = \frac{k_{A,H} l_B}{k_{B,L} l_A}. \quad (4.24)$$

4.3.4 Adjustment method for extended conditions

The above criteria and the general solutions in Tables 4-3 and 4-4 are valid only when the phase change temperatures are within boundaries $T_L \leq T_A^* \leq T_H$ and $T_L \leq T_B^* \leq T_H$. If T_A^* or T_B^* is outside these ranges, no phase change should arise. Should this be the case, the material can be assumed to possess a constant overall thermal conductivity. To adjust the situations with correct properties, I have to substitute $k_{A,H}$ for $k_{A,L}$ and/or $k_{B,L}$ for $k_{B,H}$ to the relations and criteria for the q_{LH} in Table 4-3 when $T_A^* < T_L$ and/or $T_B^* > T_H$, respectively. Likewise, when $T_A^* > T_H$ and/or $T_B^* < T_L$, the values of $k_{A,L}$ and/or $k_{B,H}$ for the q_{HL} are substituted for $k_{A,H}$ and/or $k_{B,L}$ in Table 4-4, respectively. Another adjustment for the q_{HL} is additionally needed since R_{HL} is a single criterion for both materials, and mentioned in Table 4-4. On the boundary of criteria, the solutions to the heat flux of both sides should be physically continuous and the continuity was validated.

4.4 Case study

4.4.1 Applied materials

Based on this general theory, I introduce a candidate material pair to show the potential thermal rectification effect of phase change heterojunctions. At room temperature or above, where most thermal diodes are used, low temperature thermal conductivities in the solid-state phase are higher than the high temperature thermal conductivities, such as polyethylene [135] (material A in the model). To maximize thermal rectification of the heterojunction, choosing a material with the opposite temperature trend can be a promising design for the other side. One candidate is metallic VO_2 (material B in the model) [134]. Indeed, the materials have the thermal conductivities like a step function [134,135], and have been used in literature [131]. The narrow transition temperature range hardly degrades the thermal rectification factor as enough thermal bias is applied [132]. The phase change temperatures and amplitude of thermal conductivity for both materials are tunable, either by doping [134], geometric factor [135], or stress [135]. For this work, I used the thermal conductivity data of the polyethylene by large-scale molecular dynamics simulations and the metallic VO_2 [134] by experimental measurements on a suspended device. Both temperature-dependent thermal conductivities show that the shapes are good approximation of step functions even at the length scale of <100 nm. Even though VO_2 exhibits a hysteresis effect in heating and cooling processes, the general theory can cover the both heat flux based on different properties from the hysteresis. Since my theory here is general and I wish to test an example with more varieties of phase change states, I assume VO_2 has a higher value of virtual representative phase change temperature as $T_B^*=340$ K than the polyethylene with $T_A^*=320$ K. Otherwise, I do not optimize other material properties (such as thermal conductivity ratio across phase change

temperature) to achieve best performance instead I keep them the same as literature values [134,135], as summarized in Table 4-5.

Table 4-5. Material properties used for the calculation in this manuscript for polyethylene (material A) [135] and tungsten doped VO₂ (material B) [134].

T_A^* [K]	T_B^* [K]	$k_{A,L}$ [Wm ⁻¹ K ⁻¹]	$k_{A,H}$ [Wm ⁻¹ K ⁻¹]	$k_{B,L}$ [Wm ⁻¹ K ⁻¹]	$k_{B,H}$ [Wm ⁻¹ K ⁻¹]	l_A/l_B [-]
320	340 [†]	30	10	2	4	4

[†] The value of T_B^* is virtual

4.4.2 General theory results

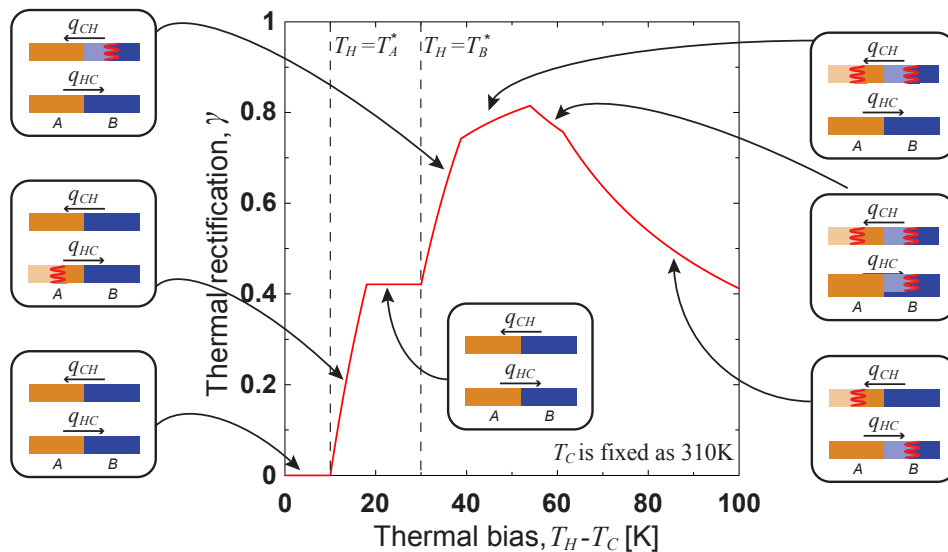


Figure 4-4. Thermal bias dependent thermal rectification via a heterojunction between polyethylene (material A) [135] and tungsten doped VO₂ (material B) [134] as detailed in Table 4-5. Regimes with different slopes represent different combinations of phase change states between the two materials. Two representative states yielding different thermal rectification trends are detailed in the inserts.

Figure 4-4 shows the thermal rectification factor dependent on thermal bias. The interface positions of phase change in both materials move with respect to the change of temperature T_H , as

the temperature T_L at the other end is fixed. The moving phase change interfaces in both materials are responsible for the various cases of thermal rectification. In the given conditions, seven distinct regions with different slopes of the thermal rectification factor are observed. All of which are derived from different phase change states. Two representative states, yielding different thermal rectification trends, are described as schematics in the insets. The thermal bias determines the phase changes, and thus defines the overall thermal conductivity and heat flux in each state and direction. The changing overall thermal conductivities are the underlying phenomenology behind thermal rectification.

At the flat regions in Fig. 4-4, I note that there is no phase change in either direction or material. The junction with two materials possessing the thermally opposite phase change trends is expected to perform high thermal rectification. In this case, the solid-state junction using the phase change materials shows a maximal thermal rectification factor of 80 %, with a great potential to achieve a higher thermal rectification compared to the concept with an asymmetric shape of a material such as the 7 % of a carbon nanotube [116] and 28 % of VO_2 [118]. Furthermore, as the concept developed in this work is based on bulk properties, the solid-state thermal device can be scaled up significantly more easily in comparison to nanostructures in the literature.

The general theory presented above offers a physical interpretation of thermal rectification, thus directly examining the contribution of each parameter to the thermal rectification factor and the relationship among these parameters. As investigating to optimize the thermal rectification factor according to geometric characteristics, I can recognize the thermal rectification of the junction depends on the length ratio l_A/l_B of the materials, not on the length itself. As shown in Fig. 4-5 which presents the thermal rectification factor obtained by the length ratio and thermal bias, the length ratio l_A/l_B , as a design parameter, is a critical parameter to determine the trend of thermal rectification factor, as well as its maximal value. Furthermore, under particular conditions such as the black line of $l_A/l_B = 2^3$, I can observe more than one local maximum. The result with plural optimization points represents that the solid-state junction is dominated by the complex phase change scenarios and this general theory is able to provide a design guide for thermal devices from testable predictions.

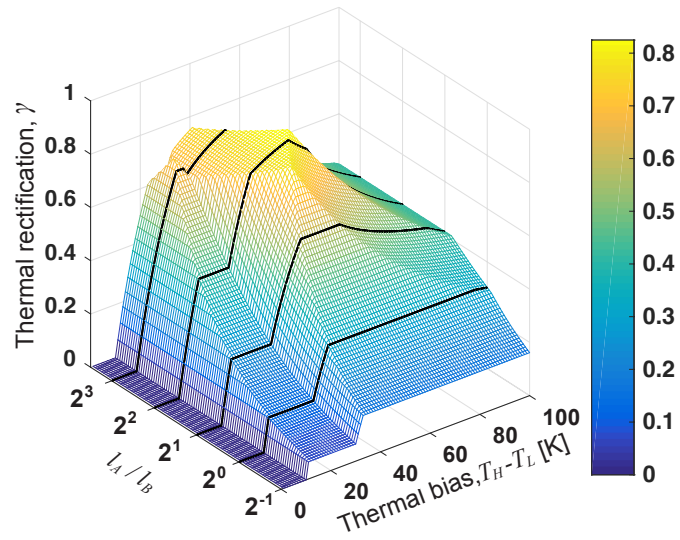


Figure 4-5. Optimal thermal rectification with respect to a selected design parameter, the length ratio l_A/l_B . The 3D mesh graph shows the existence of local and general optimization points for thermal rectification. (Other parameters are detailed in Table 4-5)

4.4.3 Global optimal solution

This general theory works as a powerful and convenient tool to understand the physics of different cases of phase change in the heterojunction and the theoretical limitations on the performance of such a thermal diode. The general theory shows that the phase change temperature as well as the length ratio are two knobs to tune the thermal rectification factor. In order to examine the maximum potential rectification behavior possible across the heterojunction, I study the effect that changing the phase change temperature in each material has. In the following analysis, $T_{VO_2}^*$ is considered as a tuning parameter while $T_{Polyethylene}^*$ is fixed as 320 K and the generality of $T_A^* < T_B^*$ should be kept by choosing VO_2 as material A at the cases of $T_{VO_2}^* < T_{Polyethylene}^*$. Figure 4-6 presents the dependence of the thermal rectification factor with respect to $T_{VO_2}^*$ for three different length ratios. The black dashed line in Fig. 4-6 refers to the condition where VO_2 has the same phase change temperature as polyethylene (i.e. 320 K). Two noticeable features emerge from this analysis, which I discuss below.

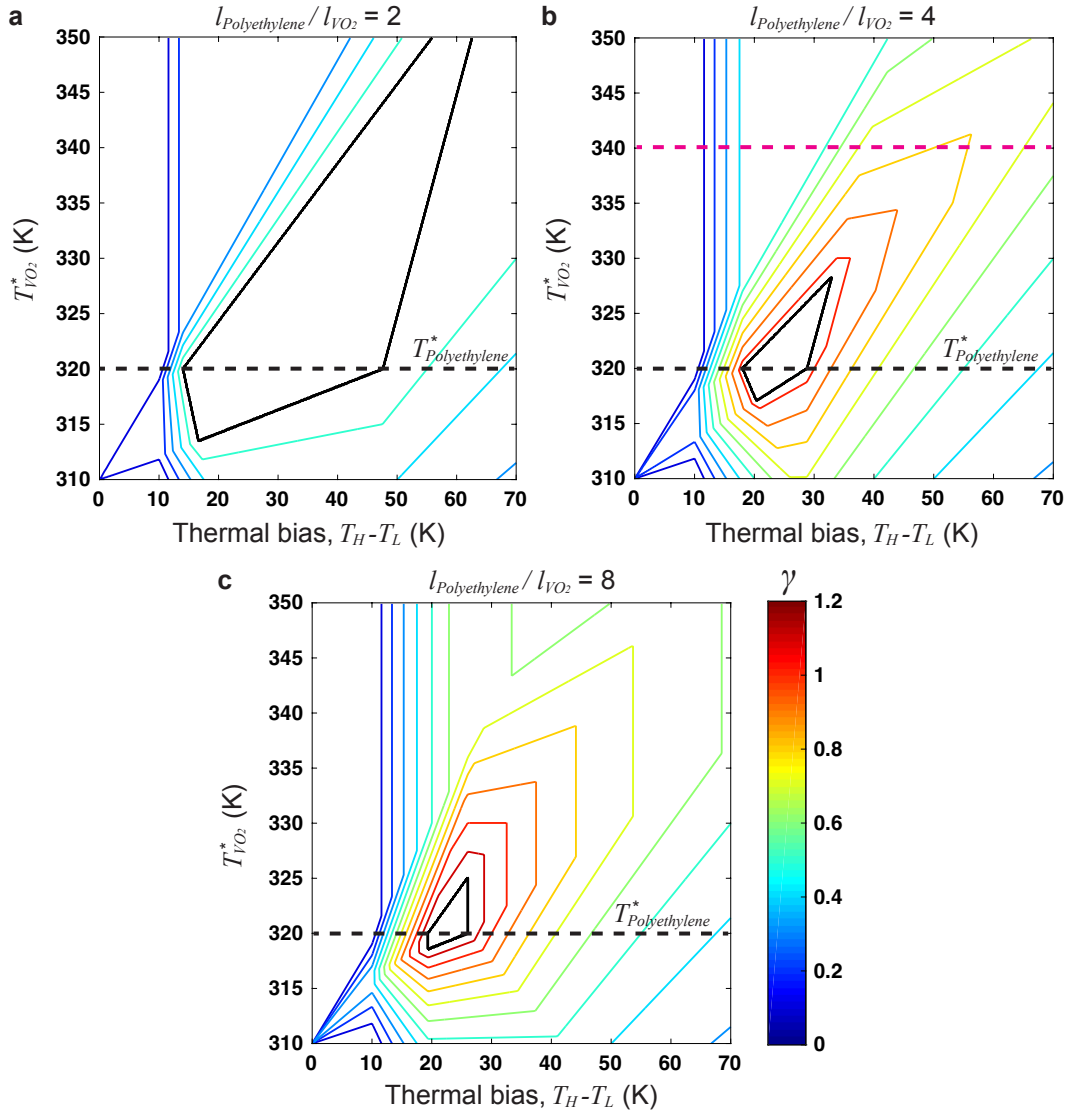


Figure 4-6. Optimal thermal rectification with respect to phase change temperature at the defined length ratio, (a) $l_{VO_2}/l_{Polyethylene} = 2$, (b) $l_{VO_2}/l_{Polyethylene} = 4$ and (c) $l_{VO_2}/l_{Polyethylene} = 8$. The area inside the black line in each figure has the same thermal rectification factor γ and the maximum value of γ . The black dashed lines mean the condition the VO_2 has the same phase change temperature with the polyethylene as 320 K. The magenta dashed line in (b) corresponds to the condition of the case study at Fig. 4-4. (Other parameters are detailed in Table 4-5)

Feature one is that the optimal thermal rectification factor appears across a plateau region (and not at one particular point). The area inside the black solid line (the plateau region) has the same value of γ as a local maximum across the entire area. Basically, the highest possible γ

available from the heterojunction, occurs when both materials are in their most thermally conductive phase in one direction and in their lowest thermally conductive phase in the other direction. However, as a practical matter, this limiting case seldom occurs in real systems, so, in general, it is important to examine the case where the local maximum γ predominates – this is where only one material is exhibiting a phase change interface in both directions. In this circumstance, the plateau regions confirm that the thermal rectification maxima are robust to small thermal perturbations from the ideal case. In more detail, when I check the phase change states of the plateau regions, there is only one phase change in both heat flux directions in the same material (in the VO₂ material at the length ratio conditions of Figs. 4-6a and 4-6b, and in the polyethylene material at the condition of Fig. 4-6c).

I can derive the mathematical solution of γ for each region from the general theory summarized in Tables 4-3 and 4-4. When the phase change occurs only in material A (as is the case in Fig. 4-6c which has a large length ratio l_A/l_B), the heat flux of each direction can be calculated as

$$q_{LH} = \frac{k_{B,H} \{k_{A,H}(T_H - T_A^*) + k_{A,L}(T_A^* - T_L)\}}{k_{A,H}l_B + k_{B,H}l_A}, \quad (4.25)$$

$$q_{HL} = \frac{k_{B,L} \{k_{A,H}(T_H - T_A^*) + k_{A,L}(T_A^* - T_L)\}}{k_{A,L}l_B + k_{B,L}l_A}. \quad (4.26)$$

At conditions that cause higher heat flux in the q_{LH} direction, the solution of γ in the case of a phase change in material A in both directions can be derived by inserting Eqs. (4.25) and (4.26) into the Eq. (4.1) as follows.

$$\gamma = \left(\frac{k_{A,L}}{k_{B,L}} + \frac{l_A}{l_B} \right) \bigg/ \left(\frac{k_{A,H}}{k_{B,H}} + \frac{l_A}{l_B} \right) - 1. \quad (4.27)$$

Additionally, the solution of γ with a phase change in material B can be presented as

$$\gamma = \left(1 + \frac{k_{B,H}}{k_{A,H}} \frac{l_A}{l_B} \right) \bigg/ \left(1 + \frac{k_{B,L}}{k_{A,L}} \frac{l_A}{l_B} \right) - 1. \quad (4.28)$$

Both equations are possible solutions for maximum γ , expressed as an independent relation of the thermal bias (T_H and T_L) and the phase change temperatures (T_A^* and T_B^*). It means that the change in overall thermal conductivity for both directions is maintained at a certain rate according to the thermal bias, even though the phase change interface is moving. Thus, the optimal plateau regions, which share an identical thermal rectification factor, occur due to the independency of the thermal rectification on the axis variables, the thermal bias and T_{VO2}^* .

The second feature worth noting arises that the thermal bias range satisfying the local optimal γ is the widest when the phase change temperatures of the two materials are identical, i.e. at the condition on the black dashed line in Figure 4-6. As the phase change temperatures of two materials approach the same value, the possibility of the state with two phase changes in the q_{LH} direction disappears. The more phase change interface disturbs to actualize the higher thermal rectification from the appropriate thermally conductive phase for each heat flux direction. The state with only one phase change can utilize the proper phase of at least the other material which a phase change does not occur, in contrast to the state with two phase changes. The reduced possibility of the additional phase change widens the thermal bias condition for the local maximum γ .

By leveraging the tunability of the phase change temperature, a solid-state junction consisting of two materials with an identical phase change temperature is the most promising case. Below, I examine the theoretical maximum thermal rectification factor in this case. One additional optimization parameter for this solid-state heterojunction is the ratio of the lengths of each segment of material, l_A/l_B . Figure 4-7 shows the maximal thermal rectification factor γ_{max} of the heterojunction at each length ratio condition. The results of γ_{max} corresponds to the mathematical solutions from Eqs. (4.27) or (4.28), as expected from the above analysis. A global optimization value is obtainable from the intersection of the two equations. To achieve the global maximal performance of the heterojunction, the length ratio should satisfy the following relation of l_A/l_B .

$$l_A/l_B = \sqrt{\frac{k_{A,L} k_{A,H}}{k_{B,L} k_{B,H}}}. \quad (4.29)$$

Then, as the optimized length ratio inserts into Eqs. (4.27) or (4.28), the equations result in the identical thermal rectification factor of

$$\gamma_{max} = \sqrt{\frac{k_{A,L} k_{B,H}}{k_{A,H} k_{B,L}}} - 1. \quad (4.30)$$

The theoretical maximum solution is based on the geometric mean of the thermal conductivity ratio of the two materials. The relation with the thermal conductivity ratio is consistent with the initial intuition of selecting polyethylene as material A ($k_{A,L} > k_{A,H}$) and VO₂ ($k_{B,L} < k_{B,H}$) as material B to achieve an effect of thermal rectification in this case study. The maximum solution shows there is no limit ceiling for the thermal rectification in this design. A phase change material with one phase change temperature makes two separate phases. Thus, two materials in the junction design are sufficient number to realize the effect of thermal rectification. Additionally, I am able to check that the length ratio for the high thermal rectification is dependent on the ratio of the general thermal conductivity between two phase change materials.

Upon close inspection of this condition of the length ratio for the theoretical maximum, a plateau region according to thermal bias does not appear, in other words, the optimum γ_{max} is observed at a specific thermal bias condition. The phase change temperature is located at the junction interface in both directions. Without any phase change in both materials, the heterojunction can be operated only with low thermal conductivities of both materials in one direction and high thermal conductivities in the opposite direction. As presented in Fig. 4-7, the heterojunction with the two materials has a theoretical potential to present the γ_{max} of over 140 %. Although based on optimal phase change temperatures of materials and a specific thermal bias condition, the theoretical maximum value suggests the guidance for design and material selection, and clarifies the possibility of the heterojunction as a thermal rectifier with an outstanding thermal rectification factor.

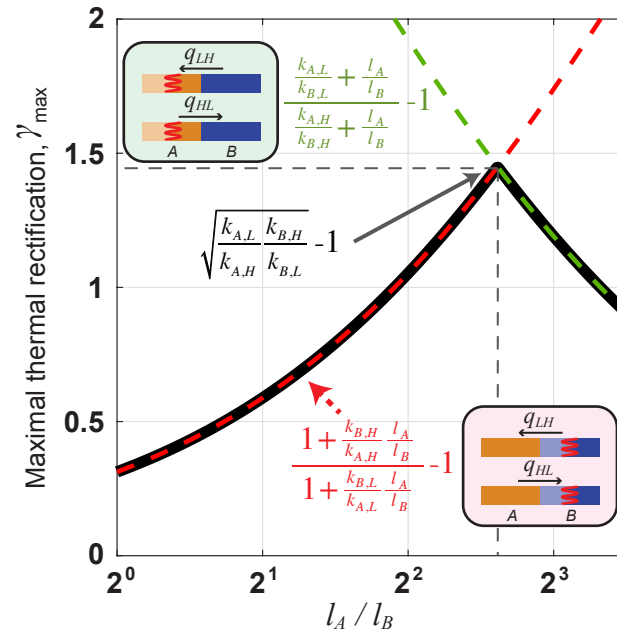


Figure 4-7. Maximal thermal rectification γ_{max} with $T_A^* = T_B^*$ condition at each length ratio. The green line is the solution of γ for the case of a phase change in material A in both directions and the red line is the solution for that in material B. The global maximal rectification is observed at the intersection between the two solutions. The theoretical maximal rectification is based on the geometric mean of the thermal conductivity ratio of the two materials as expressed as $\sqrt{\frac{k_{A,L} k_{B,H}}{k_{A,H} k_{B,L}}} - 1$

1 with the optimized length ratio of $\frac{l_A}{l_B} = \sqrt{\frac{k_{A,L} k_{A,H}}{k_{B,L} k_{B,H}}}$. (Other parameters are detailed in Table 4-5)

Chapter 5

Summary and future works

5.1 Summary of this dissertation

This dissertation has made contributions to the understanding of anomalous phases for thermal energy materials and their second-order phase transitions; and suggested a theoretical model of a nonlinear transport phenomenon, thermal rectification, by using phase change materials. Here I summarize the content of this dissertation.

Chapter 2 presented a molecular insight into the lower critical solution temperature (LCST) transition of aqueous ionic liquids. Thermally responsive ionic liquids are promising draw solutes for forward osmosis desalination as they exhibited high osmotic pressures and a small enthalpy of phase separation from water compared to conventional unresponsive draws (NaCl) and thermolytic salts. For an understanding of changes in the local molecular environment during the transition, the dynamic light scattering (DLS) revealed a common trend among IL-water LCST mixtures in which the IL forms small aggregates below T_c , which subsequently increased in size upon heating leading up to the critical point. This observation was specific to LCST mixtures i.e., after minor chemical modification of the anion which led to a fully miscible mixture, the system exhibited long-range order of hundreds on nm, which then decreased in size upon heating. Molecular dynamics (MD) simulation supported a stronger attractive interaction between cations and anions at above T_c of LCST. The driving force for the aggregation phenomena was analyzed by directional bonding with water molecules. For the ionic liquid combination to have LCST behavior, the directional bonding with water molecules was necessary to contribute to hydration shells around the ions of ionic liquid rather than hydrogen bonds. This chapter also investigated the osmotic strength of two candidate ionic liquids as draw solutes to desalinate feeds of varying salinity. The osmolality of the aqueous ionic liquids deviated from an ideal solution by van't Hoff theory. MD simulation explained the unusual dissolution by checking the number of water molecules inside the ions' first coordination shell to form a hydration shell. The study suggested a method to define a free ion by a cut-off number to satisfy the requirement for a hydration shell by comparing it with a single ion and pair simulations.

Chapter 3 investigated the amorphous phases and behavior of nanoconfined erythritol, as a representative of sugar alcohols (SAs), in ZIF-8 and ZIF-11 pores by utilizing MD simulations. Sugar alcohols have attractive characteristics as phase change materials, nevertheless, their

relatively high melting temperature limits their application in the real world. Nanoconfinement was used as a parameter to reduce the melting temperature. Although the experimental encapsulation of SAs (erythritol and xylitol) within a class of MOF was demonstrated, the mechanism behind the observed melting point depression and the phase identification in the nanopores could not be experimentally observed. Based on reliable partial charges for the ZIF structures calculated by a density functional theory, structural analysis showed the attractive interaction between SA and the ZIF structure frustrates the crystallization of SAs, and verified the second-order phase transition between amorphous phases. Here, I suggested a methodology to determine the phase transition temperature by using the MSD with fixed sampling times. The melting temperature of erythritol was reduced by the nanoconfinement from 391 K to 330 K or lower as a function of the ZIF pore size and the number of SA molecules. This chapter also explored the thermal conductivity of the SA-in-ZIF composites. The phonon frequency analysis through the HCACF and VDOS verified that the presence of SA molecules enhances the heat transfer by adding additional heat pathways between the nanoporous structure of ZIFs.

Chapter 4 studied a practical thermal device application that can be realized by phase change materials. Analogous to the electrical diode, a thermal rectifier transmits heat more easily in one direction than in the reverse direction. I suggested a thermal rectifier design of a solid-state junction comprised of two phase change materials and discussed a general theory for calculating the thermal rectification factor of the system. This provided a comprehensive analysis, considering whether phase changes happen in either (or both) of two material heterojunctions. The analysis of a heterojunction by the general theory showed the possibility to obtain a high thermal rectification by utilizing the thermal conductivity difference between phases of existing materials. With a further analysis based on the tunable phase change materials, the general theory suggested the theoretical maximal thermal rectification factor from optimization of design and thermal-bias conditions.

5.2 Recommendations for future work

Certainly, many works still need to be done to figure out the unusual behavior of anomalous phase transition materials and to expand their possibilities into the real world. Some parts of the theoretical works in this dissertation require a certain level of experimental validation and realization. Experiments and simulations are complementary and support each other by suggesting intriguing questions that cannot be resolved by themselves. Thinking beyond the interdependent role, the work of this dissertation also motivates the more challenging directions on computational work itself as described below.

5.2.1 Low Critical Solution Temperature (LCST) behavior

The DLS measurements in Chapter 2 showed a common trend of the aggregate size of IL-water LCST mixtures and MD simulations reproduced the observation of the subsequent increase in size upon heating. However, the all-atom classic MD simulation could not realize a few orders of magnitude radical increase of scattering diameter after the phase separation, i.e., above T_c . Both IL-rich and water-rich phases showed aggregates on the order of a few hundreds to thousands nm, of which system size is difficult to be simulated even at a general scale of cluster computers. Coarse-grained Molecular Dynamics (CGMD) can be applied to understand the mesoscale aggregation. Compared to the all-atom MD, each bead in CGMD represents three to five atoms and their pendant hydrogen atoms [143] to reduce the total number of particles in a simulation system. Since the LCST behavior comes from the interaction between water and the ion combination of hydrophobic/hydrophilic cation/anion, the water model should be considered carefully. We still have a question of whether a 2 or 3-site water model can reproduce the hydration effect on the ions. Coarse-grained water model [144,145] is an intriguing topic for general usage to scale up the system size of water mixture simulations. In Chapter 2, although the osmolality was measured experimentally, the theoretical work studied the osmotic strength by converting it to an apparent free ion ratio. Several works [146,147] have tried to directly calculate the osmotic pressure from MD simulations, however, the applications have been limited to the aqueous solutions with simple salt ions such as Na^+ , K^+ , and Cl^- . The suggested method is not proper to apply to such small molecules in this system. Thus, the development of a general methodology for osmotic pressure calculation remains an outstanding challenge and will make a benefit to the area of water treatment and osmosis materials.

5.2.2 Enthalpy of fusion and phase transition temperature of phase change materials

Although the MD simulation for the nanoconfined SAs checked the melting temperature depression and their second-order phase transition in Chapter 3, recognizable enthalpy of fusion was not observed. It is a technical limitation of MD simulation with the fixed partial charges on atoms. The underestimate of the computational enthalpy of fusion originates from two factors: the effects of quantum zero-point vibrational energy and electronic polarization [99]. The adjustment of phase transition temperature naturally brings the trade-off of latent heat. To accurately evaluate the availability of the encapsulated SAs to thermal energy applications, reliable results of enthalpy of fusion are necessary. *Ab initio* MD or other polarizable MD simulations can be used to calculate the enthalpy of fusion of the composites by removing the limitation of the force field with fixed partial charges. Beyond MOFs, the sweet spot size of pore volume should be searched with candidates having larger pore sizes. The consecutive researches and the collective data would suggest a general theory that determines critical parameters and predicts the relation between adjusted phase transition temperature and enthalpy of fusion.

5.2.3 Strategy for tunable phase transition temperature

The general theory for the heterojunction design of two phase-change materials demonstrated that the thermal bias range satisfying the local optimal thermal rectification is the widest when the phase transition temperatures of the two materials are identical. This finding means that the tunability of phase transition temperature can provide a remarkable improvement for the high thermal rectification and further for nonlinear thermal devices using phase change materials. Chapter 3 validated that the encapsulation of phase change materials is a parameter to reduce the phase transition temperature. The thermodynamic change (potential field and entropy) by the boundary interaction with frameworks shifts the equilibration of the free energy between phases. Entropy change is another key parameter for fine control of the phase transition temperature. For example, additives (such as metal particles, ions, or polymers) to phase change materials can affect the structure order and then their entropy. We further suggest a possibility of active controllability of phase transition temperature by applying an external force field which can affect the additives. Polyelectrolyte as an additive is an interesting material with a lot of controllable parameters that could allow the precise and active tuning of the phase transition temperature.

References

- [1] U. S. Energy Information Administration, 2015 Residential Energy Consumption Survey (2015).
- [2] N. Vergadou and D. N. Theodorou, *Membranes* **9**, 98 (2019).
- [3] D. C. Rapaport, *The art of molecular dynamics simulation* (Cambridge university press, 2004).
- [4] S. J. Plimpton and A. P. Thompson, *MRS bulletin* **37**, 513 (2012).
- [5] <https://lammmps.sandia.gov/bench.html#potentials>
- [6] W. C. Swope, H. C. Andersen, P. H. Berens, and K. R. Wilson, *The Journal of chemical physics* **76**, 637 (1982).
- [7] M. Puligheddu, Y. Xia, M. Chan, and G. Galli, *Physical Review Materials* **3**, 085401 (2019).
- [8] A. van Roekeghem, J. Carrete, C. Oses, S. Curtarolo, and N. Mingo, *Physical Review X* **6**, 041061 (2016).
- [9] R. Kubo, *Reports on progress in physics* **29**, 255 (1966).
- [10] J.-P. Hansen and I. R. McDonald, *Theory of simple liquids* (Elsevier, 1990).
- [11] R. E. Jones and K. K. Mandadapu, *The Journal of chemical physics* **136**, 154102 (2012).
- [12] T. Ikeshoji and B. Hafskjold, *Molecular Physics* **81**, 251 (1994).
- [13] T.-P. Teng, Y.-H. Hung, T.-C. Teng, H.-E. Mo, and H.-G. Hsu, *Applied Thermal Engineering* **30**, 2213 (2010).
- [14] H. Bao, J. Chen, X. Gu, and B. Cao, *ES Energy & Environment* **1**, 16 (2018).
- [15] B. J. Alder and T. E. Wainwright, *The Journal of chemical physics* **27**, 1208 (1957).
- [16] D. Poulikakos, S. Arcidiacono, and S. Maruyama, *Microscale Thermophysical Engineering* **7**, 181 (2003).
- [17] https://en.wikibooks.org/wiki/Molecular_Simulation/Radial_Distribution_Functions
- [18] S. Yadav, A. Choudhary, and A. Chandra, *The Journal of Physical Chemistry B* **121**, 9032 (2017).
- [19] D. L. Shaffer, L. H. Arias Chavez, M. Ben-Sasson, S. Romero-Vargas Castrillón, N. Y. Yip, and M. Elimelech, *Environmental Science & Technology* **47**, 9569 (2013).
- [20] B. K. Pramanik, L. Shu, and V. Jegatheesan, *Environmental Science: Water Research & Technology* **3**, 625 (2017).
- [21] T. Tong and M. Elimelech, *Environmental Science & Technology* **50**, 6846 (2016).

- [22] E. W. Tow and J. H. Lienhard V, *Journal of Membrane Science* **544**, 221 (2017).
- [23] E. W. Tow, D. M. Warsinger, A. M. Trueworthy, J. Swaminathan, G. P. Thiel, S. M. Zubair, A. S. Myerson, and J. H. Lienhard V, *Journal of Membrane Science* **556**, 352 (2018).
- [24] M. F. A. Goosen, S. S. Sablani, H. Al-Hinai, S. Al-Obeidani, R. Al-Belushi, and D. Jackson, *Separation Science and Technology* **39**, 2261 (2005).
- [25] G. P. Thiel, E. W. Tow, L. D. Banchik, H. W. Chung, and J. H. Lienhard, *Desalination* **366**, 94 (2015).
- [26] D. L. Shaffer, J. R. Werber, H. Jaramillo, S. Lin, and M. Elimelech, *Desalination* **356**, 271 (2015).
- [27] K. H. Mistry, R. K. McGovern, G. P. Thiel, E. K. Summers, S. M. Zubair, and J. H. Lienhard, *Entropy* **13**, 1829 (2011).
- [28] A. Deshmukh, C. Boo, V. Karanikola, S. Lin, A. P. Straub, T. Tong, D. M. Warsinger, and M. Elimelech, *Energy & Environmental Science* **11**, 1177 (2018).
- [29] Y. Kohno and H. Ohno, *Physical Chemistry Chemical Physics* **14**, 5063 (2012).
- [30] Y. Kohno and H. Ohno, *Chemical Communications* **48**, 7119 (2012).
- [31] K. Fukumoto and H. Ohno, *Angewandte Chemie International Edition* **46**, 1852 (2007).
- [32] Y. Fukaya, K. Sekikawa, K. Murata, N. Nakamura, and H. Ohno, *Chem. Commun.*, 3089 (2007).
- [33] Y. Kohno, H. Arai, S. Saita, and H. Ohno, *Australian Journal of Chemistry* **64**, 1560 (2012).
- [34] Y. Kohno and H. Ohno, *Chemical Communications* **48**, 7119 (2012).
- [35] Y. Kohno and H. Ohno, *Physical Chemistry Chemical Physics* **14**, 5063 (2012).
- [36] T. Ando, Y. Kohno, N. Nakamura, and H. Ohno, *Chemical Communications* **49**, 10248 (2013).
- [37] Y. Fukaya and H. Ohno, *Physical Chemistry Chemical Physics* **15**, 4066 (2013).
- [38] S. Saita, Y. Kohno, N. Nakamura, and H. Ohno, *Chemical Communications* **49**, 8988 (2013).
- [39] P. Paricaud, A. Galindo, and G. Jackson, *Molecular Physics* **101**, 2575 (2003).
- [40] E. Kartzmark, *Canadian Journal of Chemistry* **45**, 1089 (1967).
- [41] M. Yu and H. Nishiumi, *The Journal of Physical Chemistry* **96**, 842 (1992).
- [42] J. R. McCutcheon, R. L. McGinnis, and M. Elimelech, *Desalination* **174**, 1 (2005).
- [43] M. L. Stone, C. Rae, F. F. Stewart, and A. D. Wilson, *Desalination* **312**, 124 (2013).
- [44] C. Chiappe and D. Pieraccini, *Journal of Physical Organic Chemistry* **18**, 275 (2005).
- [45] P. Rao, R. Kostecky, L. Dale, and A. Gadgil, *Annual Review of Environment and*

Resources **42**, 407 (2017).

[46] J. S. McNally, X. P. Wang, C. Hoffmann, and A. D. Wilson, *Chemical Communications* **53**, 10934 (2017).

[47] W. Li and P. Wu, *Polymer Chemistry* **5**, 5578 (2014).

[48] T. Morita, K. Miki, A. Nitta, H. Ohgi, and P. Westh, *Physical Chemistry Chemical Physics* **17**, 22170 (2015).

[49] A. A. Zavitsas, *The Journal of Physical Chemistry B* **105**, 7805 (2001).

[50] Y. Kohno, Y. Deguchi, and H. Ohno, *Chemical Communications* **48**, 11883 (2012).

[51] Y. Zhao, H. Wang, Y. Pei, Z. Liu, and J. Wang, *Physical Chemistry Chemical Physics* **18**, 23238 (2016).

[52] R. Wang, W. Leng, Y. Gao, and L. Yu, *RSC Advances* **4**, 14055 (2014).

[53] A. Nitta, T. Morita, S. Saita, Y. Kohno, H. Ohno, and K. Nishikawa, *Chemical Physics Letters* **628**, 108 (2015).

[54] R. Hayes, G. G. Warr, and R. Atkin, *Chemical Reviews* **115**, 6357 (2015).

[55] S. Feng and G. A. Voth, *Fluid Phase Equilibria* **294**, 148 (2010).

[56] Y.-L. Wang, S. Sarman, S. Glavatskih, O. N. Antzutkin, M. W. Rutland, and A. Laaksonen, *The Journal of Physical Chemistry B* **119**, 5251 (2015).

[57] A. Nitta, T. Morita, K. Nishikawa, and Y. Koga, *Physical Chemistry Chemical Physics* **19**, 16888 (2017).

[58] G. Zhou, X. Liu, S. Zhang, G. Yu, and H. He, *The Journal of Physical Chemistry B* **111**, 7078 (2007).

[59] X. He, O. Guvench, A. D. MacKerell Jr, and M. L. Klein, *The Journal of Physical Chemistry B* **114**, 9787 (2010).

[60] M. A. González and J. L. Abascal, *The Journal of chemical physics* **135**, 224516 (2011).

[61] W. D. Cornell *et al.*, *Journal of the American Chemical Society* **117**, 5179 (1995).

[62] Z. Liu, S. Huang, and W. Wang, *The Journal of Physical Chemistry B* **108**, 12978 (2004).

[63] C.-M. Ionescu, D. Sehnal, F. L. Falginella, P. Pant, L. Pravda, T. Bouchal, R. S. Vařeková, S. Geidl, and J. Koča, *Journal of cheminformatics* **7**, 50 (2015).

[64] G. D. Smith, D. Bedrov, and O. Borodin, *Physical review letters* **85**, 5583 (2000).

[65] F. T. S. Chan, *International Journal of Production Research* **41**, 3549 (2003).

[66] M. Yasukawa, Y. Tanaka, T. Takahashi, M. Shibuya, S. Mishima, and H. Matsuyama, *Industrial & Engineering Chemistry Research* **54**, 8239 (2015).

[67] Y. Cai, W. Shen, J. Wei, T. H. Chong, R. Wang, W. B. Krantz, A. G. Fane, and X. Hu, *Environmental Science: Water Research & Technology* **1**, 341 (2015).

- [68] H. W. Horn, W. C. Swope, J. W. Pitera, J. D. Madura, T. J. Dick, G. L. Hura, and T. Head-Gordon, *The Journal of Chemical Physics* **120**, 9665 (2004).
- [69] X. Liu, S. Zhang, G. Zhou, G. Wu, X. Yuan, and X. Yao, *The Journal of Physical Chemistry B* **110**, 12062 (2006).
- [70] R. W. Hockney and J. W. Eastwood, *Computer simulation using particles* 1988).
- [71] M. M. Farid, A. M. Khudhair, S. A. K. Razack, and S. Al-Hallaj, *Energy conversion and management* **45**, 1597 (2004).
- [72] S. Zhang and Z. Wang, *Renewable and Sustainable Energy Reviews* **82**, 2319 (2018).
- [73] W. Aftab, X. Huang, W. Wu, Z. Liang, A. Mahmood, and R. Zou, *Energy & Environmental Science* **11**, 1392 (2018).
- [74] M. Kenisarin and K. Mahkamov, *Renewable and sustainable energy reviews* **11**, 1913 (2007).
- [75] C.-C. Lai, W.-C. Chang, W.-L. Hu, Z. M. Wang, M.-C. Lu, and Y.-L. Chueh, *Nanoscale* **6**, 4555 (2014).
- [76] Y. Yamagishi, H. Takeuchi, A. T. Pyatenko, and N. Kayukawa, *Aiche Journal* **45**, 696 (1999).
- [77] K. Merlin, J. Soto, D. Delaunay, and L. Traonvouez, *Applied energy* **183**, 491 (2016).
- [78] S. A. Khateeb, S. Amiruddin, M. Farid, J. R. Selman, and S. Al-Hallaj, *Journal of Power Sources* **142**, 345 (2005).
- [79] R. Barzin, J. J. Chen, B. R. Young, and M. M. Farid, *Energy* **92**, 505 (2015).
- [80] S. A. Memon, *Renewable and sustainable energy reviews* **31**, 870 (2014).
- [81] J. Skovajsa, M. Koláček, and M. Zálešák, *Energies* **10**, 152 (2017).
- [82] D. C. Hyun, N. S. Levinson, U. Jeong, and Y. Xia, *Angewandte Chemie International Edition* **53**, 3780 (2014).
- [83] A. Solé, L. Miró, C. Barreneche, I. Martorell, and L. F. Cabeza, *Renewable Energy* **75**, 519 (2015).
- [84] T. Nomura, C. Zhu, A. Sagara, N. Okinaka, and T. Akiyama, *Applied Thermal Engineering* **75**, 481 (2015).
- [85] H. Li, M. Eddaoudi, M. O'Keeffe, and O. M. Yaghi, *nature* **402**, 276 (1999).
- [86] C. Wang, L. Feng, H. Yang, G. Xin, W. Li, J. Zheng, W. Tian, and X. Li, *Physical Chemistry Chemical Physics* **14**, 13233 (2012).
- [87] T. Uemura, N. Yanai, S. Watanabe, H. Tanaka, R. Numaguchi, M. T. Miyahara, Y. Ohta, M. Nagaoka, and S. Kitagawa, *Nature communications* **1**, 1 (2010).
- [88] J. Tang, M. Yang, W. Dong, M. Yang, H. Zhang, S. Fan, J. Wang, L. Tan, and G. Wang, *RSC advances* **6**, 40106 (2016).

- [89] L. Hackl *et al.*, *Journal of Materials Chemistry A* (2020).
- [90] J. Zhang, T. Zhang, D. Yu, K. Xiao, and Y. Hong, *CrystEngComm* **17**, 8212 (2015).
- [91] H. Fu, Z. Wang, X. Wang, P. Wang, and C.-C. Wang, *CrystEngComm* **20**, 1473 (2018).
- [92] K. S. Park, Z. Ni, A. P. Côté, J. Y. Choi, R. Huang, F. J. Uribe-Romo, H. K. Chae, M. O’Keeffe, and O. M. Yaghi, *Proceedings of the National Academy of Sciences* **103**, 10186 (2006).
- [93] B. Cui, C. O. Audu, Y. Liao, S. T. Nguyen, O. K. Farha, J. T. Hupp, and M. Grayson, *ACS applied materials & interfaces* **9**, 28139 (2017).
- [94] A. McGaughey and M. Kaviany, *International Journal of Heat and Mass Transfer* **47**, 1799 (2004).
- [95] S.-M. Lee and D. G. Cahill, *Journal of applied physics* **81**, 2590 (1997).
- [96] H. Babaei *et al.*, *Nature Communications* **11**, 1 (2020).
- [97] B. Zheng, M. Sant, P. Demontis, and G. B. Suffritti, *The Journal of Physical Chemistry C* **116**, 933 (2012).
- [98] T. A. Manz and N. G. Limas, *RSC advances* **6**, 47771 (2016).
- [99] T. Inagaki and T. Ishida, *The Journal of Physical Chemistry C* **120**, 7903 (2016).
- [100] S. Höhlein, A. König-Haagen, and D. Brüggemann, *Materials* **10**, 444 (2017).
- [101] W. Shinoda, M. Shiga, and M. Mikami, *Physical Review B* **69**, 134103 (2004).
- [102] W. Zhou, H. Wu, T. J. Udovic, J. J. Rush, and T. Yildirim, *The Journal of Physical Chemistry A* **112**, 12602 (2008).
- [103] S. A. Moggach, T. D. Bennett, and A. K. Cheetham, *Angewandte Chemie International Edition* **48**, 7087 (2009).
- [104] A. F. Sapnik, H. S. Geddes, E. M. Reynolds, H. H.-M. Yeung, and A. L. Goodwin, *Chemical Communications* **54**, 9651 (2018).
- [105] Y. Zhang and E. J. Maginn, *The Journal of chemical physics* **136**, 144116 (2012).
- [106] D. McQuarrie, Sausalito, CA, 222 (2000).
- [107] B. Huang, A. McGaughey, and M. Kaviany, *International journal of heat and mass transfer* **50**, 393 (2007).
- [108] X. Zhang and J. Jiang, *The Journal of Physical Chemistry C* **117**, 18441 (2013).
- [109] J. Dickey and A. Paskin, *Physical Review* **188**, 1407 (1969).
- [110] D. W. Hahn and M. N. Özisik, *Heat conduction* (John Wiley & Sons, 2012).
- [111] N. Li, J. Ren, L. Wang, G. Zhang, P. Hänggi, and B. Li, *Reviews of Modern Physics* **84**, 1045 (2012).
- [112] N. Yang, N. Li, L. Wang, and B. Li, *Physical Review B* **76**, 020301 (2007).

- [113] M. Peyrard, EPL (Europhysics Letters) **76**, 49 (2006).
- [114] N. A. Roberts and D. Walker, International Journal of Thermal Sciences **50**, 648 (2011).
- [115] Y. Wang, A. Vallabhaneni, J. Hu, B. Qiu, Y. P. Chen, and X. Ruan, Nano letters **14**, 592 (2014).
- [116] C. Chang, D. Okawa, A. Majumdar, and A. Zettl, Science **314**, 1121 (2006).
- [117] B. V. Budaev and D. B. Bogy, Applied Physics Letters **109**, 231905 (2016).
- [118] J. Zhu *et al.*, Nano letters **14**, 4867 (2014).
- [119] T. Zhang and T. Luo, Small **11**, 4657 (2015).
- [120] H. Wang, S. Hu, K. Takahashi, X. Zhang, H. Takamatsu, and J. Chen, Nature Communications **8**, ncomms15843 (2017).
- [121] R. Dettori, C. Melis, R. Rurali, and L. Colombo, Journal of Applied Physics **119**, 215102 (2016).
- [122] Z. Chen *et al.*, Nature communications **5** (2014).
- [123] P. Ben-Abdallah and S.-A. Biehs, Applied Physics Letters **103**, 191907 (2013).
- [124] A. Ghanekar, J. Ji, and Y. Zheng, Applied Physics Letters **109**, 123106 (2016).
- [125] C. Dames, Journal of Heat Transfer **131**, 061301 (2009).
- [126] D. M. Leitner, The Journal of Physical Chemistry B **117**, 12820 (2013).
- [127] W. Kobayashi, Y. Teraoka, and I. Terasaki, Applied Physics Letters **95**, 171905 (2009).
- [128] D. Sawaki, W. Kobayashi, Y. Moritomo, and I. Terasaki, Applied physics letters **98**, 081915 (2011).
- [129] W. Kobayashi, D. Sawaki, T. Omura, T. Katsufuji, Y. Moritomo, and I. Terasaki, Applied Physics Express **5**, 027302 (2012).
- [130] R. Chen *et al.*, Scientific reports **5**, 8884 (2015).
- [131] A. L. Cottrill and M. S. Strano, Advanced Energy Materials **5** (2015).
- [132] A. L. Cottrill, S. Wang, A. T. Liu, W. J. Wang, and M. S. Strano, Advanced Energy Materials.
- [133] J. Ordonez-Miranda, J. M. Hill, K. Joulain, Y. Ezzahri, and J. Drevillon, Journal of Applied Physics **123**, 085102 (2018).
- [134] S. Lee *et al.*, Science **355**, 371 (2017).
- [135] T. Zhang and T. Luo, ACS nano **7**, 7592 (2013).
- [136] D.-W. Oh, C. Ko, S. Ramanathan, and D. G. Cahill, Applied Physics Letters **96**, 151906 (2010).
- [137] M. D. Losego, L. Moh, K. A. Arpin, D. G. Cahill, and P. V. Braun, Applied Physics Letters

97, 011908 (2010).

[138] D. G. Cahill, W. K. Ford, K. E. Goodson, G. D. Mahan, A. Majumdar, H. J. Maris, R. Merlin, and S. R. Phillpot, *Journal of applied physics* **93**, 793 (2003).

[139] M. D. Losego, M. E. Grady, N. R. Sottos, D. G. Cahill, and P. V. Braun, *Nature materials* **11**, 502 (2012).

[140] S. Majumdar, J. A. Sierra-Suarez, S. N. Schiffres, W.-L. Ong, C. F. Higgs III, A. J. McGaughey, and J. A. Malen, *Nano letters* **15**, 2985 (2015).

[141] H. Acharya, N. J. Mozdierz, P. Koblinski, and S. Garde, *Industrial & Engineering Chemistry Research* **51**, 1767 (2011).

[142] H. D. Pandey and D. M. Leitner, *The Journal of chemical physics* **147**, 084701 (2017).

[143] G. Fitzgerald, J. DeJoannis, and M. Meunier, in *Modeling, Characterization, and Production of Nanomaterials* (Elsevier, 2015), pp. 3.

[144] K. R. Hadley and C. McCabe, *Molecular simulation* **38**, 671 (2012).

[145] H. Chan, M. J. Cherukara, B. Narayanan, T. D. Loeffler, C. Benmore, S. K. Gray, and S. K. Sankaranarayanan, *Nature communications* **10**, 1 (2019).

[146] S. Murad, *Adsorption* **2**, 95 (1996).

[147] Y. Luo and B. Roux, *The journal of physical chemistry letters* **1**, 183 (2010).